Continuum-Scale Modeling of Rechargeable Batteries

by

Saeed Kazemiabnavi

A dissertation submitted in partial fulfillment
of the requirements for the degree of
Doctor of Philosophy
(Mechanical Engineering)
in the University of Michigan
2020

Doctoral Committee:

Professor Donald J. Siegel, Chair
Assistant Professor Neil P. Dasgupta
Associate Professor Christian Lastoskie
Associate Professor Jeff Sakamoto

Saeed Kazemiabnavi

skazemi@umich.edu

ORCID iD: 0000-0003-2409-709X

Dedication

To my best friend and the love of my life, Haniyeh,

who has always been by my side with her love and support.

Acknowledgements

I would like to express my deepest gratitude and sincere appreciation to many people for their support that helped me complete the work presented in this dissertation.

First and foremost, I would like to thank my advisor, Prof. Donald J. Siegel, for his invaluable encouragement, support and patience throughout my graduate studies at the University of Michigan. He has set an example of excellence as a researcher, mentor and instructor. I would also like to thank Prof. Katsuyo Thornton, Prof. Jeff Sakamoto, and Prof. Neil Dasgupta for their tremendous support throughout my research. I am truly grateful for their guidance during these years and I consider myself incredibly lucky and privileged to have collaborated with such knowledgeable and insightful researchers. In addition, I would like to thank Prof. Christian Lastoskie for his willingness to serve on my committee and for providing helpful feedback and guidance on my research.

A special thanks goes out to the senior graduate students and postdocs in Prof. Thornton's research group, including Dr. Stephen DeWitt, Dr. Alexander Chadwick, Dr. Bernardo Orvananos, Dr. Hui-Chia Yu, Dr. William Andrewes, and Dr. Raúl Enrique for generously taking the time for the many questions I have asked them. I am also grateful for the many past and current members of the Thornton Group for their mutual trust, friendship and support over past several years.

I would also like to acknowledge the various funding agencies and user facilities for providing financial support and computational resources. The work contained within this thesis was supported by the NorthEast Center for Chemical Energy Storage (NECCES), an Energy

Frontier Research Center funded by the U.S. Department of Energy, Office of Science; the Joint Center for Energy Storage Research (JCESR), an Energy Innovation Hub funded by the U.S. Department of Energy, Office of Science, Basic Energy Sciences under Award Numbers DE-SC0001294 and DE-SC-0012583; U.S. Department of Energy - Energy Efficiency and Renewable Energy (EERE) office, under Award Number DE-EE0008362. I would also like to extend my thanks to the Rackham Graduate School for generously supporting this research through the Rackham International Student Fellowship that was awarded to me for the Winter 2016 semester. Moreover, many of the computational resources were provided by the National Energy Research Scientific Computing Center (NERSC), a U.S. Department of Energy Office of Science User Facility operated under Contract No. DE-AC02-05CH11231. Additional computational resources were provided by the University of Michigan's Advanced Research Computing.

I am also thankful to my friends and family for their constant support and enthusiasm during these past years. I am especially grateful to my in-laws, Hamid and Mitra, as well as my sister in-law, Reyhaneh, for their unconditional support and encouragement. Last but certainly not least, this dissertation would not have been possible without the unceasing support and sacrifices of my wonderful wife, Haniyeh, who has always been by my side, encouraging me every step of the way.

Table of Contents

List of Tables

List of Figures

Abstract

During the operation of a rechargeable battery, the electrochemical reactions occur at the interface between the electrolyte and the active material in the electrode. The electrochemical performance of such batteries is influenced by a complex interplay between the kinetics of the electrochemical reactions and the transport of reactant and product species in the electrode and electrolyte. In this dissertation, the effect of various electrode and electrolyte properties on the electrochemical performance of the battery is investigated via computational modeling at a variety of length scales and dimensionalities. Two applications are studied in this dissertation: the kinetics and thermodynamics of nucleation during electrodeposition on metallic anodes, and the transport kinetics in the electrolyte and intercalating electrodes in lithium-ion batteries.

A continuum-scale model based on the classical theory of nucleation is formulated to study the nucleation behavior of several metals during electrodeposition on metal anodes. The model utilizes the formation energies of critical nuclei obtained from density functional theory calculations to estimate the time-dependent and steady-state nucleation rate and density on various metal anodes. Nucleation rates are predicted to be several orders of magnitude larger on alkali metal surfaces than on the other metals. This multiscale model highlights the sensitivity of the nucleation behavior on the structure and composition of the electrode surface.

In order to study the kinetics of lithium ion transport in intercalating electrode particles, a continuum-scale model is developed that provides detailed insight into the kinetics and voltage behavior of the (de)intercalation processes in core-shell heterostructure cathode particles. The simulations indicated that an open-circuit potential difference between the surface and bulk

phases in a core-shell cathode particle leads to a charge/discharge asymmetry in the galvanostatic voltage profiles, causing a decrease in the accessible capacity of the particle. Moreover, further simulations showed that this reduction in the accessible capacity is smaller when the surface-phase diffusivity is higher than the bulk-phase diffusivity. These findings provide valuable guidance in developing material selection criteria that ensures optimal electrochemical performance in core-shell heterostructure hybrid cathode particles.

In composite battery electrode architectures, local limitations in ionic and electronic transport can result in nonuniform energy storage reactions. A continuum-scale model based on the porous electrode theory was utilized to investigate the effect of various electrode and electrolyte properties on the reaction heterogeneity across the electrode thickness. Our simulations showed that accelerated reactions at the electrode faces in contact with either the separator or the current collector demonstrate that both ionic and electronic transport limit the reaction progress. This rate heterogeneity may accelerate rate-dependent degradation pathways in regions of the composite electrode experiencing faster-than-average reaction.

Designing Li-ion batteries with electrodes that are capable of fast ion transport is essential in improving their power density under fast-charging conditions. In order to investigate the effect of introducing vertical channels through the thickness of the electrode on the Li ion transport during fast charging, a three-dimensional continuum-scale model based on the porous electrode theory is developed. These simulations allow us to investigate the geometric parameters that affect the electrochemical performance of highly-ordered hierarchical (HOH) anodes under galvanostatic extreme fast charging conditions. Our analysis showed that the HOH anode architecture with optimized geometric parameters can significantly improve the galvanostatic charge capacity of the electrode at high rates by minimizing the transport limitations that occur during extreme fast charging conditions.

Chapter 1.

Introduction

Context and Motivation

During the past few decades, rechargeable batteries have received significant attention for a wide range of applications including consumer electronic products such as cell phones and laptops, electrified powertrain systems such as electric vehicles (EVs) and hybrid electric vehicles (HEVs), and powering supplies in aerospace systems such as aircrafts and space exploration vehicles (rovers) [1, 2]. In particular, lithium-ion batteries have a higher energy and power density compared to more conventional battery chemistries such as lead-acid and nickel-metal hydride batteries, which makes them suitable for use in EVs and HEVs [3]. Moreover, the development and manufacturing cost of lithium-ion battery packs has been rapidly decreasing over the past decade [4], making them of increasing interest in home and grid storage applications [5, 6].

A lithium-ion battery is an electrochemical device that converts the stored chemical energy into electrical energy. Since the invention of voltaic pile by Alessandro Volta in 1800 [7], significant improvements have been made in the development of the electrochemical cell components, while the operating principles have not fundamentally changed. As shown in the schematic illustration in Figure 1.1, a lithium-ion battery consists of anode (negative) and cathode (positive) electrodes, which are usually porous materials capable of reversibly storing lithium in their crystal structure [7, 8]. These two electrodes along with an electronicallyisolating porous separator are soaked into a liquid electrolyte that fills the pores of their structure and allows for ionic transport between the anode and cathode during the operation of the battery.

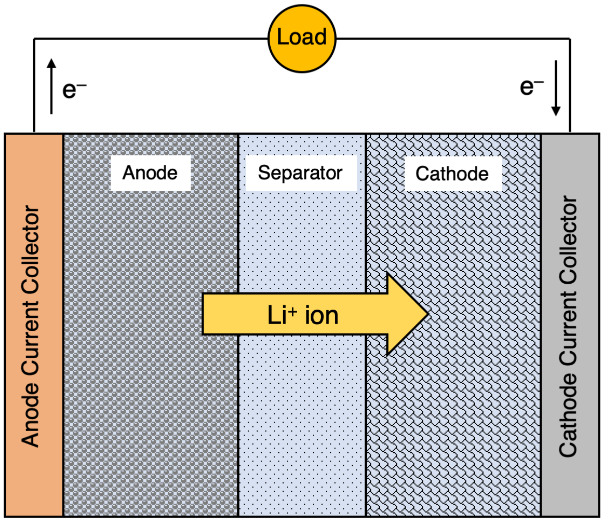

Figure 1.1. Schematic illustration of the structure and operation of lithium-ion battery during discharge. The reverse reactions occur during charge.

The electrochemical reactions occur at the interface between the electrode particles and electrolyte. During discharge, the oxidation reaction occurs at the anode/electrolyte interface and the reduction reaction occurs at the cathode/electrolyte interface. Therefore, during discharge, lithium atoms depart from the anode material, travel in the electrolyte through the separator in the form of Li^+ ion, and intercalate into the cathode particles [7, 8]. This process generates an electromotive force, which sends the electrons from the anode to the cathode by travelling through the battery external circuit in order to balance the charges. Therefore, an electric current is generated, which can be used to power a load. The opposite of this reversible process occurs during charge [7].

Since 1999 when Sony Corporation successfully commercialized the lithium-ion battery technology for small portable electronic devices, several active material have been developed for use in the anode and cathode electrodes [7], each with their own advantages and disadvantages making them suitable for specific applications. Carbon-based intercalation materials with various morphologies such as graphite and hard carbon have been long considered as the most widely used anode material in commercial lithium-ion battery cells thanks to their low working potential, high safety, and low cost. However, these materials suffer from a high voltage hysteresis and irreversible capacity loss [9]. Titanium-based oxides such as spinel $Li_4Ti_5O_{12}$ (LTO) and TiO_2 have also been extensively studied as promising anode materials, which benefit from a long cycle-life, high safety, and high-power capability. However, very low capacity and low energy density are the common issues among this type of anode materials [9]. Alloying anodes such as high Si, Ge, Sn, P, and Si/Sn-based oxides have a much higher specific capacity and energy density compared to intercalation materials [9]. However, one of the main challenging issues with this type of materials is the unavoidable large volume expansion during lithiation, resulting in a poor cycling capability. Similarly, transition metal oxide conversion anode materials such as oxides of Fe, Co, Ni, Mn, Cu, Mo, etc., benefit from high specific capacities, but suffer from large volume change, low coulombic efficiency, and unstable SEI, which results in a poor cycling capability. Lithium metal anode provides the highest specific capacity and lowest working potential. However, the use of metallic lithium in rechargeable batteries have always been accompanied by safety concerns, mainly due to the dendrite formation on the surface of anode, which can penetrate the polymer separator and possibly cause fire due to internal short-circuit [10].

One of the most commonly used cathode materials in lithium-ion batteries are layered lithium metal oxides such as lithium cobalt oxide ($LiCoO_2$ or LCO), thanks to their high structural stability [11]. As a solution to reduce the synthesis cost and improve the electrochemical performance and thermal stability of LCO, the mixed transition metal oxide variants of layered cathode materials have gained significant attention [12]. In particular, nickel-rich compositions of layered oxides such as lithium nickel manganese cobalt oxides ($LiNi_{1-x-y}Co_xMn_yO_2$ or NMC) and lithium nickel cobalt aluminum oxide ($LiNi_{1-x-y}Co_xAl_yO_2$ or NCA), have been increasingly used in commercial lithium-ion cells for automotive applications due to their improved energy density and rate capability [12]. Olivines, which are mainly recognized by their compound name, lithium iron phosphate ($LiFePO_4$ or LFP) are another common type of cathode materials. These materials have a moderate specific capacity, but offer benefits such as small capacity fade as well as being non-toxic and environmentally friendly [11]. Lithium manganese oxide ($LiMn_2O_4$ or LMO) spinel cathode materials are also used as cathode materials in lithium-ion batteries. This material have a high rate capability and minimal environmental impacts [11], but is unstable in a reduced capacity state due to the presence of electrochemically active Mn^{3+} ions, which results in a large capacity fade upon frequent cycling [11].

Over the past two decades, researchers have been continuously working on improving the safety and energy density of rechargeable batteries, especially for large-scale applications [13-16]. Such efforts require a deep understanding of the battery materials behavior under various operating conditions. Due to the complicated multi-physics nature of batteries, physics-based models can provide a deep understanding of the multiple physical and chemical phenomena that occur simultaneously during the operation of the battery. Moreover, the complex interplay of these physical processes creates complicated problems, each of which require a specific temporal and spatial resolution. Therefore, a wide range of simulation and modeling approaches will be required to study these systems, including atomistic-level techniques (Density Functional Theory [17-23] and Molecular Dynamics [24, 25] simulations), stochastic approaches (Monte Carlo and Kinetic Monte Carlo simulations [26]), and continuum-scale modeling techniques [10, 27, 28]. In continuum-scale models, the behavior of individual atoms is neglected, and the average response of the system are captured by studying the coarse-grained description of that phenomenon. The main focus of this dissertation will be on continuum-scale models applied to the electrochemical processes that occur in a broad range of time and length scales.

Dissertation Overview

In this dissertation, three examples of electrochemical processes are considered that occur during the operation of metal anode and lithium-ion batteries: i) thermodynamics and kinetics of nucleation during electrodeposition in metal anode batteries, ii) kinetics of lithium intercalation in electrode particles, and iii) the electrochemical behavior of lithium-ion battery electrodes under various operating conditions. In order to study these systems, three different computational models are presented. The first model uses the classical theory of nucleation to study the nucleation behavior of several metals during electrodeposition on metal anodes. This model utilizes the formation energies of critical nuclei obtained from density functional theory (DFT) calculations to estimate the time-dependent and steady-state nucleation rate and density on various metal anode surfaces. The second one is a one-dimensional model based on the smoothed-boundary formulation of transport equation, which allows for explicitly distinguishing different phases in the model system. This model is used to study the kinetics of lithium intercalation in core-shell heterostructure cathode particles. The third one is a three-dimensional model based on the porous electrode theory, which is used to study the effect of various electrode and electrolyte properties on the reaction heterogeneity in battery electrodes. This model is also used to study the electrochemical behavior of highly ordered hierarchical anode architectures in extreme fast charging lithium-ion batteries. The simulation results of this model are also validated against experimental measurements.

This dissertation is divided into eight chapters: (1) Introduction, (2) Background, (3) Thermodynamics and Kinetics of Nucleation during Electrodeposition on Metal Anodes, (4) The Effect of Surface-Bulk Potential Difference on the Kinetics of Intercalation in Core-Shell Active Cathode Particles, (5) The Effect of Lithium Diffusivity and Particle Geometry on the Kinetics of Intercalation in Core-Shell Active Cathode Particles (6) Reaction Heterogeneity in Battery Electrodes, (7) Electrochemical Behavior of Highly Ordered Hierarchical Anode Architectures for Extreme Fast Charging Batteries, and (8) Summary and Future Work. In this dissertation, the goal is to find an explanation for the following questions:

1. What determines the nucleation behavior and characteristics of different metal anodes during electrodeposition?

2. In hybrid cathode particles, how do the thermodynamic and kinetic properties of its active materials affect the electrochemical behavior of the particle?

3. What causes reaction heterogeneity in battery electrodes?

4. How can the electrode architecture be modified to improve its rate capability?

Chapter 2 provides a general overview of different battery modeling approaches, and in particular, the underlying physics, assumptions, and the governing equations of the pseudo two-dimensional model developed by Newman et al. [29, 30], which is extensively used in literature as a comprehensive physics-based approach for modeling electrochemical systems.

In chapter 3, a model based on the classical theory of nucleation is utilized to study the nucleation behavior of several metals during electrodeposition on metal anodes. The model uses the formation energies of critical nuclei obtained from density functional theory (DFT) calculations to estimate the time-dependent and steady-state nucleation rate and density on various metal anodes with potential applications in single- and multi-valent metal anode batteries.

In chapter 4 and 5, a continuum-scale model is developed to study the kinetics of lithium ion transport in intercalating electrode particles. The model uses smoothed-boundary method to reformulate the governing partial differential equations, which allows for explicitly distinguishing different phases that are present in the model system. The simulations provide detailed insight into the kinetics and voltage behavior of the intercalation/de-intercalation processes in core-shell heterostructure cathode particles.

In chapter 6, a continuum-scale model based on the porous electrode theory is developed to study the reaction heterogeneity in the composite porous electrode of a lithium-ion battery. These simulations allow us to investigate the effect of various electrode and electrolyte properties on the reaction heterogeneity across the electrode thickness. The simulation results are also validated against the experimental data obtained from X-ray diffraction computed tomography (XRD-CT) measurements.

In chapter 7, a three-dimensional continuum-scale model based on the porous electrode theory is developed to investigate the effect of introducing vertical channels through the thickness of the electrode on the Li ion transport during fast charging. These simulations allow us to investigate the geometric parameters that affect the electrochemical performance of highly-ordered hierarchical (HOH) anodes under galvanostatic extreme fast charging conditions.

In chapter 8, a summary of the research presented in this dissertation and our key findings are discussed, along with potential areas where the modeling frameworks can be extended to for future studies.

Author Contributions

Chapter 3: D. J. Siegel conceived the presented idea. K. Nagy performed the DFT simulations under the supervision of D. J. Siegel. S. Kazemiabnavi performed the continuum-scale simulations under the supervision of K. Thornton and D. J. Siegel. K. Nagy and D. J. Siegel took the lead in writing the manuscript with contributions from S. Kazemiabnavi and K. Thornton.

Chapter 4: K. Thornton and G. Ceder conceived the study. B. Orvananos, R. Malik, and A. Abdellahi derived the initial model and numerical scheme under the supervision of K. Thornton and G. Ceder. S. Kazemiabnavi modified the model and numerical scheme, performed the simulations, and analyzed the results under the supervision of K. Thornton. S. Kazemiabnavi, B. Orvananos, R. Malik, and A. Abdellahi wrote the manuscript with input from all co-authors. All authors provided critical feedback and helped shape the research, analysis and manuscript.

Chapter 5: K. Thornton and G. Ceder conceived the study. B. Orvananos, R. Malik, and A. Abdellahi derived the initial model and numerical scheme under the supervision of K. Thornton and G. Ceder. S. Kazemiabnavi modified the model and numerical scheme, performed the simulations, and analyzed the results under the supervision of K. Thornton. K. Greenman contributed to performing the simulations and analysis of the results under the supervision of S. Kazemiabnavi and K. Thornton. S. Kazemiabnavi wrote the manuscript with input from all co-authors. All authors provided critical feedback and helped shape the research, analysis and manuscript.

Chapter 6: K. W. Chapman and P. J. Chupas conceived this study. H. Liu, A. Grenier, G. Vaughan, and M. D. Michiel performed the XRD-CT measurement, and G. Vaughan and M. D. Michiel performed the data reduction. S. Kazemiabnavi performed the simulations under the supervision of K. Thornton. B. J. Polzin prepared the thick porous electrode. H. Liu and S. Kazemiabnavi analyzed the experimental and simulation results, respectively, under the supervision of K. W. Chapman, P. J. Chupas, and K. Thornton. H. Liu, K. W. Chapman, and S. Kazemiabnavi wrote the manuscript with contributions from all co-authors.

Chapter 7: N. Dasgupta and J. Sakamoto conceived the presented idea. K. H. Chen, M. Namkoong, and C. Yang carried out the experiments and analyzed the experimental results under the supervision of N. Dasgupta, J. Sakamoto, and J. Mazumder. S. Kazemiabnavi developed the model, performed the simulations, and analyzed the simulation results under the supervision of K. Thornton. S. M. Mortuza contributed to performing the simulations under the supervision of K. Thornton. S. Kazemiabnavi wrote the manuscript with inputs from S. M. Mortuza, K. H. Chen, M. Namkoong, J. Sakamoto, N. Dasgupta, and K. Thornton.

Chapter 2.

Background

In this chapter, we provide a general overview of different battery modeling approaches, and in particular, the underlying physics, assumptions, and governing equations of the pseudo two-dimensional (P2D) model developed by Newman et al. [29, 30], which is extensively used in literature as a comprehensive physics-based approach for modeling batteries.

As one of the primary energy storage solutions, Li-ion batteries play a major role in a wide range of applications from vehicle electrification to powering consumer electronic devices. The optimal design and implementation of Li-ion batteries that are suitable for such a wide range of applications and can operate under various loading conditions, requires extensive experimental characterization and diagnostic efforts to fully comprehend and optimize the electrochemical behavior of its components. The electrochemical modeling of batteries allows for investigating the electrochemical behavior of their components beyond the feasibility, cost, and time constraints of experimental methods. Moreover, battery models can provide predictive information about the electrochemical performance of battery materials under certain operating conditions. Therefore, such models can be used to facilitate the optimal design of rechargeable batteries, while reducing the time and cost associated with the development of their various components.

Reduced-order empirical battery models such as equivalent-circuit models are typically used in battery management systems for battery state of charge and state of health estimation and control [7, 31, 32]. These equivalent-circuit models employ a network of capacitors, resistors, and constant-phase elements to reproduce the observed voltage-current relationship of a battery [7, 33, 34]. While these models are computationally inexpensive, their validity range is limited by the operating conditions in which they have been parameterized. Moreover, these equivalent-circuit models can only relate the voltage and current of a battery and are not capable of predicting the electrochemical state of the internal battery components [7].

On the other hand, physics-based battery models can describe the thermodynamics of the cell, kinetics of the electrochemical reaction at the active particle-electrolyte interfaces, and Li ion transport within the electrolyte and electrode particles. Such models are typically valid over a wide range of operating conditions, and could be directly coupled with other physics such as electrode/electrolyte degradation and heat generation/transfer [7]. The development of accurate physics-based battery models is contingent upon determining the appropriate electrochemical parameters. These parameters are necessary for describing the physical and chemical phenomena that occur during the operation of a battery, which include the evolution of concentration and electrostatic potential in the electrodes and electrolyte, and the electrochemical reactions in the electrodes.

One of the most commonly used physics-based battery models is the pseudo two-dimensional (P2D) model, which is based on the porous electrode theory, both developed by Newman et al. [29, 30, 35]. The P2D model is a continuum-scale electrochemical model that accounts for the dynamics of lithium ion transport and electrostatic potential in the electrode and electrolyte, as well as the electrochemical reactions that occur at the active particle-electrolyte interfaces. The evolution of electrostatic potentials in the electrode and electrolyte, as well as lithium ion transport in the electrolyte occur across the thickness of the cell, which are in macroscale; however, the solid-state lithium transport inside the electrode particles occurs in micro-scale due to the small size of active material particles in the anode and cathode. Therefore, the mathematical treatment of the governing equations for these process needs to be performed at two different length-scales [7].

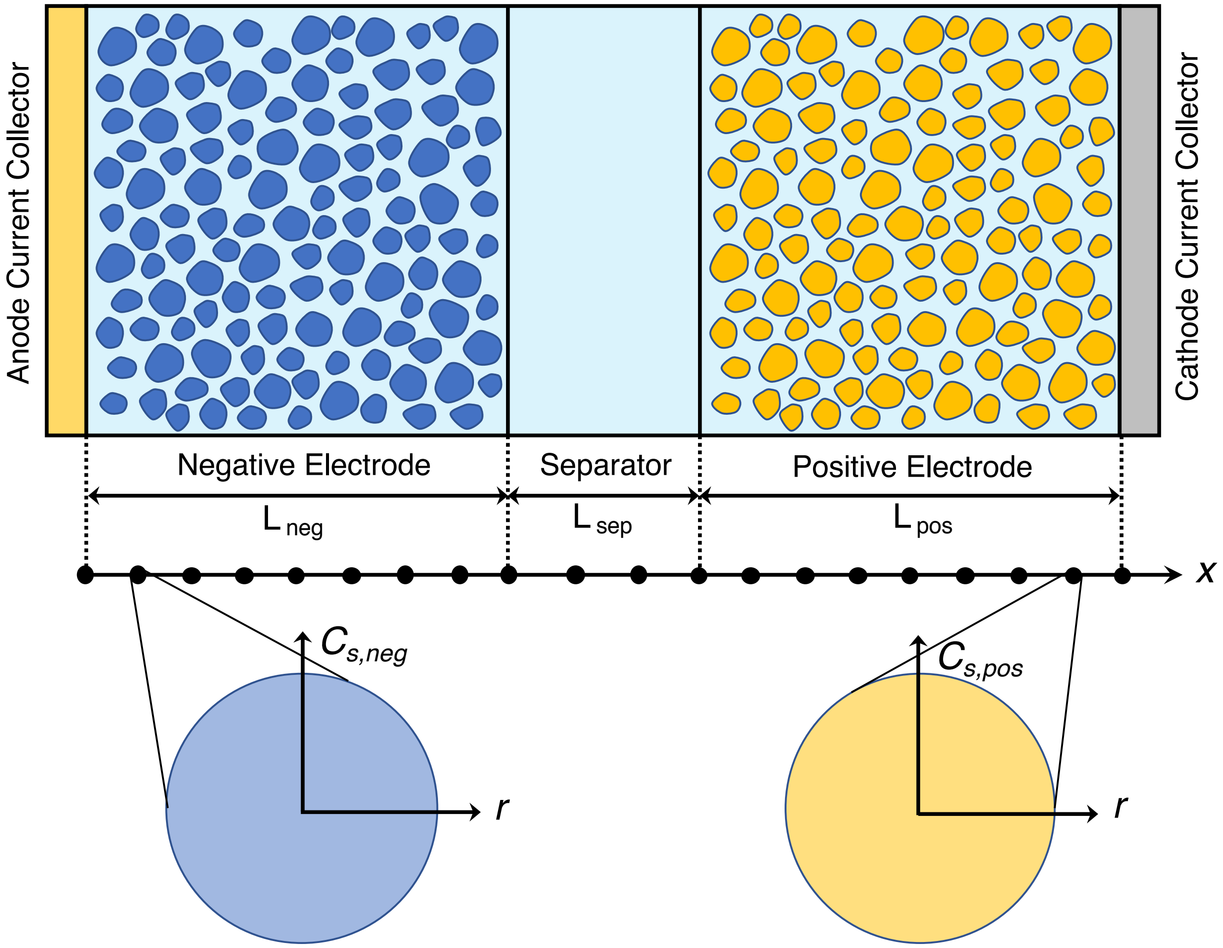

Figure 2.1. A schematic view of the macro- and micro-scale computational domains in the P2D model.

A schematic representation of the computational domain for the P2D model is shown in Figure 2.1. The anode, separator, and cathode subdomains constitute the macro-scale domain of the model. The exact microstructures of the composite electrodes are neglected. Therefore, porous electrode theory [35] is used for the mathematical treatment of the solid and liquid phases in these subdomains as superimposed continua [7]. At each grid point of the anode and cathode subdomains, a one-dimensional micro-scale domain in radial coordinates is considered to model the dynamics of lithium (de)intercalation in the active electrode particles.

The dependent variables in the P2D model are lithium concentration in the solid phase, electrolyte salt concentration, electrostatic potential in the electrolyte, the electrostatic potential in the solid phase at the surface of the particle, and the electrochemical reaction rate. Time and special coordinates across the cell thickness and particle radius are the independent variables [7].

The lithium concentration evolution in the active electrode particles is described by the Fick's second law of diffusion in spherical coordinates [30, 36],

$$\frac{\partial c_{s,i}}{\partial t} = D_{s,i} \frac{1}{r^2} \frac{\partial}{\partial r}\left(r^2 \frac{\partial c_{s,i}}{\partial r}\right) \tag{2.1}$$

where $c_{s,i}$ is the lithium concentration in the solid phase, $D_{s,i}$ is the diffusion coefficient of lithium in the solid electrode particles, and i denotes the positive ($i = p$) or negative ($i = n$) electrodes. Due to the symmetry of the spherical particles, a no-flux (homogenous Neumann) boundary condition is applied to the center of the particle such that $-D_{s,i} \frac{\partial c_{s,i}}{\partial r} = 0$ at $r = 0$ [30, 36]. Since the electrochemical reaction occurs at the particle-electrolyte interface, the flux on the surface of the particles is equal to the reaction rate such that $-D_{s,i} \frac{\partial c_{s,i}}{\partial r} = J_i$ at $r = R_{s,i}$, where J_i is the electrochemical reaction flux at the surface of the particles, and $R_{s,i}$ is the radius of the spherical particles in the anode or cathode [30, 36].

The salt concentration evolution for the binary electrolyte in the liquid phase is described by the porous-medium diffusion equation with an electrochemical reaction source term [30, 36],

$$\varepsilon_i \frac{\partial c_i}{\partial t} = \nabla.\left(D_{eff,i} \nabla \mathrm{c}_i\right) + (1 - t_+^0) a_i J_i \tag{2.2}$$

where ε_i is the porosity, c_i is the concentration of the binary electrolyte, $D_{eff,i}$ is the effective diffusivity of lithium ion in the electrolyte, t_+^0 is the transference number of lithium ion, and $i =$

p, s, and n, denoting positive electrode, separator, and negative electrode, respectively. The variable a_i is the surface area per unit volume of the intercalation particles defined as $(3/R_{s,i})(1-\varepsilon_i-\varepsilon_{f,i})$. The reaction flux is zero in the separator since it is not electrochemically active. No-flux boundary conditions are applied to the electrode-current collector interfaces at the two ends of the cell such that $-D_{eff,n}\nabla c_n\big|_{z=0}=0$ and $-D_{eff,p}\nabla c_p\big|_{z=L_n+L_s+L_p}=0$ [30, 36]. At the positive electrode-separator and the negative electrode-separator interfaces, we assume continuous electrolyte salt concentration and continuous flux, resulting in the following additional boundary conditions [30, 36],

$c_n|_{z=L_n^-}=c_s|_{z=L_n^+}$,

$c_s|_{z=(L_n+L_s)^-}=c_p\big|_{z=(L_n+L_s)^+}$,

$-D_{eff,n}\nabla c_n\big|_{z=L_n^-}=-D_{eff,s}\nabla c_s\big|_{z=L_n^+}$, and

$-D_{eff,s}\nabla c_s\big|_{z=(L_n+L_s)^-}=-D_{eff,p}\nabla c_p\big|_{z=(L_n+L_s)^+}$.

The electrostatic potential in the solid phase, $\phi_{s,i}$, is determined by employing Ohm's law [30, 36],

$$\nabla.\left[\sigma_{eff,i}\nabla\phi_{s,i}\right]=a_iFJ_i \tag{2.3}$$

where F is the Faraday's constant, and σ_{eff} is the effective electrical conductivity of the electrode defined as $\sigma_{eff,i}=\sigma_i(1-\varepsilon_i-\varepsilon_{f,i})$ with $i=p$ and n for positive and negative electrode, respectively. A flux boundary condition is applied to the positive electrode-current collector interface such that the charge flux is equal to the applied current density, I_{app} [30, 36],

$-\sigma_{eff,p}\nabla\phi_{s,p}\big|_{z=L_n+L_s+L_p}=I_{app}$.

A no charge flux boundary condition is applied to the electrode-separator interfaces, which results in the following boundary conditions [30, 36],

$-\sigma_{eff,p}\nabla\phi_{s,p}\big|_{z=L_n+L_s} = 0$, and

$-\sigma_{eff,n}\nabla\phi_{s,n}\big|_{z=L_n} = 0$.

The electrostatic potential at the negative electrode-current collector interface is set to zero, $\phi_{s,n}\big|_{z=0} = 0$, and therefore, the cell voltage will be equal to the electrostatic potential at the positive electrode-separator interface, $E_{cell} = \phi_{s,p}\big|_{z=L_n+L_s+L_p}$[30, 36].

The electrostatic potential in the liquid phase, $\phi_{l,i}$, is governed by the charge balance equation based on Ohm's law [30, 36],

$$-\nabla\left[\kappa_{eff,i}\nabla\phi_{l,i}\right] + \frac{2RT\left(1-t_+^0\right)}{F}\nabla\left[\kappa_{eff,i}\nabla\ln c_i\right] = a_iFJ_i \tag{2.4}$$

where $\kappa_{eff,i}$ is the effective ionic conductivity of the electrolyte, R is the universal gas constant, and T is the temperature. No charge flux boundary conditions are applied to the liquid phase at the electrode-current collector interfaces such that [30, 36],

$-\kappa_{eff,n}\nabla\phi_{l,n}\big|_{z=0} = 0$, and

$-\kappa_{eff,p}\nabla\phi_{l,p}\big|_{z=L_n+L_s+L_p} = 0$.

The electrochemical reaction flux, J_i, in Eq. (2.2)-Eq. (2.4) is determined by the Butler-Volmer equation [8, 30, 36],

$$J_i = i_{0,i}\left[\exp\left(\frac{0.5F}{RT}\eta_i\right) - \exp\left(\frac{-0.5F}{RT}\eta_i\right)\right] \tag{2.5}$$

where the overpotential for the electrochemical reaction, η_i, is defined as $\phi_{s,i} - \phi_{l,i} - U_i$. The exchange current density, $i_{0,i}$, in Eq. (2.5) is defined as [30, 36],

$$i_{0,i} = k_i\left(c_{s,i,max} - c_{s,i,surf}\right)^{0.5} {c_{s,i,surf}}^{0.5} {c_i}^{0.5} \tag{2.6}$$

where k_i is the anodic/cathodic reaction rate constant, $c_{s,i,max}$ and $c_{s,i,surf}$ are the maximum and surface concentration of lithium in the solid electrode particles, respectively.

A slightly modified version of this model that assumes uniform lithium concentration inside the particles is used in chapter 6 to model the reaction heterogeneity in an LFP half-cell. Later in chapter 7, the three-dimensional (3D) form of this full-cell model is used to simulate the electrochemical behavior of highly-ordered hierarchical (HOH) anode under extreme fast charging conditions.

Chapter 3.

Thermodynamics and Kinetics of Nucleation for Electrodeposition on Metal Anodes

Introduction

In this chapter,[*] we utilized the classical theory of nucleation informed by first-principles atomistic simulations to study the nucleation behavior of several metals during electrodeposition on metal anodes. Despite the success of lithium-ion batteries [37-39], demands for higher gravimetric and volumetric energy densities, greater power output, and longer lifetime are driving research into other battery chemistries beyond Li-ion [40]. In this regard, metals are promising candidates for future battery anodes because they have higher theoretical capacities than the graphite-based, intercalation anodes used in lithium ion batteries, Table 3.1. Furthermore, the higher abundance of non-Li metals may result in reduced costs.

The use of metal anodes in rechargeable batteries is not a new idea. Early attempts to commercialize a Li-metal-based cell were unsuccessful due to dendrite growth during charging [41]. More recently, Fluidic Energy™ has commercialized a rechargeable Zn-air battery [42], while Aurbach et al. developed the first rechargeable battery incorporating a Mg metal anode in 2000 [43]. Efforts to improve Mg batteries' capabilities is an active area of research [38, 44, 45]. Al anodes are currently used in primary batteries [46], but the use of an aqueous electrolyte

---

[*] Adapted from K.S Nagy, S. Kazemiabnavi, K. Thornton, and D.J. Siegel, "Thermodynamic Overpotentials and Nucleation Rates for Electrodeposition on Metal Anodes," *ACS Appl. Mater. Interfaces*, 11, 8, (**2019**) 7954-7964. This is an unofficial adaptation of an article that appeared in an ACS publication. ACS has not endorsed the content of this adaptation or the context of its use.

limits rechargeability due to the irreversibility of the Al_2O_3 discharge product. Plating and stripping Al metal anodes using organic-based electrolytes has been largely unsuccessful at room temperature [47, 48], with ionic liquids demonstrating the only evidence to date of cycling [49-51]. Na batteries using molten Na electrodes have been proposed for applications in load-levelling and emergency power [39]. Nevertheless, considerable interest in room temperature Na metal anode batteries also exists, as evidenced by numerous studies on Na-ion, Na-O_2 and Na-S systems [39, 52, 53]. Ren et al. reported a K-O_2 battery which showed a low discharge/charge voltage gap of less than 50 mV during the initial cycle [54], and Zhao et al. reported a K-S battery with impressive initial charge capacity [55]. Earlier attempts to cycle Ca anodes in organic-based solvents proved unsuccessful [56]; however, cycling of Ca metal was recently reported at elevated temperatures [57], and at room temperature [58].

Table 3.1. Properties of candidate negative electrode metals for use in battery applications. Reproduced from Ref. [23].

Anode	Abundance (ppm)	Gravimetric Capacity (mAh/g)	Volumetric Capacity (mAh/cm^3)	Potential vs. SHE (V)
Al	83,176	2980	8046	-1.66
Ca	52,481	1337	2046	-2.87
Mg	32,359	2205	3837	-2.37
Na	22,909	1166	1181	-2.71
K	9,120	685	624	-2.93
Zn	79	820	5846	-0.76
Li	13	3862	2093	-3.04
Graphite	-	300 to 350	790	-2.79 to -2.94

These developments have stimulated the growing interest in batteries that employ metallic negative electrodes. To be viable, metal electrodes should undergo electrodeposition and -dissolution with low overpotentials. For some metals these processes are highly efficient, yet for others achieving efficient cycling is a greater challenge. The experimental overpotential of various metals extracted from cyclic voltammograms reported in this chapter [23] suggest the existence of trends across the various metals. Electrodeposition involving Group I metals, Li, Na, and K, is the most efficient, whereas electrodeposition of Ca is much less so. Mg, Al, and Zn tend to fall between these extremes, with their performance dependent on electrolyte composition, scan rate, and temperature [59, 60].

These observations beg the question: Why are some metals able to plate and strip more easily than others? The overpotentials associated with electrodeposition and -dissolution provide a measure of the efficiency of these processes. In general, these overpotentials can be traced to four contributing processes: charge transfer, mass transport, chemical reaction, and crystallization [61]. As a step towards understanding efficiency differences between different metal electrodes, first-principles calculations can be used to evaluate the thermodynamic overpotentials [62] associated with plating and stripping on several low-energy surfaces of seven metals relevant for battery applications: Li, Na, K, Mg, Ca, Al, and Zn. In this chapter, reactions at terraces and step edges are considered. The thermodynamics factors probed here contribute to the reaction and crystallization components of overpotentials, and reflect heterogeneity in the adsorption/desorption energy of ions arising from inequivalent reaction sites on the electrode surface.

Recognizing that the rate and density of nucleation can affect the evolution of electrodeposits [63-65], steady-state nucleation rates are estimated using a multi-scale approach wherein a classical nucleation model is informed by DFT calculations [66-68]. These simulations allow for a comparison of nucleation rates during electrodeposition on different metallic surfaces and surface features (e.g., terraces vs. step edges).

Surface Energies and Thermodynamic Overpotentials

In order to identify the most likely surfaces of the metal electrodes to be present during electrodeposition, equilibrium crystallite shapes were predicted by constructing Wulff plots from the calculated surface energies of several plausible facets. Surfaces with the largest areal packing densities are typically expected to exhibit the lowest surface energies. As shown in Figure 3.1, the equilibrium crystallite shapes (i.e., Wulff plots) were constructed using the surface energies from DFT calculations. In addition to listing the surface energies obtained from DFT calculations, Table 3.2 tabulates the respective fraction of the crystallite surface area of each facet. Based on the surface energies and areas, σ_{weighted} represents the area-weighted average of the surface energy. This value is expected to be the property most closely resembling experimental measurements of the surface energy in cases where the {*hkl*} index of the surface is not known. Indeed, less than 12% disagreement was observed between σ_{weighted} and the average of the experimental values for each of Al, Ca, Li, Na, and Mg. The discrepancy between theory and experiment is larger for potassium (~20%) and Zn (>40%). The absolute values for the surface energy of K are smaller than the other metals considered here, so a small variation yields a greater percentage error.

There are several possible explanations for the discrepancies be-tween the experimental and calculated surface energy of Zn, one of which is the experimental method used to obtain the surface energies. For example, Tyson [69] established a linear correlation between cohesive energy at 0 K and surface energy, while de Boer et al. [70] established a linear trend between enthalpy of vaporization and surface energy. It has been noted [71, 72] that these methods use observables which are referenced to elements in the gas phase, which in the case of the divalent metals Hg, Cd, Mg, and Zn, leads to significant errors in the resulting surface energies.

Furthermore, the experimental values use surface tensions measured at high temperatures, but then extrapolate to 0 K [69, 71, 72]. Additionally, several authors [73, 74] have noted that experimentally determined surface energies are generally larger than those predicted by calculations. This results from the presence of surface defects, and the experimental surfaces being a mixture of several crystallographic planes.

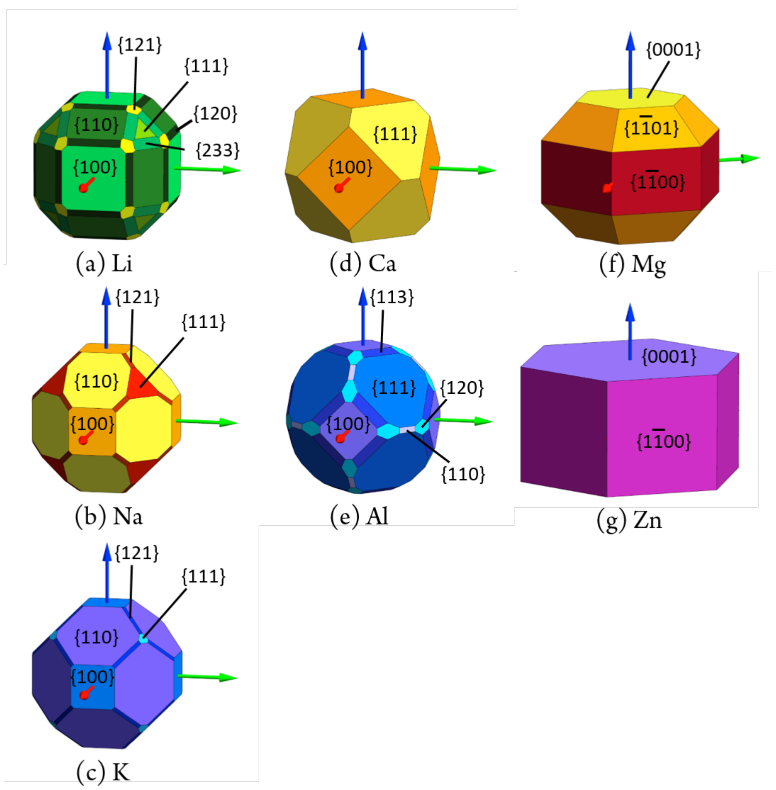

(a) Li (d) Ca (f) Mg

(b) Na (e) Al (g) Zn

(c) K

Figure 3.1. Wulff plots for (a) Li, (b) Na, (c) K, (d) Ca, (e) Al, (f) Mg, and (g) Zn. At ambient conditions (a) – (c) adopt the BCC crystal structure, (d) – (e) adopt the FCC structure, and (f) – (g) are HCP. Reproduced from Ref. [23].

Table 3.2. Calculated surface energies (σ) for a given {*hkl*} surface facet, the equilibrium area fraction of each facet as determined by the Wulff construction, and the area-weighted surface energy, σ_{weighted}. Reproduced from Ref. [23].

Metal	**{*hkl*}**	**$\sigma_{\text{calculated}}$ (J/m^2)**	**Area Fraction**	**σ_{weighted} (J/m^2)**	**Expt. Values (J/m^2)**
Al	{100}	1.05	0.17	1.01	1.14 [75]
	{110}	1.14	0.02		
	{111}	0.96	0.57		
	{120}	1.13	0.09		
	{113}	1.09	0.15		
	{133}	1.12	-		
Ca	{100}	0.49	0.43	0.50	0.50 [69]
	{110}	0.58	-		
	{111}	0.50	0.57		
	{120}	0.59	-		
	{113}	0.57	-		
	{133}	0.56	-		
Li	{100}	0.49	0.33	0.52	0.52 [69]
	{110}	0.53	0.33		
	{111}	0.56	0.04		
	{114}	0.55	-		
	{120}	0.54	0.13		
	{121}	0.57	0.06		
	{233}	0.57	0.10		
Na	{100}	0.24	0.20	0.24	0.24 [75]
	{110}	0.23	0.67		
	{111}	0.25	0.09		
	{114}	0.26	-		
	{120}	0.30	-		
	{121}	0.26	0.04		
	{233}	0.26	-		
K	{100}	0.12	0.17	0.11	0.13 [75]
	{110}	0.11	0.77		
	{111}	0.13	0.01		
	{114}	0.13	-		
	{120}	0.13	-		
	{121}	0.13	0.05		
	{233}	0.13	-		
Mg	{001}	0.59	0.17	0.69	0.76 [70]
	$\{1\bar{1}0\}$	0.70	0.37		
	$\{1\bar{1}1\}$	0.71	0.46		
	{110}	0.85	-		
	{111}	0.84	-		
Zn	{001}	0.41	0.46	0.57	0.92 [75]
	$\{1\bar{1}0\}$	0.71	0.54		
	$\{1\bar{1}1\}$	0.80	-		

The calculation of thermodynamic overpotentials has been used extensively to examine electrocatalysts [76-78] and metal-air batteries [62, 74]. The calculated overpotentials from these studies generally agree well with experimentally observed overpotentials. In this chapter, the overpotential contributions during the electrodeposition and -dissolution of metal ions at metallic negative electrodes in batteries is explored. The goal is to examine trends in the thermodynamic overpotentials and nucleation rates as a function of anode composition and surface structure, the latter including various surface facets and adsorption/desorption sites.

Our calculations consider terrace and step sites on the electrode surface. In prior studies [62, 79] it was observed that application of the thermodynamic overpotentials method at terrace sites alone led to an overestimation of the overpotential; electrochemical reactions at step and kink sites yielded predictions more in line with experimental data. Nevertheless, it has also been suggested [80, 81] that at high current densities the overpotentials resulting from charge transfer at terrace sites can contribute to the overpotential when a large number of terrace sites are available. Additionally, the limited time available for surface diffusion under high current densities implies that not all electrodeposited ions will have sufficient time to migrate to low-energy step/kink sites. Thus, it is reasonable to examine behavior at both terrace and kink sites.

DFT simulations of sequential adsorption-relaxation processes of metal atoms on the abovementioned surfaces show that the initial deposition step onto an empty terrace is consistently the most endergonic step. This results from the initial deposition site presenting the least number of nearest neighbors for bonding. This step nucleates a new, single-atom island on top of an existing terrace. Similarly, the final deposition step that forms a complete monolayer, is consistently the most exergonic step since the depositing atom has the maximum number of nearest neighbors available for bonding.

The thermodynamic overpotentials obtained from DFT calculations for electrodeposition on several low-energy surfaces of the seven metals are shown in Figure 3.2. The data are grouped by metal and arranged for a given metal according to increasing surface energy. The thermodynamic overpotentials for terrace reactions are represented by the orange bars for the deposition process and overlaid blue cross-hatching for the dissolution process. The facets examined for thermodynamic overpotentials were those with the largest areal fractions: {111} and {100} for Al and Ca; {110} and {100} for Li, Na, and K; {001}, $\{1\bar{1}0\}$, and $\{1\bar{1}1\}$ for Mg; {001} and $\{1\bar{1}0\}$ for Zn. Additionally, deposition on stepped surfaces was also considered. Step morphologies were approximated using {210} surfaces for BCC metals, {212} for FCC metals, and $\{10\bar{1}7\}$ for HCP metals.

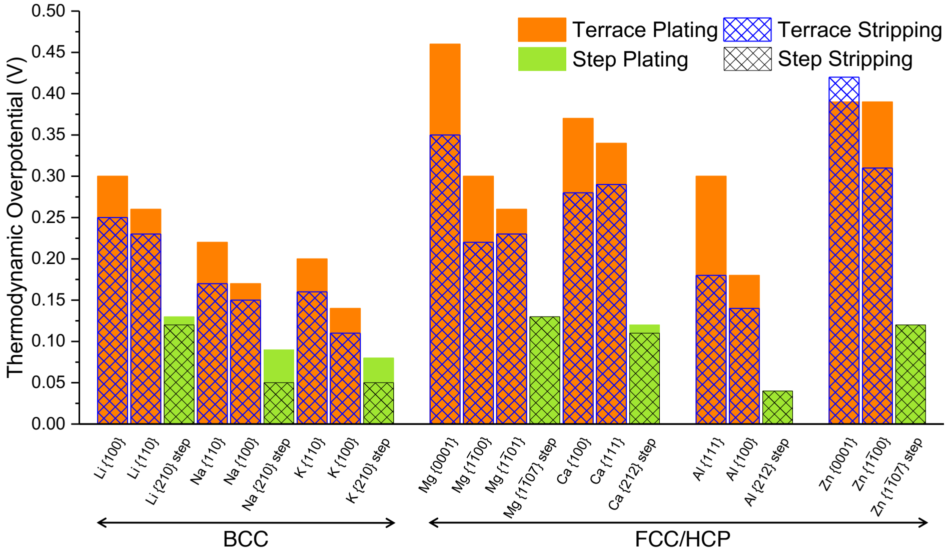

Figure 3.2. Thermodynamic overpotentials obtained from DFT calculations for electrodeposition and -dissolution on 7 metals as a function of surface facet and surface morphology (terraces vs. steps). Facets of a given metal are arranged according to ascending surface energy, and metals are grouped by column of the periodic table. Solid orange/green bars represent plating overpotentials on terraces/steps; cross-hatched bars represent stripping overpotentials on terraces and steps. For simplicity, only the absolute value of the overpotential is plotted. Reproduced from Ref. [23].

The data in Figure 3.2 shows that the calculated thermodynamic overpotentials on stepped surfaces is smaller than those on terraced surfaces. This trend can be understood using a simple bond-counting argument: adsorption at a step-edge or kink presents a larger number of coordinating atoms compared to adsorption on a terrace. A second trend in the data pertains to the Group I metals, Li, Na, and K, which generally exhibit lower thermodynamic overpotentials compared to the Group II metals (Ca and Mg), Group III metal (Al), and the transition metal (Zn). This trend is in agreement with the experimental overpotentials[23].

To explain the lower overpotentials observed for the alkali metals, we recall that they crystallize in the BCC structure, while the other metals adopt FCC or HCP lattices. BCC bulk atoms have a coordination number (CN) of 8, while the close-packed FCC and HCP systems the atoms have CN = 12. Focusing on deposition, we recall that the thermodynamic overpotential is determined by the initial deposition event. Therefore, the origin of the relatively lower overpotential for the alkali metals should be tied to the bonding environment of these initially deposited adatoms. These adatoms are coordinated by 4 or 5 nearest neighbors on the {110} and {100} surfaces, respectively. In contrast, the CNs for adatoms on the FCC and HCP metals (Mg, Ca, Al, Zn) are at best similar to the BCC surfaces, and are often smaller: CN = 3 on the close-packed {111} and {0001} surfaces; CN = 4 on the FCC {100} surfaces and on Mg $\{1\bar{1}00\}$ and $\{1\bar{1}01\}$; CN = 2 on Zn$\{1\bar{1}00\}$. Comparing the bulk CNs to the CNs of the initially deposited adatoms, we note that the BCC alkali metals have the smallest surface-to-bulk CN difference. In other words, the surface bonding environment experienced by the alkali metals adatoms is more similar to their bulk-like coordination than in the FCC or HCP systems. This similarity results in relatively lower thermodynamic overpotentials for the alkali metals. A similar argument based on CN has been invoked to explain differences in dendrite formation tendencies during electrodeposition of metals [82].

Additional trends apparent in Figure 3.2 relate to the surface energy and the asymmetry between deposition and dissolution. Regarding surface energy effects, we note that the thermodynamic overpotential generally decreases with increasing surface energy. In the case of deposition, this trend can be rationalized by recognizing that the atoms comprising a high-energy facet are more reactive to (i.e., more readily bond with) adatoms. In the case of stripping and assuming a simple picture of surface energetics that depends only on bond counting, it will be energetically easier to remove an atom from a high surface energy facet due to the fewer number of bonds that must be broken (relative to a more stable surface). This qualitatively explains the reduction in thermodynamic overpotential for stripping from higher surface energy facets.

Steady-State Nucleation Rates

According to classical nucleation theory [83, 84], the time-dependent nucleation rate, $J(t)$, can be expressed in terms of an induction time, τ, and the steady-state nucleation rate, J_0, using Eq. (3.1) [83]:

$$J(t) = J_0\left[1 + 2\sum_{n=1}^{\infty}(-1)^n \exp\left(\frac{-n^2 t}{\tau}\right)\right] \tag{3.1}$$

where J_0 is expressed as [84]:

$$J_0 = N\left(\frac{\omega_c}{g_c}\right)\left(\frac{\Delta G_c}{3\pi k_B T}\right)^{1/2} \exp\left(\frac{-\Delta G_c}{k_B T}\right) \tag{3.2}$$

Here, N is the total number of atoms per unit surface area of the electrode that can contribute to the formation of nuclei. Assuming that a layer of the electrolyte in the vicinity of the electrode contributes directly to the nucleation, N can be calculated using $N = N_A . C_0 . d$, where N_A is Avogadro's number, C_0 is the electrolyte concentration (1000 mol/m^3), and d is the thickness of the layer of electrolyte in the vicinity of the electrode (assumed 10 Å for all cases).

ΔG_c is the formation energy of the critical nucleus, g_c is the number of atoms in the critical nucleus, and ω_c, is the frequency of collision of the atoms with the critical nucleus.

In classical nucleation theory the formation energy of the cluster is assumed to be separable into bulk free energy and surface free energy terms [85]. This assumption holds as long as the cluster is large enough to distinguish between its surface and bulk regions. However, very small clusters do not satisfy these criteria; the cluster does not necessarily take the crystal structure of the bulk phase, and no clear differentiation between the bulk and surface energy contributions can be made. Therefore, an atomistic approach is necessary to determine the formation energies of clusters that are on the nanoscale. As described previously in this chapter, the deposition of the first adatom on the electrode surface is consistently the most endergonic electrodeposition step, independent of surface composition or structure (terrace or step). This behavior suggests that the critical cluster size should be taken as a single atom. Similarly, ΔG_c is defined in Eq. (3.2) to be the reaction energy of the deposition of the initial adatom at either a terrace or step.

In the case of nucleation during electrodeposition process, assuming the process in controlled by the kinetics of the electrochemical reaction and not by the diffusion of atoms on the surface, the frequency of collision of the atoms with the critical nucleus, ω_c in Eq. (3.2), is defined as $S_c i_0/ze$, in which S_c is the surface area of the critical nucleus, i_0 is the exchange current density [85]. Moreover, under an applied potential, U_{app}, the formation energy of the critical nucleus, ΔG_c, can be written as [85]:

$$\Delta G_c = -ze\left(\eta_{dep} - U_{app}\right) \tag{3.3}$$

where η_{dep} is the thermodynamic overpotential for electrodeposition obtained from DFT calculations. The calculated steady-state nucleation rate and formation energy of the critical nucleus for electrodeposition on terrace and step sites at an applied potential of −10 mV are listed in Table 3.3.

Table 3.3. Calculated steady-state nucleation rate and critical formation energy for electrodeposition on terrace and step sites at an applied potential of −10 mV. Reproduced from Ref. [23].

	Metal	**Critical Formation Energy (eV)**	**Steady-State Nucleation Rate ($s^{-1}.cm^{-2}$)**
Terrace	Li{100}	0.29	3.72×10^{9}
	Li{110}	0.25	1.64×10^{10}
	Na{110}	0.21	1.07×10^{11}
	Na{100}	0.16	6.54×10^{11}
	K{110}	0.19	3.30×10^{11}
	K{100}	0.13	2.82×10^{12}
	Mg{0001}	0.89	2.57×10^{-1}
	Mg{1$\bar{1}$00}	0.58	3.63×10^{4}
	Mg{1$\bar{1}$01}	0.50	7.60×10^{5}
	Ca{100}	0.72	2.63×10^{2}
	Ca{111}	0.66	2.61×10^{3}
	Al{111}	0.86	4.33×10^{-1}
	Al{100}	0.51	2.77×10^{5}
	Zn{0001}	0.76	2.63×10^{1}
	Zn{1$\bar{1}$00}	0.75	3.86×10^{1}
Step	Li{210}	0.12	1.80×10^{12}
	Na{210}	0.09	7.50×10^{12}
	K{210}	0.07	2.14×10^{13}
	Mg{1$\bar{1}$07}	0.24	1.31×10^{10}
	Ca{212}	0.23	2.88×10^{10}
	Al{212}	0.09	1.48×10^{12}
	Zn{1$\bar{1}$07}	0.21	2.77×10^{10}

Figure 3.3 shows the steady-state nucleation rate as a function of critical formation energy for plating on step and terrace sites calculated using the thermodynamic overpotentials from DFT as input to Eq. (3.1). The relatively small thermodynamic overpotential predicted for the alkali metals (Li, Na, and K) generally results in higher steady-state nucleation rates compared to the other metals, regardless of whether plating occurs on terraces or at steps. However, as discussed earlier and as demonstrated in Figure 3.2, the thermodynamic

overpotential for plating at step sites is smaller than that on terrace sites. This results in a steady-state nucleation rate that is several orders of magnitude higher at steps compared to terrace sites, independent of the choice of metal. This is attributed to the exponential relationship between the reaction energies of initial deposition and the nucleation rate as defined by Eq. (3.2). The relative ordering of the surfaces/metals with respect to their nucleation rate is similar for step and terrace deposition sites. Nevertheless, the rates on the step sites are more tightly clustered, suggesting that deposition in these cases is less sensitive to the metal's composition.

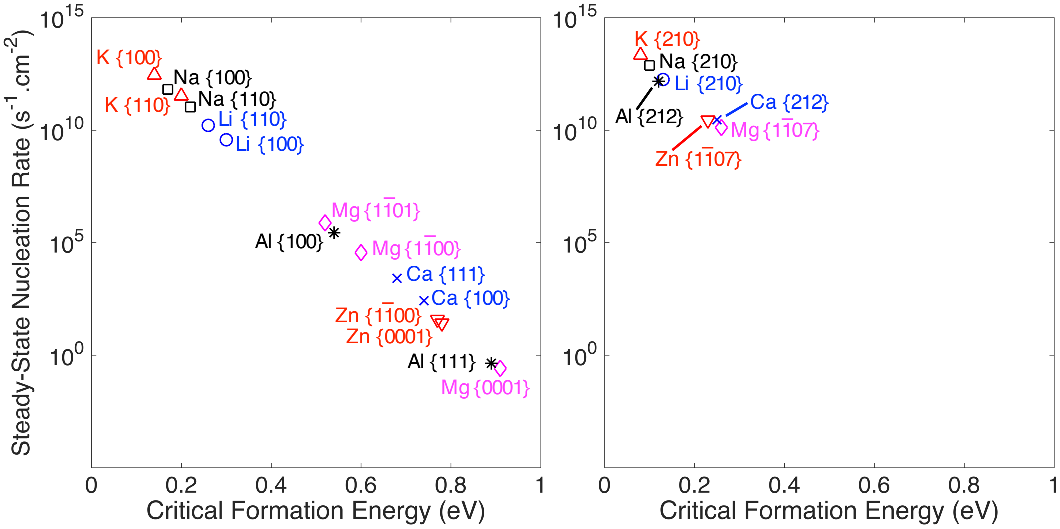

(a) (b)

Figure 3.3. The steady-state nucleation rate as a function of critical formation energy for plating on (a) terrace and (b) step sites. Due to their smaller critical formation energy, alkali metals are predicted to have higher steady-state nucleation rates compared to other metals. The exponential relationship between these quantities results from Eq. (3.2). Reproduced from Ref. [23].

Figure 3.4 shows the calculated steady-state nucleation rates as a function of free surface energy for plating on terrace and step sites. This figure illustrates that for each metal, the steady-state nucleation rate is higher on surfaces with a higher free surface energy. We previously noted that the thermodynamic overpotential decreases with increasing surface energy. Therefore, the formation energy of the critical nucleus is smaller on facets with a higher free surface energy, resulting in a higher nucleation rate on these facets. This is due to the fact that the atoms comprising a high-energy facet are more reactive to (i.e., more readily bond with) adatoms.

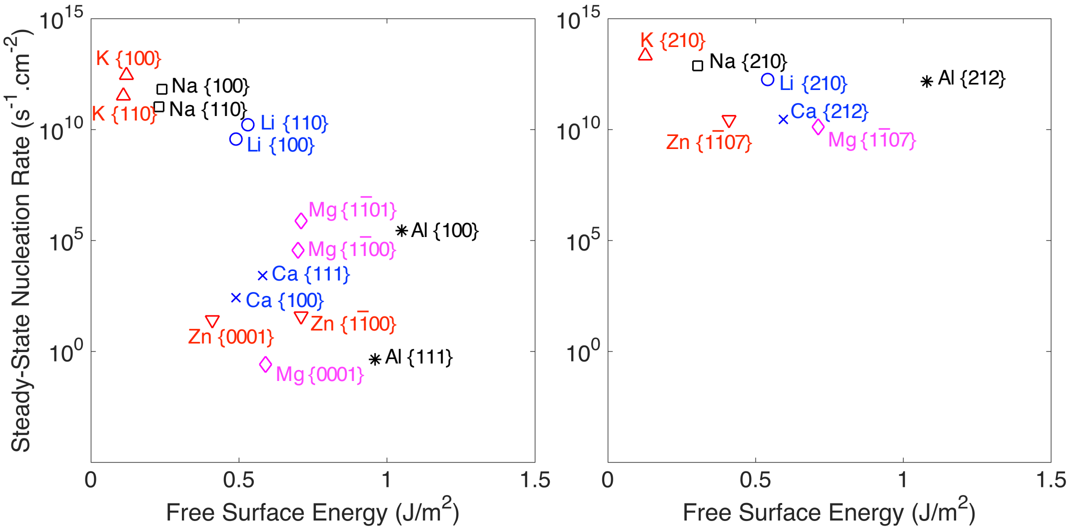

Figure 3.4. The steady-state nucleation rate as a function of free surface energy for plating on (a) terrace and (b) step sites. For each metal, the steady-state nucleation rate is higher on surfaces with a higher free surface energy. Reproduced from Ref. [23].

Figure 3.5 shows the steady-state nucleation rate as a function of applied potential for electrodeposition on terrace and step sites. This figure illustrates that the nucleation rate increases with the application of a more negative potential, as expected. The slope of each line is proportional to the number of transferred electrons, z, during the electrochemical reduction of the corresponding metallic ion. By applying a negative potential, U_{app}, the formation energy of the critical nucleus decreases by zeU_{app}, which exponentially increases the steady-state nucleation rate.

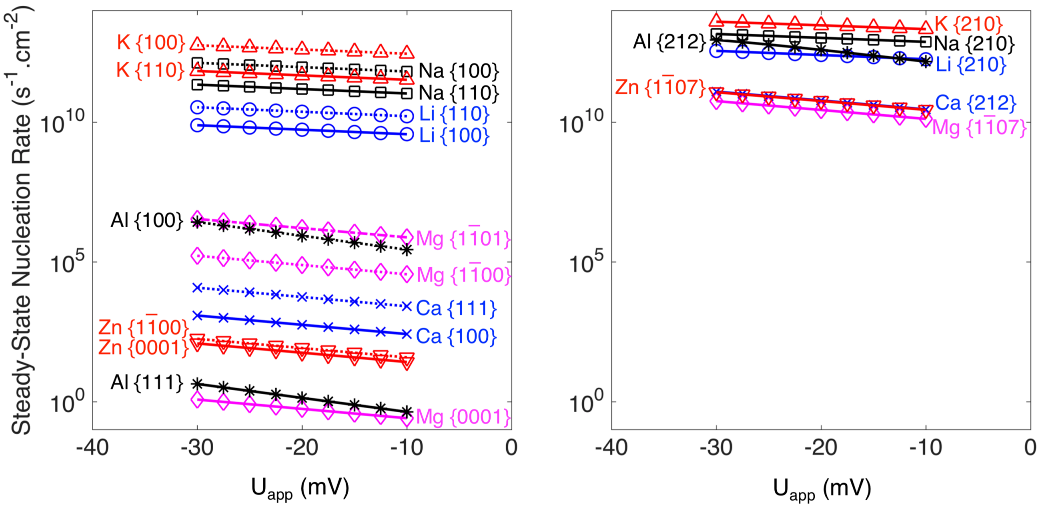

(a) (b)

Figure 3.5. Steady-state nucleation rate as a function of applied potential, U_{app}, for plating on (a) terrace and (b) step sites on seven metal negative electrodes. U_{app} is varied from -30 to -10 mV vs. the corresponding equilibrium potential for each metal. Reproduced from Ref. [23].

There has been a number of studies indicating that the nucleation density is among the key parameters that govern how lithium plates during electrodeposition, along with electrochemical parameters such as current density. It was theoretically predicted through mesoscale simulations of lithium dendrite growth that more uniform deposition can be achieved when nuclei are more densely distributed; if the nuclei are sufficiently close together for a given electrochemical condition, the initial growth results in impingement and subsequent stable growth [86]. Experimentally, the effect of nucleus density on plating behavior has been examined by Garcia et al. [87], who reported complete prevention of dendrite formation in Zn metal anodes by introduction of nucleation pulse to increase the initial coverage of Zn nuclei. More recently, Rehnlund et al. showed that dendrite-free stable lithium deposition can be achieved by using a decreased lithium salt concentration and a short lithium nucleation pulse, which resulted in an increased lithium nuclei density on the electrode surface [88]. Our findings provide quantitative, material-specific data that support the observed dendrite suppression in some metals and will enable suppression in others.

Summary and Conclusions

The thermodynamic overpotentials obtained from DFT calculations for seven metals (Li Na, K, Mg, Ca, Al, and Zn) considered as potential anodes for future rechargeable batteries were investigated. The magnitude of the calculated overpotentials are in many cases similar to measured values, and range from tens to hundreds of mV. These calculations also provide insight regarding the inefficiencies associated with electrodeposition of Ca and Mg: the calculated overpotentials for these metals are amongst the largest overall, consistent with measurements.

We observe that the metal's crystal structure correlates with the efficiency of plating and stripping: body-centered cubic alkali metals are predicted to be among the most efficient systems, whereas the remaining metals, all of which possess close-packed crystal structures, are predicted to have higher thermodynamic overpotentials. As expected, electrodeposition/-dissolution is most efficient at kink sites on steps, while undercoordinated terrace sites yield the largest thermodynamic overpotentials. Trends involving surface energies are discussed. Differences between the calculated overpotentials and experimental measurements highlight the importance of kinetic factors (which are not accounted for in the present approach), such as ohmic resistance in electrolytes, diffusion through solid electrolyte interphases, surface diffusion, electron transfer, etc.

Steady-state nucleation rates were estimated using a classical nucleation model informed by the present DFT calculations. These simulations allow for a comparison of electrodeposition nucleation rates on different metallic surfaces and surface features (e.g., terraces vs. step edges). The small thermodynamic overpotentials predicted for plating at step edges results in higher nucleation rates at these features, suggesting that a large population of kink sites will promote efficient cycling. Nucleation rates on terraces differ by several orders of magnitude across the metals, with rates on the body-centered cubic metals predicted to be fastest. In contrast, nucleation rates at step edges are within a few orders of magnitude of each other, indicating a weak dependence on metal composition. This approach demonstrates a technique for linking atomistic data with a continuum nucleation model, and highlights the sensitivity of nucleation behavior on the structure and composition of the electrode surface.

Chapter 4.

The Effect of Surface-Bulk Potential Difference on the Kinetics of Intercalation in Core-Shell Active Cathode Particles

Introduction

In this chapter,[*] a one-dimensional continuum-scale model is developed to investigate the galvanostatic charge/discharge behavior of cathode particles with a core-shell heterostructure. During the past few past few decades, rechargeable batteries have received significant scientific attention since they show great promise as a reliable energy storage solution for a wide variety of applications ranging from electric powertrain systems to consumer portable electronics [1, 2]. The scientific community has shown increasing interest in exploring new chemistries for lithium batteries such as lithium-sulfur [89, 90] and lithium-air batteries [17, 19, 91, 92]. Enhancing the performance of such rechargeable batteries requires material design for various battery components such as electrochemically stable electrolytes, high-capacity anodes, and high-voltage cathodes [21, 93]. Developing new cathode materials with improved electrochemical performance, low cost, and enhanced cycle life is critically important in achieving the requirements for transportation applications [94].

Recent studies have confirmed that, in general, surface modification of the active cathode particles affects the capacity retention, rate capability and even thermal stability of the cathode

---

[*] Adopted from S. Kazemiabnavi, R. Malik, B. Orvananos, A. Abdellahi, G. Ceder, and K. Thornton, "The Effect of Surface-Bulk Potential Difference on the Kinetics of Intercalation in Core-Shell Active Cathode Particles," *J. Power Sources*, 382 (**2018**) 30-37.

materials for lithium-ion batteries [95, 96]. This surface modification can be done by coating the particles with a protective layer, in which case, the coating must guard the core material against side reactions with the electrolyte and prevent the loss of transition-metal ions or oxygen, without significantly affecting the electronic and ionic conductivities [97].

In the field of lithium-ion battery research, nanoscale coatings or encapsulating phases on active cathode materials are ubiquitous, either by design to improve performance or through "in-situ" evolution [97-99]. For instance, carbon coating on $LiFePO_4$ is widely used to improve surface conductivity and electron transfer kinetics [95, 100, 101]. Jeong et al. [102] have recently used an oxide coating on $LiMn_2O_4$ spinel particles to mitigate the dissolution of Mn^{2+} into the electrolyte. The surface of the cathode particles can also be coated with another active material to create dual-active-material cathode particles with a core-shell heterostructure. For example, Shim et al. [103] have reported on the successful implementation of a thin spinel $Li_xCo_2O_4$-coated $LiCoO_2$ prepared by post-thermal treatment. They demonstrated that the high electrical conductivity of the coating layer enhances the charge transfer activity of the cathode material. In a recent study by Jing Li et al. [104] lithium-rich Ni-Mn-Co oxide core-shell electrodes with an Mn-rich shell were used to prevent the Ni from reacting with the electrolyte. Zaghib et al. [105] introduced a new cathode material by encapsulating $LiMnPO_4$ with $LiFePO_4$ to improve its thermal stability and to facilitate carbon coating of the particles.

Surface coating can also be used to decrease the rate of side reactions that lead to the degradation of the electrolyte or active electrode material. For instance, charged electrode materials such as delithiated cathodes tend to violently react with the non-aqueous electrolytes at elevated temperatures [106, 107]. These side reactions can still occur slowly at room temperature, resulting in gradual degradation of cathode materials [95]. By creating an artificial physical barrier that increases the activation energy for such side reactions, it is possible to effectively decrease the rate of these reactions at ambient temperatures.

As mentioned, encapsulating phases on active cathode particles may form “in-situ.” For instance, Kikkawa et al. [108] observed $CoO_{2-\delta}$ $(0.67 < \delta < 1)$ forming on the surface of $LiCoO_2$ particles upon overcharge. Recently, Lee et al. introduced lithium-excess nickel titanium molybdenum oxides as a new class of high capacity cation-disordered oxides for use in rechargeable lithium battery cathodes [109]. They showed that $Li_{1.2}Ni_{1/3}Ti_{1/3}Mo_{2/15}O_2$ (LNTMO20) provides the best performance among Li-excess Ni-Ti-Mo oxides. However, galvanostatic discharge tests at different rates indicated that its discharge capacity decreases from $250\ \mathrm{mAh/g}$ to $120\ \mathrm{mAh/g}$ as the rate increases from $10\ \mathrm{mA/g}$ to $400\ \mathrm{mA/g}$ [109]. Lee at al. [109] showed that the surface phase that formed during the first charge of LNTMO20 particles was responsible for this reduction in capacity at high C-rates.

The formation of solid-electrolyte interphase (SEI) layer on the surface of cathode particles is another example of in-situ evolution of encapsulating phases that can potentially result in capacity reduction. For instance, Bian et al. [110] observed that a thick SEI layer (>10 nm) forms on the surface of cycled $Li(Li_{0.18}Ni_{0.15}Co_{0.15}Mn_{0.52})O_2$ (LLMO) Li-excess cathode particles, which causes a significant capacity drop (~50%) after only 100 cycles at 0.2C rate. They also showed that BiOF-coated LLMO particles exhibit a dramatically reduced (~10%) capacity drop under the same conditions, which was attributed to very thin SEI layers (~3 nm) that formed on the BiOF-coated particles [110].

Identifying the sources of capacity drop in Li-excess compounds is crucial in the development of next-generation high-energy-density cathode materials [111]. In general, any difference in the material and geometrical properties of the surface and bulk phases, such as open-circuit voltage (OCV), Li diffusivity, reaction coefficient, and thickness, can potentially affect the charge/discharge behavior of core-shell cathode particles [112]. We hypothesize that the poor kinetic behavior of core-shell cathode particles is caused by either low diffusivity in the surface layer as shown by Lee et al. [109] in the case of Li-excess materials, or a shift in the OCV of the surface phase. While both mechanisms can occur simultaneously, in order to investigate which mechanism has a greater impact on the intercalation kinetics, the effect of each mechanism needs to be studied separately. Since the effect of a small Li diffusion coefficient on the kinetic behavior of core-shell cathode particles is more obvious, in this paper we focus on the effect of OCV shift in the surface phase. Below, a simple but general continuum model is formulated to study the lithium intercalation kinetics of a particle with a core-shell heterostructure. This model will allow us to evaluate the charge/discharge overpotential in dual-active-material core-shell particles and to demonstrate that this shift in the surface-phase OCV may be responsible for the observed electrochemical behavior of high capacity Li-excess cathode materials.

Electrochemical Model

The model particle with a core-shell heterostructure, illustrated schematically in Figure 4.1 is comprised of two active materials: a core material with open circuit voltage V_o encapsulated by a thin layer of a second phase with a shifted open circuit voltage $V_o + \Omega$. The charge/discharge of a Li-ion battery cell is a result of multiple physical and chemical mechanisms that occur simultaneously in the electrode, liquid electrolyte and their interfaces. These mechanisms include i) ionic transport in the electrolyte, ii) current continuity in the ionically conductive electrolyte, iii) electrochemical reaction(s) at the particle-electrolyte interfaces, iv) Li ion transport in the electrode particles, and v) current continuity in the electronically conductive solid phases. The first two mechanisms take place in the electrolyte, while the last two processes occur in the cathode particles. The reaction (iii) arises on the interface between the electrolyte and cathode particles. The details and mathematical descriptions of these processes are described below.

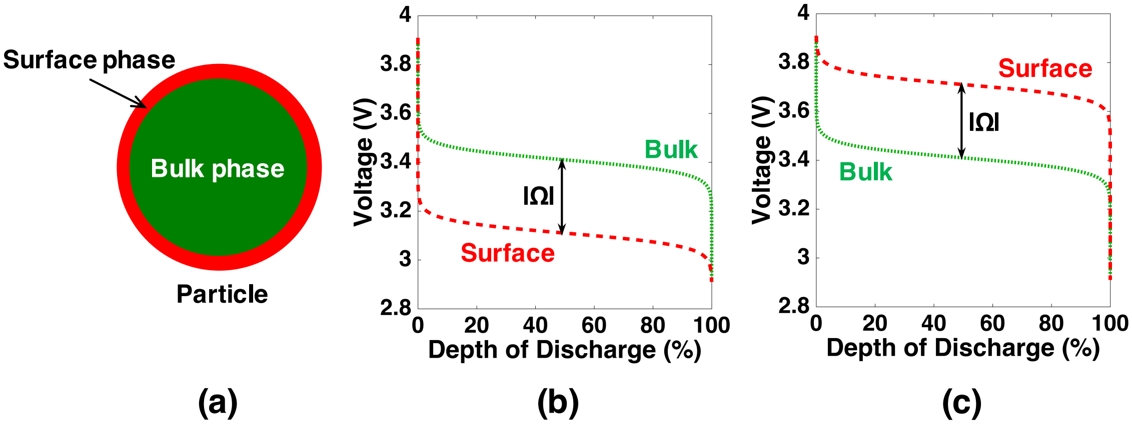

Figure 4.1. (a) Schematic illustration of a core-shell active particle. The corresponding open circuit voltages of the bulk phase (green) and surface phase (red) for a particle with (b) $\Omega < 0$ and (c) $\Omega > 0$. Reproduced from Ref. [27].

During the discharge of a lithium-ion battery, lithium is oxidized at the anode and the resulting Li ions travel through the electrolyte towards the cathode electrode. At the cathode-electrolyte interface, these Li ions react with the electrons and intercalate into the host crystal. The intercalation reaction is described by the chemical equation:

$$Li^{+} + e^{-} + X \longrightarrow LiX \tag{4.1}$$

where X represents the unit formula for the cathode host compound. The reverse reaction occurs when potential is applied to charge the cell. In this study, we do not consider side reactions such as those that form solid-electrolyte interphase (SEI) or that lead to decomposition of electrode particles and/or the liquid electrolyte. We also assume the reaction-limited regime in the electrolyte (i.e., the mass transport in the electrolyte is rapid in comparison to the charge-transfer kinetics), and therefore ignore the diffuse double layers [8].

For simplicity and computational efficiency, we assume the geometry of the core-shell cathode particle to be spherical so that the dynamics can be described by one-dimensional (1D) equations in radial coordinates. The core phase is encapsulated by an outer shell with a shifted OCV. We also assume that both phases have constant thickness (i.e., no phase evolution) with constant electrostatic potential field (i.e., the particle has sufficiently high electronic conductivity). Therefore, we construct a 1D model of a particle of radius R with surface-phase of thickness Δ, as illustrated in Figure 4.2.

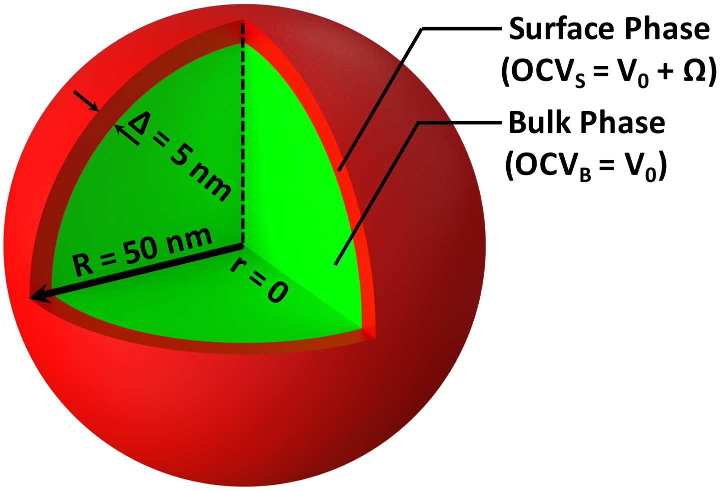

Figure 4.2. The 1D model system for a particle of radius R and surface thickness Δ assuming spherical symmetry. Reproduced from Ref. [27].

At the particle-electrolyte interface, we model the charge-transfer reaction rate with Butler-Volmer kinetics [8], and Li transport within the particle with linear diffusion [113]. We reformulate these governing partial differential equations using the smoothed boundary method (SBM) [114], which has been applied to simulations of lithiation/delithiation of Li intercalation systems [115-117]. In this work, SBM is used to explicitly distinguish phases (the surface, bulk, and electrolyte phases) in the model system.

The electron-transfer reaction between Li$^+$ ions in the electrolyte and the electrons in the cathode particles occurs at the particle-electrolyte interfaces. The rate of this reaction, R_{rxn}, can be modeled using the Butler-Volmer equation [8], expressed as:

$$R_{rxn} = \frac{i_0}{F}\left[\exp\left(-\frac{\alpha F}{RT}\eta\right) - \exp\left(\frac{(1-\alpha)F}{RT}\eta\right)\right] \tag{4.2}$$

where i_0 is the exchange current density, F is Faraday's constant, α is the charge transfer coefficient, R is the universal gas constant, and T is the temperature. The overpotential, η, is defined as $\phi_p - \phi_e + \mu/F$, in which ϕ_p and ϕ_e are the electrostatic potential of the particle and the electrolyte, respectively. The electrostatic potentials are assumed to be uniform throughout the particle. V_{oc} is the open circuit voltage, which is the function of Li concentration in the particle, and μ is the chemical potential of Li in the particle.

When Li atoms intercalate into cathode particles, they diffuse through the interstitial sites of the host crystal lattice. The Li atom transport in the cathode particles can be described by the SBM formulation of the diffusion equation expressed in terms of the chemical potential with the reaction rate as a boundary condition at the particle-electrolyte interface to account for the electrochemical insertion [114]:

$$\frac{\partial C}{\partial t} = \frac{1}{r^2\psi_p}\frac{\partial}{\partial r}\left(r^2\psi_p M\frac{\partial \mu}{\partial r}\right) + \frac{|\nabla\psi_p|}{\psi_p}R_{rxn} \tag{4.3}$$

where r is the radial coordinate, C is the concentration of Li in the particle, t is time, and M is the Li transport mobility inside the particle. ψ_p is the particle domain parameter, which is set to 1 in the particle and 0 in the electrolyte, and smoothly varies between 0 and 1 in the particle-electrolyte interface. For simplicity, we neglect interactions between Li ions in the host structure and consider each phase (surface and bulk) as a thermodynamically ideal solution [113], for which the chemical potential is given by:

$$\mu\,[J/mol] = -F\Omega\psi_s + RT\ln\left(\frac{X}{1-X}\right) \tag{4.4}$$

where μ is the Li chemical potential, F is the Faraday's constant, Ω is the potential difference between the surface and bulk phases, R is the universal gas constant, T is temperature, ψ_s is the surface phase domain parameter (which equals 1 in the surface phase, 0 in the bulk phase, and $0 < \psi_s < 1$ in the interface), and X is the Li site occupancy fraction. Assuming that the crystal structure of the electrode particles remains intact during (de)intercalation, $X = C/\rho$, where ρ is the interstitial site density. The simulations were performed with a constant diffusivity, D, which is related to mobility, M, by:

$$M = D\left(\frac{\partial\mu}{\partial C}\right)^{-1} = \frac{\rho X(1-X)}{RT}D \tag{4.5}$$

We simulate both charging and discharging under galvanostatic conditions. Therefore, a constant current boundary condition determined by the charge/discharge rate (C-rate) is imposed at the particle-electrolyte interface. Moreover, we investigate the regime in which the charge-transfer kinetics are rapid in comparison to mass transport inside the particle and thus the diffusion in the cathode particle limits the overall reaction rate (i.e., the diffusion-limited regime). This is achieved by setting the exchange current density to a sufficiently high value as listed in Table 4.1.

Parameterization and Numerical Scheme

The parameters employed for the simulations in this study are listed in Table 4.1. The parameters are chosen to approximate the properties of layered Li transition metal oxide intercalation compounds. We also assumed identical diffusivity, density, and molar mass of the surface and bulk phases. Moreover, the particle-electrolyte and surface-bulk domain parameters were defined using the following stepwise sine function [118]:

$$\psi = \begin{cases} 0 & \text{if } \left(\frac{\bar{r}-r}{w}\right) < -\frac{\pi}{2} \\ 1 & \text{if } \left(\frac{\bar{r}-r}{w}\right) > \frac{\pi}{2} \\ \frac{1}{2}\left[\sin\left(\frac{\bar{r}-r}{w}\right) + 1\right] & \text{otherwise,} \end{cases} \tag{4.6}$$

where $\bar{r}$ denotes the position of the interface (distance from the center of the particle), and w is a parameter that controls the interfacial thickness of the domain parameter profile. For computational efficiency, the interfacial width for the surface/bulk and particle/electrolyte boundaries is set at 0.5 nm, which is resolved by 5 grid points. Reducing the interfacial width further to define a sharper boundary results in rapidly increasing computation time without improving the accuracy of the simulation results significantly. The values of $\bar{r}$ and w are also listed in Table 4.1, and the corresponding order parameter profiles are shown in Figure 4.3.

For the spatial derivatives, a central finite difference scheme is employed with a $0.1\ nm$ discretization. The temporal evolution of the concentration of Li in the particle is solved with an Euler explicit time stepping scheme. After each time-step, the concentration and chemical potential of Li inside the particle are updated, and the new overpotential is calculated, which is used in the Butler-Volmer equation that sets the reaction flux. In order to implement the constant current boundary condition in the galvanostatic simulations, the boundary value of the electrostatic potential of the cathode particle at the particle-electrolyte interface is adjusted to obtain a new overpotential so that the reaction current from Butler-Volmer equation is equal to the imposed constant current boundary condition.

Table 4.1. The parameters used in the simulations. Reproduced from Ref. [27].

Parameter	Description	Value	Reference
i_0^n	Nominal exchange current density	$8.5 \times 10^{-7}\ A/cm^2$	[119]
α	Transfer coefficient in Butler-Volmer equation	0.5	[120]
D_B	Diffusivity of Li in the bulk phase	$10^{-12}\ cm^2/s$	[121]
D_S	Diffusivity of Li in the surface phase	$10^{-12}\ cm^2/s$	[121]
ρ	Interstitial site density	$0.05\ mol/cm^3$	[122]
Δ	Thickness of the surface phase	$5\ nm$	-
R	Radius of the particle	$50\ nm$	[123]
$\bar{r}_p$	Position of the particle-electrolyte interface	$50\ nm$	-
$\bar{r}_s$	Position of the surface-bulk interface	$45\ nm$	-
w	Interfacial thickness parameter	0.18	[118]

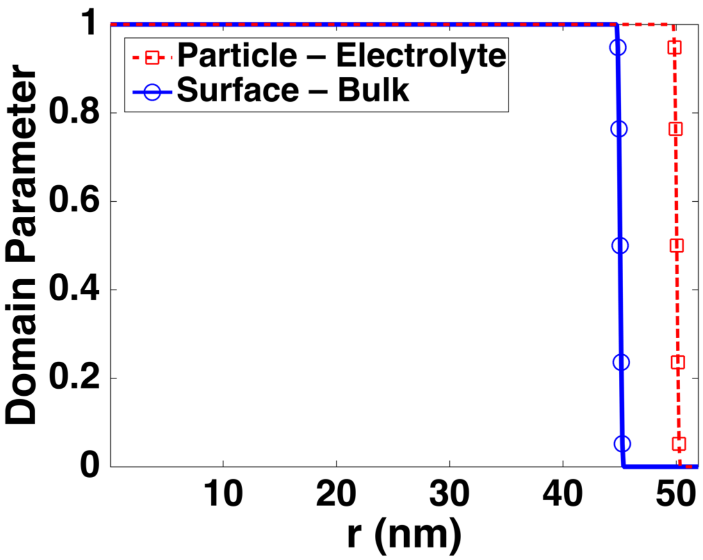

Figure 4.3. Profiles of the particle-electrolyte (Red) and surface-bulk (Blue) domain parameters. The square and circle markers denote the values of the domain parameter in the particle-electrolyte and surface-bulk interfacial regions at the grid points, respectively. Reproduced from Ref. [27].

Results and Discussion

The effect of surface-bulk potential difference

We applied our 1D model to examine the effect of the potential difference, Ω, between surface and bulk on the kinetics of lithium intercalation and the galvanostatic charge/discharge profiles at different values of Ω, C-rates, and exchange current densities. The OCV of the most common cathode materials that are used in hybrid cathode particles such as $LiCoO_2$, $LiMn_2O_4$, $LiFePO_4$, and $LiVPO_4F$ falls within a 0.4 V window [124-127]. Therefore, Ω was varied from -0.2 to 0.2 V. To this end, the simulations were performed at a fixed charge/discharge rate of 1C and a constant exchange current density of $8.5 \times 10^{-7} A/cm^2$. The simulated galvanostatic charge and discharge curves are plotted in Figure 4.4. For $\Omega = 0$, which is equivalent to the case where the entire particle remains in a single phase, the charge and discharge curves are identical in shape as expected, but with a constant polarization of $\sim 0.109\, V$ over the entire cycle. However, the charge/discharge curves increasingly deviate from that of the $\Omega = 0$ case as the magnitude of Ω increases. This deviation is relatively small until $|\Omega| > 0.1\, V$, at which the charge/discharge curves are no longer similar to each other and have a different shape compared to the $\Omega = 0$ case.

At positive and large Ω (Figure 4.4(a)), the discharge curves exhibit two distinct stages, each consisting of rapid decrease followed by slower decrease, which is indicative of a two-stage lithiation process. The first stage is relatively short and corresponds to the surface lithiation step that involves a larger discharge voltage due to the higher surface potential ($\Omega > 0$). Once the lower voltage bulk phase lithiation starts (corresponding to the initiation of the second stage), the discharge voltage drops and the polarization starts increasing with depth of discharge (DOD). Moreover, with increase in Ω the abrupt polarization rise due to the sudden voltage drop at the end of the discharge process occurs earlier at a lower DOD. This results in a reduction in the discharge capacity of the cathode particle, which is more significant when Ω exceeds 0.1 V. For instance, at $\Omega = 0.1$ V, the particle still has more than 97% of its initial discharge capacity. However, by increasing Ω to 0.15 and 0.2 V the discharge capacity of the particle decreases to

86% and 55% of its initial discharge capacity, respectively. On the other hand, the charge curve is less affected by positive Ω values. The only notable changes with increasing Ω are (i) the charge curve becomes almost flat for most of the charge process, and (ii) a voltage increase towards the end of charge due to the delithiation of the surface phase that has a higher open circuit voltage.

The opposite behavior is observed when Ω is negative (Figure 4.4(b)), where the charge curve shows a significant change with Ω. In this case the charge capacity is significantly reduced when the magnitude of Ω exceeds 0.1 V. For instance, at $\Omega = -0.1$ V, the particle maintains more than 97% of its initial charge capacity. However, at $\Omega = -0.15$ V and -0.2 V, the particle has only 86% and 55% of its initial charge capacity, respectively. On the other hand, the discharge curve is less affected by negative Ω values. The only significant changes with increase in the magnitude of Ω are (i) the discharge curve becomes almost flat for most of the discharge process, and (ii) a voltage drop towards the end of discharge due to the lithiation of the surface phase that has a lower open circuit voltage. Overall, the charge/discharge capacity drops with increasing magnitude of Ω in core-shell cathode particles.

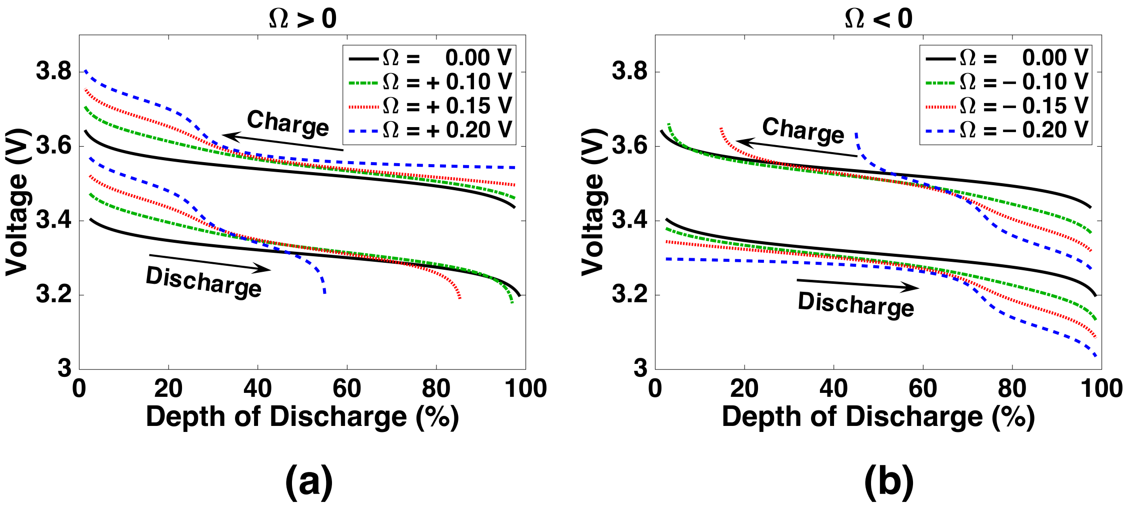

Figure 4.4. Galvanostatic charge and discharge curves at 1C for particles with Ω ranging from a) 0 to 0.2 V and b) from -0.2 to 0 V. As the magnitude of Ω increases, the charge/discharge curves increasingly deviate from the Ω = 0 case. Reproduced from Ref. [27].

The Li concentration evolution inside a cathode particle as a function of depth of discharge at 1C rate are shown in Figure 4.5 for $\Omega = 0, -0.2$ and $+0.2\ V$. For the $\Omega = 0$ case, which is equivalent to a single-phase particle, both surface and bulk regions of the particle are lithiated (delithiated) at the same time during discharge (charge) (Figure 4.5(a)). Therefore, at any time during charge/discharge, the concentration of Li inside the surface and bulk are equal to each other, which results in charge/discharge profiles that are identical in shape with a constant polarization over the entire cycle.

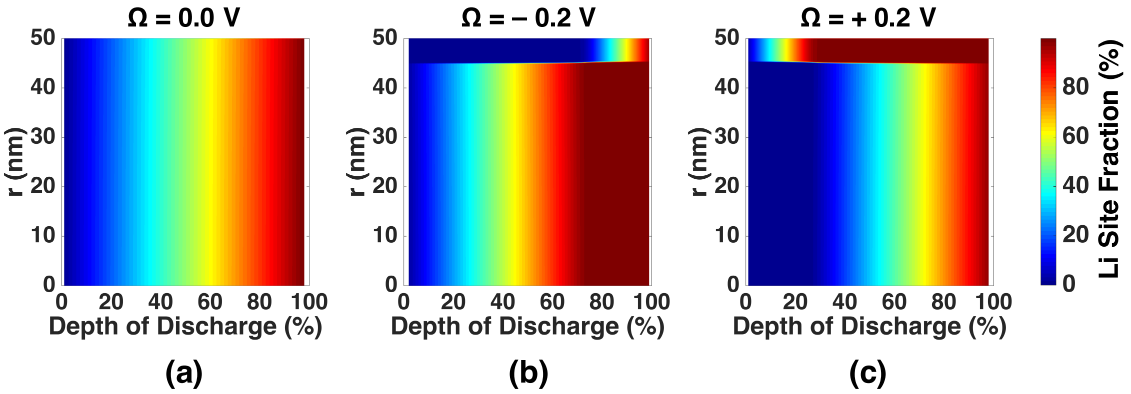

Figure 4.5. The Li concentration evolution inside a cathode particle as a function of depth of discharge at 1C rate for a particle with a) $\Omega = 0$, b) $\Omega = -0.2$ V, c) $\Omega = +0.2$ V. The colorbar indicates the Li site fraction. The lithiation (discharge) proceeds from left to right and the delithiation (charge) proceeds from right to left. Reproduced from Ref. [27].

In the $\Omega = -0.2\ V$ case, where the open circuit voltage of the surface phase is $0.2\ V$ lower than that of the bulk phase, the bulk is lithiated before the surface phase during discharge (Figure 4.5(b)), resulting in a relatively flat discharge curve. The surface phase lithiation then occurs towards the end of the discharge cycle, leading to full lithiation. However, during charge, the surface phase is almost fully delithiated before the lithium in the bulk phase can be accessed. This results in an abrupt increase in the polarization at DOD of ~44% (as seen by the blue dashed curve in Figure 4.4(b)). The Li concentration is very small at the surface, resulting in a low Li mobility in the surface phase. Therefore, the remaining lithium in the bulk phase is trapped inside the cathode particle, ending the charge process.

In contrast, in the $\Omega = +0.2\ V$ case, where the average voltage of the surface phase is $0.2\ V$ higher than that of the bulk phase, the surface phase is lithiated before the bulk phase during discharge (Figure 4.5(c)), resulting in accumulation of Li in the surface phase. As Li builds up in the surface phase, the Li chemical potential in the surface phase increases. Once the Li chemical potential in the surface phase is higher than that of the bulk phase, the lithiation of the bulk phase starts. When the surface phase is almost fully lithiated, the Li site fraction at the particle-electrolyte interface becomes very close to 1.0, rapidly increasing the Li chemical potential at the interface. However, the Li transport inside the particle becomes limited due to the low mobility of Li at high concentrations, which in turn does not allow for further lithiation of the particle. This causes an abrupt increase in the polarization towards the end of discharge, thus reducing the discharge capacity of the cathode particle. It should be noted that the chosen diffusion coefficient ($10^{-12} cm^2/s$) was high enough such that there is no concentration gradient in the surface phase. Choosing a smaller diffusion coefficient will result in a concentration gradient in the surface phase with the Li concentration being higher at the particle-electrolyte interface during discharge, and therefore, further reduces the discharge capacity. The effect of surface and bulk diffusion coefficients will be examined in more details in our future studies.

The effect of charge/discharge rate

The effect of charge/discharge rate on the galvanostatic voltage profiles was studied at four values of Ω, $\pm 0.1\ V$ and $\pm 0.2\ V$, and varying the charge/discharge rate from C/8 to 4C. The results presented in Figure 4.6 (a) show that the charge curve is relatively flat at large Ω ($\Omega = 0.2\ V$), but is shifted towards higher voltages as the C-rate increases. On the other hand, the discharge curves are not as flat and are shifted towards lower voltages as the C-rate increases. Therefore, the charge and discharge curves become further from each other, resulting in larger polarization over the charge-discharge cycle. Moreover, the discharge capacity is reduced at higher C-rates. For instance, by increasing the discharge rate from C/8 to 4C, the discharge capacity reduces from 88% to 37%.

For a smaller Ω ($\Omega = 0.1\ V$), the larger polarization at higher C-rates is also observed, but the reduction in discharge capacity at higher C-rates is far less significant, as shown in Figure 4.6(b). For example, by increasing the discharge rate from C/8 to 4C, the discharge capacity reduces from 99% to 91%. Therefore, the effects of charge/discharge rate on the galvanostatic voltage profiles are more significant at larger magnitudes of Ω.

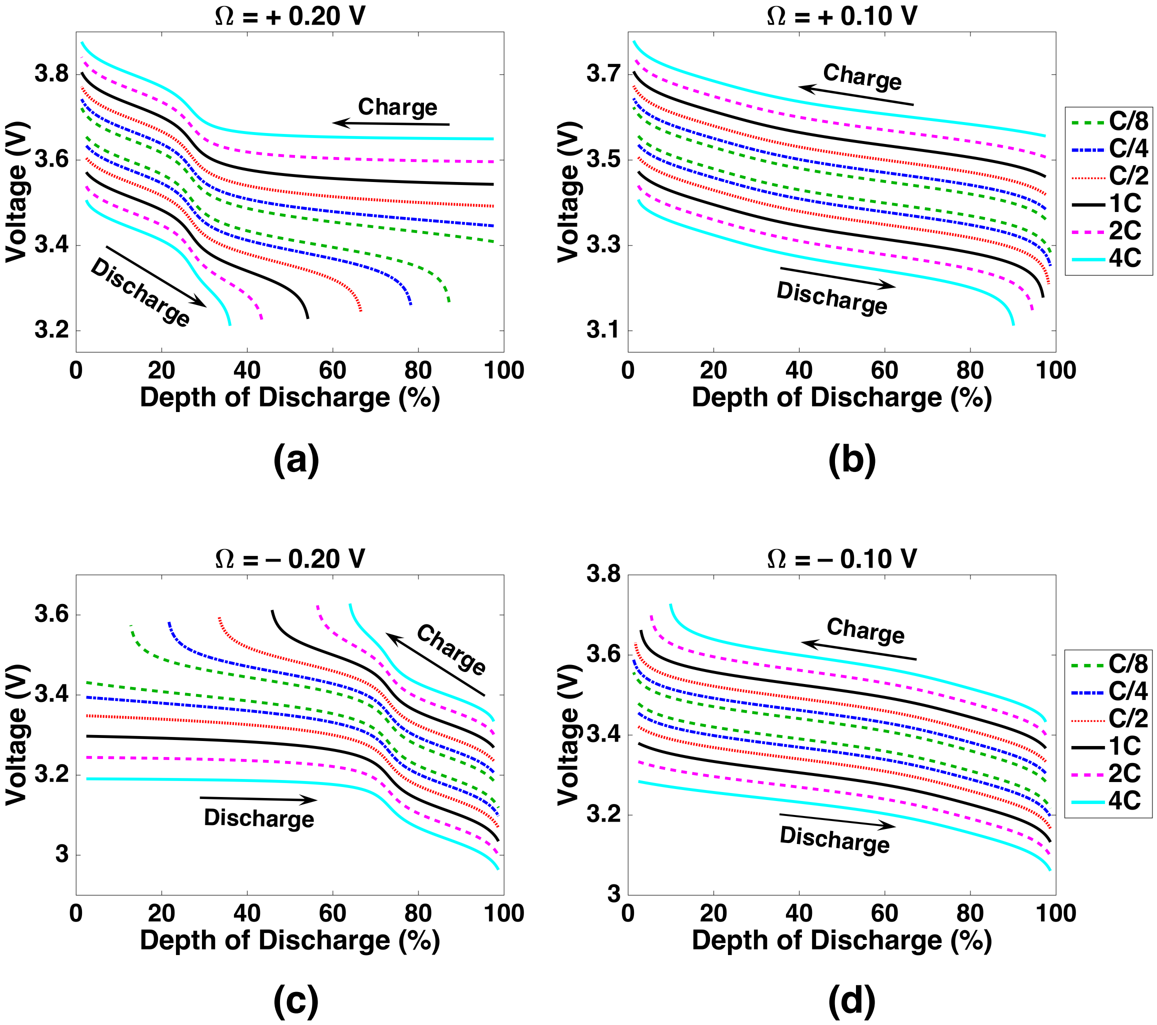

Figure 4.6. Galvanostatic charge and discharge curves at different C-rates for a particle with a) $\Omega = +0.2$ V, b) $\Omega = +0.1$ V, c) $\Omega = -0.2$ V, and d) $\Omega = -0.1$ V. The effects of charge/discharge rate on the galvanostatic voltage profiles are more significant at larger magnitudes of Ω. Reproduced from Ref. [27].

The effect of exchange current density

The exchange current density at the cathode/electrolyte interface depends on the electrolyte system and the active material, which affects the reaction kinetics (e.g., rate constants for the forward and backward electron-transfer reaction). In order to investigate the effect of exchange current density, i_0, on the galvanostatic voltage profiles, the simulations were performed at a fixed C-rate (1C) with $\Omega = \pm 0.1\ V$ and $\pm 0.2\ V$. The exchange current density was varied from $i_0^n/4$ to $4i_0^n$, with $i_0^n = 8.5 \times 10^{-7}\ A/cm^2$ as given in Table 4.1. The results presented in Figure 4.7 show that regardless of the magnitude of Ω, varying the exchange current density within this range does not affect the shape of the voltage profiles. Rather, increasing the exchange current density simply shifts the discharge curves to higher voltages and the charge curves to lower voltages. The reason the shape of the curve remains unchanged is that the parameters were selected such that the charge-transfer kinetics are rapid in comparison to mass transport inside the particle. However, the curves do shift since the larger exchange current density leads to smaller overpotential required to induce the imposed current under the galvanostatic condition.

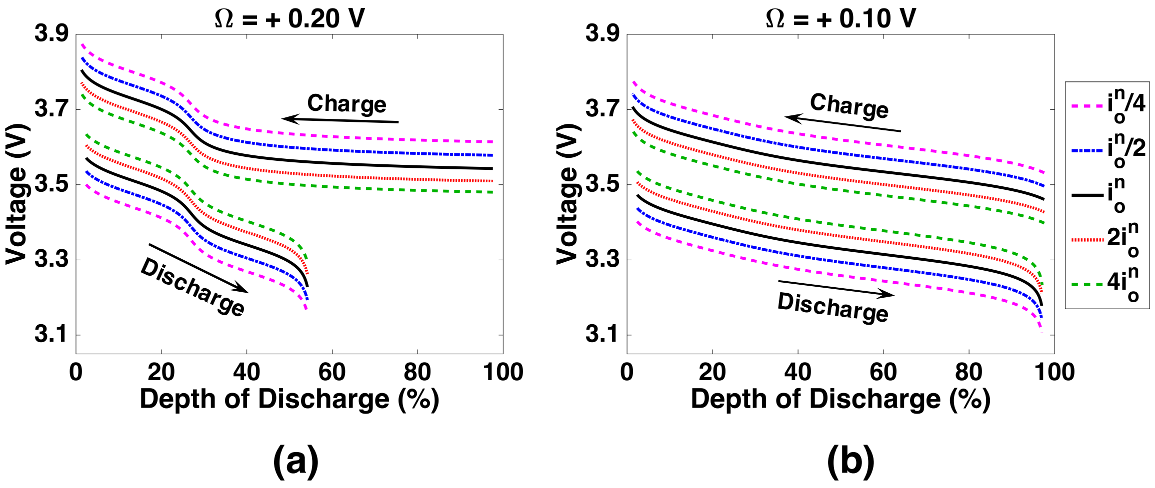

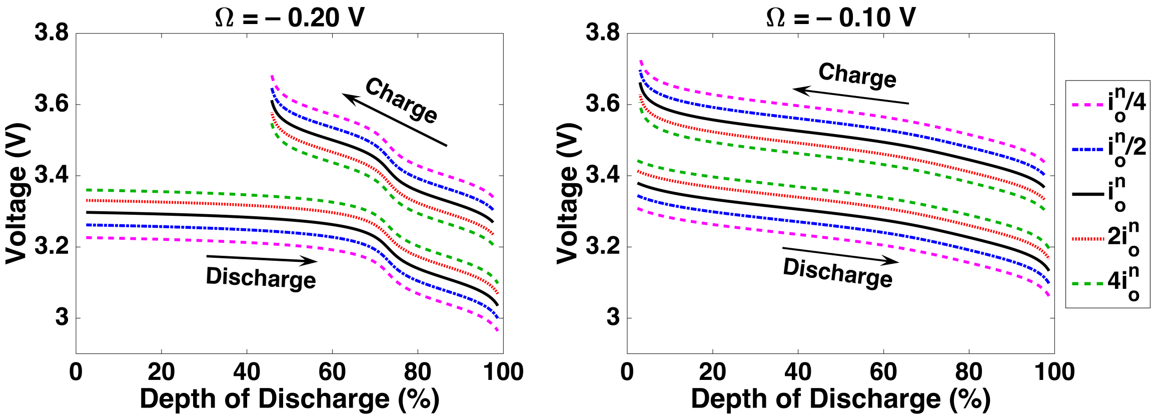

(c) **(d)**

Figure 4.7. Galvanostatic charge and discharge curves at different exchange current densities for a particle with a) Ω = +0.2 V, b) Ω = +0.1 V, c) Ω = –0.2 V, and d) Ω = –0.1 V. The shape of the charge/discharge curves are not affected by the exchange current density, but the polarization is smaller at higher exchange current densities. Reproduced from Ref. [27].

We also performed preliminary simulations for the lithiation/delithiation of core-shell cathode particles using the available literature data for the open-circuit voltage [119] and Li diffusion coefficient [128, 129] inside the particle as a function of lithium content (x in Li_xCoO_2). We utilized an expression in the form of Eq. (S1) to evaluate the chemical potential, μ, as a function of Li site fraction, X:

$$\mu[J/mol] = -F\Omega\psi_s + p_1 \log\left(\frac{X}{1-X}\right) + p_2(X-1)^2 + p_3X^2 + p_4 \tag{4.7}$$

where $p_1 = 5.7795 \times 10^3$, $p_2 = -1.4077 \times 10^5$, $p_3 = -4.5348 \times 10^4$, and $p_4 = -3.5246 \times 10^5$ are constants used to fit the experimental data obtained from OCV measurements in reference [119].

The results shown in Figure 4.8(a) indicate that the discharge capacity decreases as the magnitude of Ω increases, which is consistent with the results obtained from the simulations based on the ideal-solution model presented in the main text. Moreover, galvanostatic simulations at different charge/discharge rates shown in Figure 4.8(b) indicate that the discharge capacity reduces with increasing C-rates, and the reduction in capacity is more significant at larger magnitudes of Ω. This behavior is also consistent with the observed behavior in the simulations based on the ideal solution model.

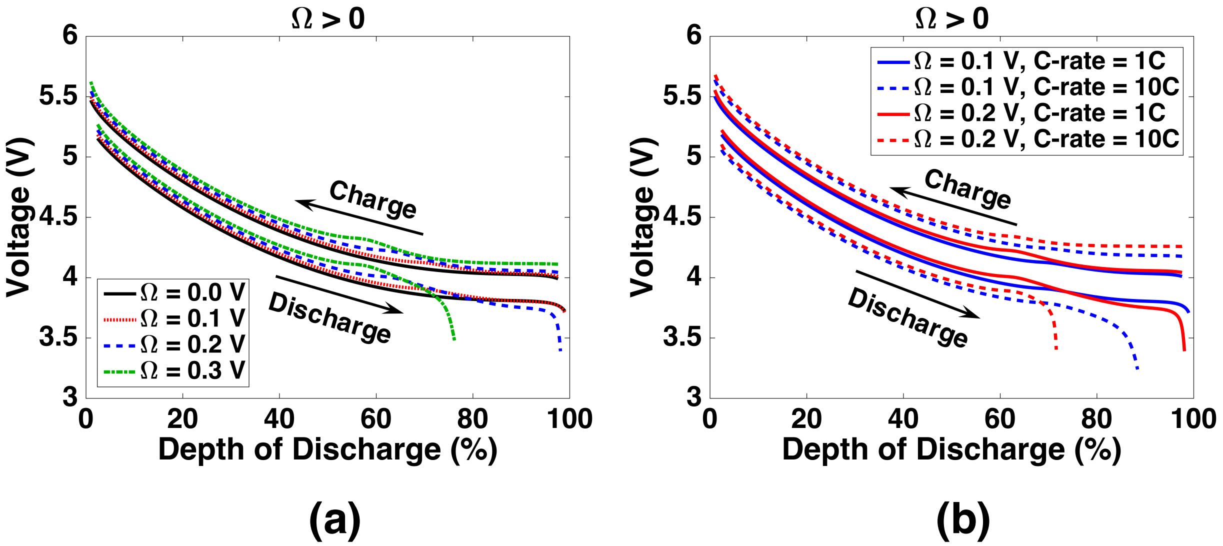

Figure 4.8. Galvanostatic charge/discharge voltage profiles for a core-shell cathode particle using the experimental data for the open-circuit voltage and concentration-dependent Li diffusivity inside the particle. a) The charge/discharge curves at 1C for Ω ranging from 0 to 0.3 V. b) The charge/discharge curves at two different C-rates, 1C and 10C, for Ω = 0.1 V and 0.2 V. Reproduced from Ref. [27].

Our simulations indicated that a core-shell arrangement of two active materials with different OCVs within a single particle does not allow (dis)charging both phases simultaneously, resulting in galvanostatic charge and discharge curves that have different shapes. In a case where the surface and bulk phases have different OCVs, during the charge process, the phase that is comprised of the low-voltage material will be delithiated before the phase comprised of the higher-voltage material. Similarly, during discharge, the higher-voltage material will be lithiated before the lower-voltage material. For example, consider the case where a lower-voltage surface phase surrounds the bulk (Ω < 0). During the discharge process (lithiation), the higher-voltage bulk phase is lithiated before the surface phase. However, during the charge process (delithiation), the lower-voltage surface phase is delithiated before the bulk phase. Therefore, asymmetry between the charge and discharge processes naturally arises with the core-shell heterostructure as a result of geometrical asymmetry coupled to transport limitations caused by low Li mobility. The reduced Li mobility occurs in the phase with higher Li concentration during lithiation when $\Omega > 0$, and the phase with lower Li concentration during delithiation when $\Omega < 0$. This asymmetry results in charge/discharge overpotential and capacity loss, which limit the efficiency of the battery.

We showed that the presence of a second phase with a higher open circuit voltage on the outer portion of the cathode particles reduces the discharge capacity due to the high concentration of Li at the particle-electrolyte interface, which reduces the Li mobility at this interface (see Figure 4.4). This reduction in capacity is more significant at higher discharge rates and in particles with larger potential difference between the bulk and surface phases (see Figure 4.6). These findings can also explain the kinetic behavior of core-shell Li-excess cathode materials. In addition to the inherently poor Li diffusivity in the surface phase of core-shell Li-excess cathode particles described by Lee et al. [109], the inhibited Li diffusion may also be a consequence of accumulation of Li at the particle-electrolyte interface due to the difference in the OCVs of the surface and bulk phases. This finding is also important when designing hybrid cathode particles that are made of two or more active materials in a core-shell geometry. Although coating the cathode particles with another active material can be beneficial [112], a small difference in the OCVs of the two materials in the surface and bulk phases can cause a significant reduction in charge/discharge capacity.

In order to show that the observed behavior of core-shell cathode particles is not an artifact of the ideal-solution assumption, we also performed preliminary simulations for the lithiation/delithiation of core-shell cathode particles using experimental data for the Li diffusivity and the Li chemical potential. We employed the concentration-dependent Li diffusion coefficient in $LiCoO_2$ [128, 129] and the open-circuit voltage of $LiCoO_2$ electrode against metallic lithium [119] to evaluate the Li chemical potential and Li mobility as a function of Li site fraction. The simulation results, which are shown in Figure 4.8, are consistent with the results obtained from galvanostatic simulations under ideal-solution assumption.

As discussed by Grew et al., there is a length scale limit below which atomistic treatment is required to fully describe the physical and chemical behavior of materials [130]. However, simulating the dynamics of nanoparticles during electrochemical processes using an atomistic model is computationally expensive, if not prohibitive. Thus, continuum-scale modeling at nanoscale continues to provide insights and mechanistic understanding of materials as well as their dynamic behaviors. Continuum-scale modeling have been extensively used to study nanoscale phenomena in a wide range of applications such as mechanical properties of nanoparticles [131], nanoscale nucleation and growth [132], transport of nanoparticles [132], and electrochemical modeling and simulation of nanoparticles [116, 117, 133, 134]. In some cases, it has been explicitly shown that continuum-scale modeling can be used to study the mechanical behavior of nanoscale materials if the size of the nanoparticles are at least 10 times greater than the average distance between the neighboring atomic planes [135]. In the case of $LiCoO_2$, the interplanar spacing is less than 15 Å [136], which indicates that a continuum-scale modeling may be applied to nanoparticles that are larger than 15 nm in radius when examining mechanical processes. While such a limit is problem dependent, the qualitative results are unlikely to be affected by the continuum approximation, and our general conclusion would not change. Instead, the nanoscale effect will set the input parameters such as the diffusivity, OCV, and the interfacial kinetic parameters, which are all variable parameters in this work.

While the 1D model presented here captures the dynamic behavior of lithiation/-delithiation processes in core-shell heterostructure cathode particles, it does have some limitations. The 1D model does not capture the effect of the particle geometry, and the current formulation in spherical coordinates is only valid for spherical particles. Moreover, the proposed model does not address the effects of ohmic polarization on the charge/discharge voltage and the Li transport inside the particle. However, the voltage drop across a cathode nanoparticle is in the order of microvolts for a particle of radius $50\,nm$, even when assuming a relatively low electrical conductivity of $10^{-4}\ S/cm$, at a current density of $1\ mA/cm^2$ [8]. Therefore, the effect of ohmic polarization on the voltage is negligible in particle-level simulations. Additionally, in the current model the diffusion coefficient for Li was assumed to be equal in the surface and bulk phases and was not a function of state of charge. However, in reality, the diffusion coefficient of Li in the surface and bulk phases can be different due to the difference in the chemical composition and the crystal structure. The effect of difference in the diffusion coefficients of the surface and bulk phases will be examined in the next chapter.

Summary and Conclusions

In this chapter, the galvanostatic charge/discharge of a cathode particle with core-shell heterostructure was simulated using a one-dimensional continuum-scale model. The model particle is comprised of a core material encapsulated by a thin layer of a second phase with an open circuit voltage that is shifted in value by a constant amount. The Li ion transport in the cathode particles was described by the smoothed boundary method (SBM) formulation of the diffusion equation with the reaction rate as a boundary condition at the particle-electrolyte interface to account for the electrochemical insertion.

The effect of the potential difference, Ω, between the surface and bulk phases on the kinetics of lithium intercalation and the galvanostatic charge/discharge profiles was studied at different values of Ω, C-rates, and exchange current densities. Galvanostatic simulations at a fixed C-rate show that the potential difference between the surface and bulk phases of the cathode particle results in a concentration difference between these two phases. This causes a reduction in the charge/discharge capacity of the particle, which is more significant at higher magnitudes of Ω.

Furthermore, galvanostatic simulations at different charge/discharge rates showed that at higher C-rates the charge and discharge voltage profiles become further from each other, resulting in a larger polarization over the entire charge/discharge cycle. Moreover, the capacity decreases with increase in the charge/discharge rate for a given Ω, and the effects of C-rate on the galvanostatic voltage profiles are more significant at larger magnitudes of Ω. In addition, simulations performed at different exchange current densities showed that regardless of the magnitude of Ω, varying the exchange current density does not affect the shape of the voltage profiles. However, as expected, increasing the exchange current density shifts the discharge curves to higher voltages and the charge curves to lower voltages, resulting in smaller polarization at higher exchange current densities.

The proposed model provides detailed insight into the kinetics and voltage behavior of the lithiation/delithiation processes in core-shell heterostructure cathode particles, which can help improve the electrical performance of cathode materials.

Chapter 5.

The Effect of Diffusivity and Particle Geometry on the Kinetics of Intercalation in Core-Shell Active Cathode Particles

Introduction

In this chapter,* the one-dimensional continuum-scale model developed in Chapter 4 is employed to study the effect of diffusivity and surface-phase thickness on the galvanostatic charge/discharge behavior of cathode particles with a core-shell heterostructure. Rechargeable batteries are considered as one of the primary energy storage solutions for a wide range of applications from vehicle electrification to powering portable electronic devices such as laptops and cell phones [1, 2]. Optimal design and selection of materials for various components of the battery is important for improving the electrochemical performance of rechargeable batteries. Designing new cathode materials with enhanced electrochemical properties, low cost, and improved cycle life is crucial in the development of rechargeable batteries [94].

Previous research has indicated that the electrochemical performance of the cathode materials such as their capacity retention, rate capability, and electrochemical/thermal stability can be tuned by modifying the surface of the active cathode particles [95, 96]. Therefore, designing new hybrid cathode materials by nanoscale coating on active cathode particles has become a common approach in lithium-ion battery research for improving the electrochemical

---

*Derived from the manuscript currently in preparation: S. Kazemiabnavi, R. Malik, B. Orvananos, A. Abdellahi, K. Greenman, G. Ceder, and K. Thornton, “The Effect of Diffusivity and Particle Geometry on the Kinetics of Intercalation in Core-Shell Active Cathode Particles,” *In preparation*.

performance of the cathode [94, 95, 97-99]. For instance, Wang et al. [137] prepared $LiCoO_2$ (LCO) coated by $LiFePO_4$ (LFP) to improve both the thermal stability and electrochemical performance of LCO. By comparing the charge-discharge curves of LCO and LFP-coated LCO at 1C between 2.5 and 4.2 V, they showed that the discharge capacity of bare LCO cathode reduces from 140 to 88 mAh/g after 50 cycles, while LFP-coated LCO has almost no capacity fade after 50 cycles [137]. Moreover, the capacity fade of LFP-coated LCO after 250 cycles at 60°C is only 8.5%, compared to more than 95% for bare LCO [137]. The small capacity fade of LFP-coated LCO at 60°C indicates that the LFP coating does not lose its protective effect at this temperature and therefore improves the thermal stability of the cathode particles [137].

In addition to the aforementioned example, many other dual-active-material cathode particles have been introduced that combines the desirable electrochemical properties of two active cathode materials resulting in a high-performance hybrid cathode material [112]. For example, since coating olivine compounds with conductive carbon is difficult with the exception of $LiFePO_4$ (LFP) [112], Zaghib et al. [105] coated $LiMnPO_4$ cathode particles with LFP to take advantage of the catalytic reaction of Fe with C and facilitate carbon coating of the particles. Other examples of hybrid cathode materials are core-shell $Li_3V_2(PO_4)_3$-$LiVOPO_4$ [138], $LiCoO_2$-coated $LiMn_2O_4$ [139], and coating $LiMn_2O_4$ cathode with nanostructured $LiFePO_4$ layer [140].

The surface phase on active cathode particles may also result from "in-situ" phase formation due to compositional changes during charge/discharge. For example, Kikkawa et al. [108] have observed that overcharging LCO particles results in the formation of $CoO_{2-\delta}$ $(0.67 < \delta < 1)$ on the surface of the particles, which is due to the progression of Co^{3+}/Co^{2+} reduction with oxygen extraction from the surface to the bulk. Another example of in-situ phase formation is the surface phase that forms on the outer portion of $Li_{1.2}Ni_{1/3}Ti_{1/3}Mo_{2/15}O_2$ (LNTMO20) Li-excess cathode particles [109]. Lee at al. [109] have recently proposed a first-charge mechanism for LNTMO20, which includes $Ni^{2+}/Ni^{\sim 3+}$ oxidation, oxygen loss, and oxygen oxidation stages. They showed that the release of oxygen, which mostly occurs near the surface of LNTMO20, is accompanied by the diffusion of under-coordinated transition metal ions into the crystal structure, resulting in an increased transition metal content in the surface phase.

Understanding the electrochemical behavior of dual-active-material core-shell cathode particles is crucial in the development of next-generation high-capacity cathode materials [111]. The kinetics of intercalation in core-shell cathode particles is affected by the diffusivity in the surface and bulk phases as well as the difference in the open-circuit voltages (OCV) of the surface and bulk phases. In an effort to examine the electrochemical behavior of such materials, we have previously developed a continuum-scale model to simulate the galvanostatic charge/discharge of dual-active-material core-shell cathode particles. In chapter 4, we have addressed the effect of OCV shift in the surface phase on the kinetic behavior of core-shell cathode particles [27]. In this chapter, we employ our previously developed continuum-scale model to examine the effect of surface and bulk diffusion coefficients on the lithium intercalation kinetics of a particle with a core-shell heterostructure. These simulations will allow us to analyze the galvanostatic charge/discharge behavior and the Li concentration evolution inside the cathode particles at different rates to determine a material design and selection criteria that ensures optimal electrochemical performance in core-shell hybrid cathode particles.

Results and Discussion

The effect of surface phase diffusivity

In order to investigate the effect of the surface phase that have smaller diffusivity than that of the bulk phase on the kinetics of lithium (de)intercalation, we employed our 1D model to simulate the galvanostatic charge/discharge processes in a single particle. For these simulations, the charge/discharge rate was fixed at 1C and a constant exchange current density of $8.5 \times 10^{-7} A/cm^2$ was used. We also set the OCV difference between surface and bulk phases to 0 ($\Omega = 0$). The Li diffusion coefficient in the bulk phase, D_B, was fixed at $10^{-12} cm^2/s$, while the diffusion coefficient in the surface phase, D_s, was varied from D_b to $D_b/1000$. The $D_s = D_b$ case is equivalent to a single-phase particle.

Figure 5.1(a) shows the simulated galvanostatic charge and discharge curves for particles with different surface-phase diffusivities. Since in all these cases Ω is set to 0, both surface and bulk phases are lithiated (or delithiated) simultaneously, leading to single-stage discharge (or charge) curves for all cases. However, as the surface-phase diffusivity decreases, the charge/discharge curves increasingly deviate from that of the single-phase particle, resulting in a larger voltage hysteresis. As shown in Figure 5.1(b), the charge/discharge capacity decreases with decrease in the surface-phase diffusion coefficient. This reduction in capacity is not significant (less than 5%) until the surface-phase diffusivity is less than $10^{-14} cm^2/s$.

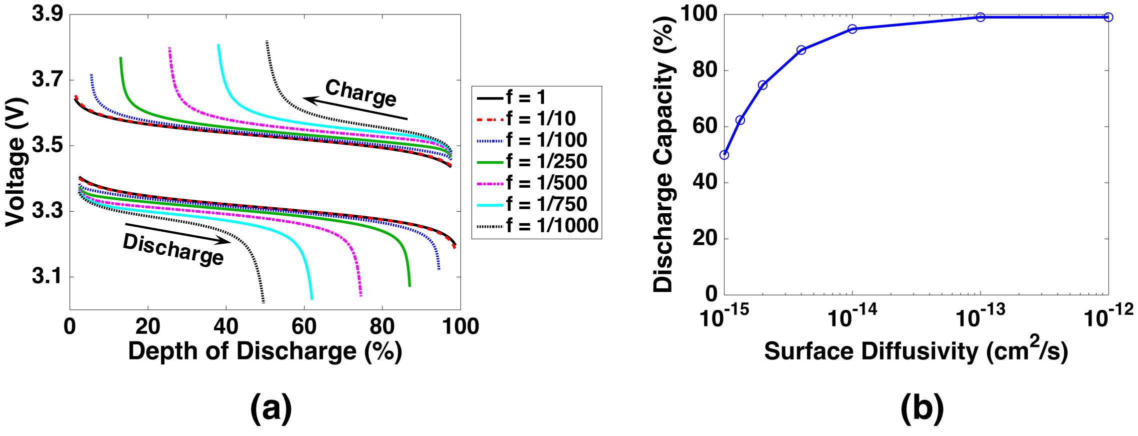

Figure 5.1. a) Galvanostatic charge and discharge curves at 1C for particles with surface-phase diffusivity, D_s, ranging from $D_s = D_b$ to $D_s = D_b/1000$. b) Charge/discharge capacity as a function of surface-phase diffusivity. As the surface phase diffusivity decreases, the charge/discharge curves increasingly deviate from that of the single-phase particle ($D_s = D_b$), resulting in larger voltage hysteresis and reduction in the charge/discharge capacity.

The Li concentration evolution within a cathode particle as a function of depth of discharge at 1C rate are shown in Figure 5.2 for $D_s = D_b$, $D_b/100$, and $D_b/500$. For the $D_s = D_b$ case, the surface and bulk phases have the same Li diffusivity, which is high enough such that the concentration of Li inside the surface and bulk phases are equal to each other at any time during charge/discharge and Li is uniformly distributed inside the particle. However, in the $D_s = D_b/100$ and $D_b/500$ cases, the concentration of Li does not remain uniform inside the particle even though both surface and bulk phases can still be lithiated or delithiated simultaneously because of the equal OCV. Since in the $D_s < D_b$ cases the diffusion coefficient of Li is lower in the surface phase, a concentration gradient forms in the surface phase during lithiation (discharge), resulting in a high concentration of Li at the particle-electrolyte interface. Once the Li site fraction at the particle-electrolyte interface is close to 1.0, the Li chemical potential rapidly increases at this interface. However, the Li transport inside the particle becomes impaired due to the low Li mobility in high concentrations, which in turn does not allow for further lithiation of the particle. This causes an abrupt decrease in the voltage towards the end of discharge, thus reducing the discharge capacity of the cathode particle.

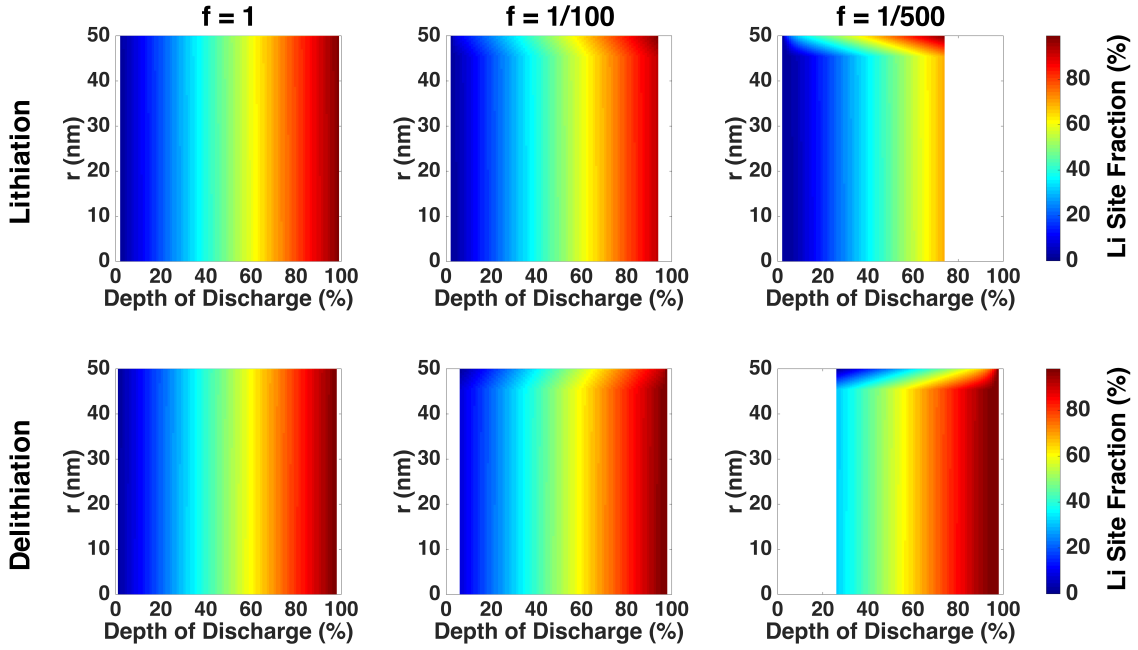

(a) (b) (c)

Figure 5.2. The Li concentration evolution within a cathode particle as a function of depth of discharge at 1C rate for particles with a) $D_s = D_b$, b) $D_s = D_b/100$, and c) $D_s = D_b/500$. The color indicates the Li site fraction. The plots for the lithiation (discharge) processes are shown in the upper row, and the plots for the delithiation (charge) processes are shown in the lower row.

In the $D_s < D_b$ cases (Figure 5.2(b) and 5.2(c)), a concentration gradient forms in the surface phase during charge (delithiation) as well, resulting in a low Li concentration at the particle-electrolyte interface. According to Eq. (4.5), once the Li site fraction at the particle-electrolyte interface is close to 0, the Li chemical potential rapidly decreases at this interface. However, the Li transport becomes limited due to the low Li mobility in low concentrations (see Eq. (4.4)), which in turn does not allow for further lithiation of the particle. This results in an abrupt increase in the voltage, thus ending the charge process. Moreover, by comparing the plots in columns (b) and (c) of Figure 5.2, it is evident that for both lithiation and delithiation processes, the lower the Li diffusion coefficient in the surface phase is, the higher the concentration gradient in the surface phase will be, resulting in a further reduction in the charge/discharge capacity of the cathode particle.

The effect of charge/discharge rate

The effect of charge/discharge rate on the galvanostatic voltage profiles was studied at two values of surface-phase diffusivity, $D_s = D_b/100$ and $D_s = D_b/500$, and varying the charge/discharge rate from C/8 to 4C. The OCV difference between surface and bulk phases (Ω) was still set to 0 in order to isolate its effects on the galvanostatic voltage profiles. The results presented in Figure 5.3 show that in both $D_s = D_b/100$ and $D_s = D_b/500$ cases, as the C-rate increases, the charge curves are shifted towards higher voltages and the discharge curves are shifted towards lower voltages. Therefore, the charge and discharge curves become further from each other at higher C-rates, resulting in a larger voltage hysteresis during the charge-discharge cycle. Moreover, the charge/discharge capacity is reduced at higher C-rates, and this reduction in capacity is more significant for particles with smaller surface-phase diffusivities. For instance, by increasing the discharge rate from C/8 to 2C, the discharge capacity reduces from 99% to 87% for $D_s = D_b/100$ case (Figure 5.3(a)), while it reduces from 98% to 42% for the $D_s = D_b/500$ case (Figure 5.3(b)). Therefore, the effect of charge/discharge rate on the galvanostatic voltage profiles is more significant at smaller surface-phase diffusivity.

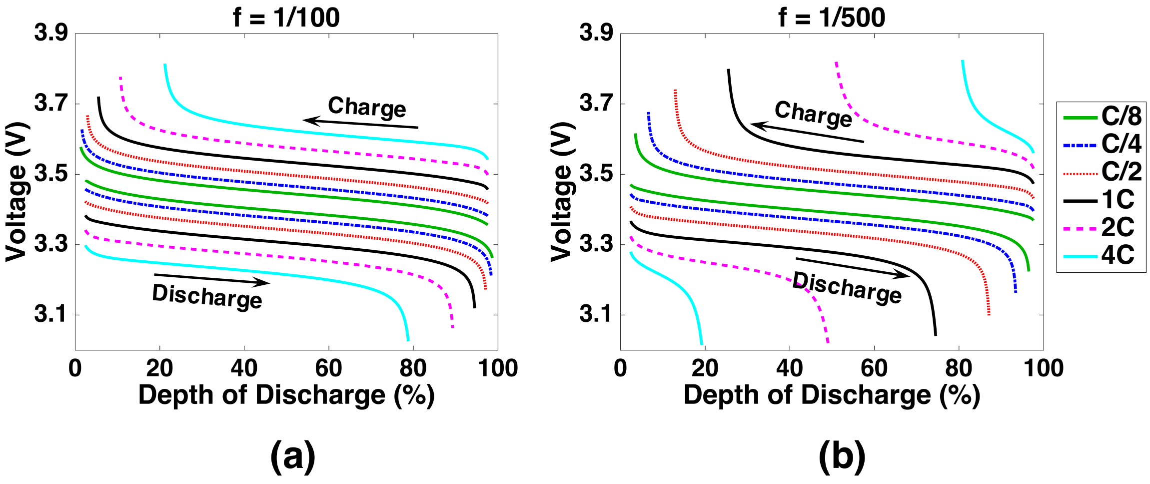

Figure 5.3. Galvanostatic charge and discharge curves at different C-rates for particles with a) $D_s = D_b/100$, and b) $D_s = D_b/500$. The effects of charge/discharge rate on the galvanostatic voltage profiles are more significant in particles with a smaller surface phase diffusivity.

The effect of exchange current density

The exchange current density at the cathode/electrolyte interface determined by the forward and backward reaction rate constants, is affected by the electrolyte system and the active material. In order to investigate the effect of exchange current density, i_0, on the galvanostatic voltage profiles, the simulations were performed at a fixed C-rate (1C) with $D_s = D_b/100$ and $D_s = D_b/500$, while Ω was still set to 0. The exchange current density was then varied from $i_0^n/4$ to $4i_0^n$, with $i_0^n = 8.5 \times 10^{-7}\ A/cm^2$. The results presented in Figure 5.4 show that regardless of the surface-phase diffusivity, the shapes of the voltage profiles do not change by varying the exchange current density within this range. However, decreasing the exchange current density does shift the charge curves to higher voltages and the discharge curves to lower voltages. The reason the shape of the curve does not change is that based on the chosen parameters, the charge-transfer kinetics are rapid in comparison to mass transport inside the cathode particle, leading to a diffusion-limited lithiation/delithiation process. However, the voltage profiles do shift since the charge-transfer resistance is higher in particles with a smaller exchange current density, and therefore, a larger overpotential is required to impose the constant-current boundary condition.

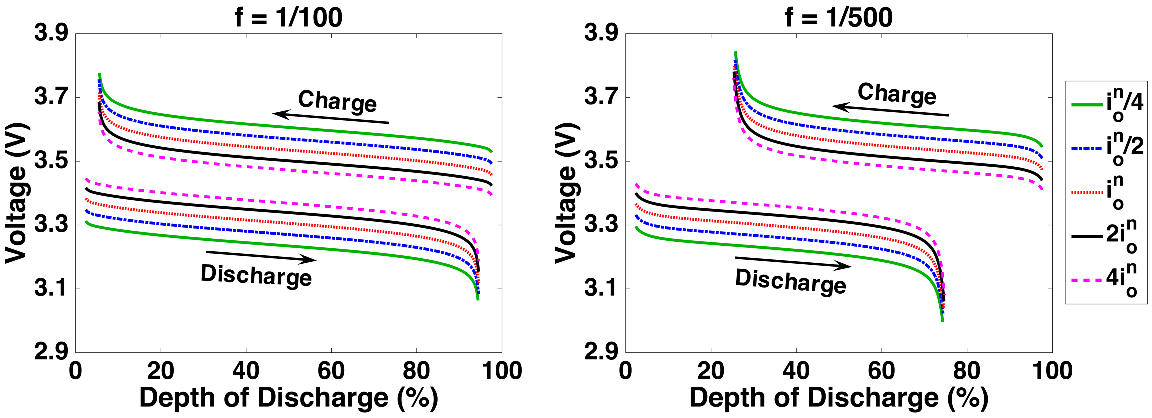

(a) (b)

Figure 5.4. Galvanostatic charge and discharge curves at different exchange current densities for particles with a) $D_s = D_b/100$, and b) $D_s = D_b/500$. While the shapes of the charge/discharge curves do not change by varying the exchange current density, the voltage hysteresis is smaller at higher exchange current densities.

The effect of surface-bulk OCV difference

The effect of surface-phase diffusivity on the galvanostatic voltage profiles of core-shell cathode particles was also studied in cases where the surface and bulk phases have different OCVs. In this scenario, we assumed that the bulk phase with an OCV of V_0 and a Li diffusivity of D_b is encapsulated by a surface phase with a shifted OCV of $V_0 + \Omega$ and a Li diffusivity of D_s. The value of Ω was varied from $0.0\,V$ to $0.2\,V$. The Li diffusion coefficient in the bulk phase was fixed at $10^{-12}\ cm^2/s$, while the Li diffusion coefficient in the surface phase was varied from $D_b/10$ to $10D_b$. The results shown in Figure 5.5 indicate that in all cases, the charge/discharge capacity decreases with increase in the magnitude of Ω. However, the reduction in capacity is smaller when the surface-phase diffusivity is higher than the bulk-phase diffusivity ($D_s = 10D_b$ cases). Therefore, a higher surface-phase diffusivity compensates for the capacity loss caused by the OCV difference between the surface and bulk phases. In chapter 4 we showed that this reduction in capacity is due to transport limitations caused by low Li mobility in the surface phase. By increasing the surface-phase diffusivity, the Li mobility in the surface phase also increases. Therefore, during lithiation (discharge) when $\Omega > 0$, a higher mobility in the surface phase allows for more Li to enter into the bulk phase, resulting in an increased discharge capacity. Moreover, during delithiation (charge) when $\Omega < 0$, a higher mobility in the surface phase allows for more Li to leave the bulk phase, resulting in an increased charge capacity.

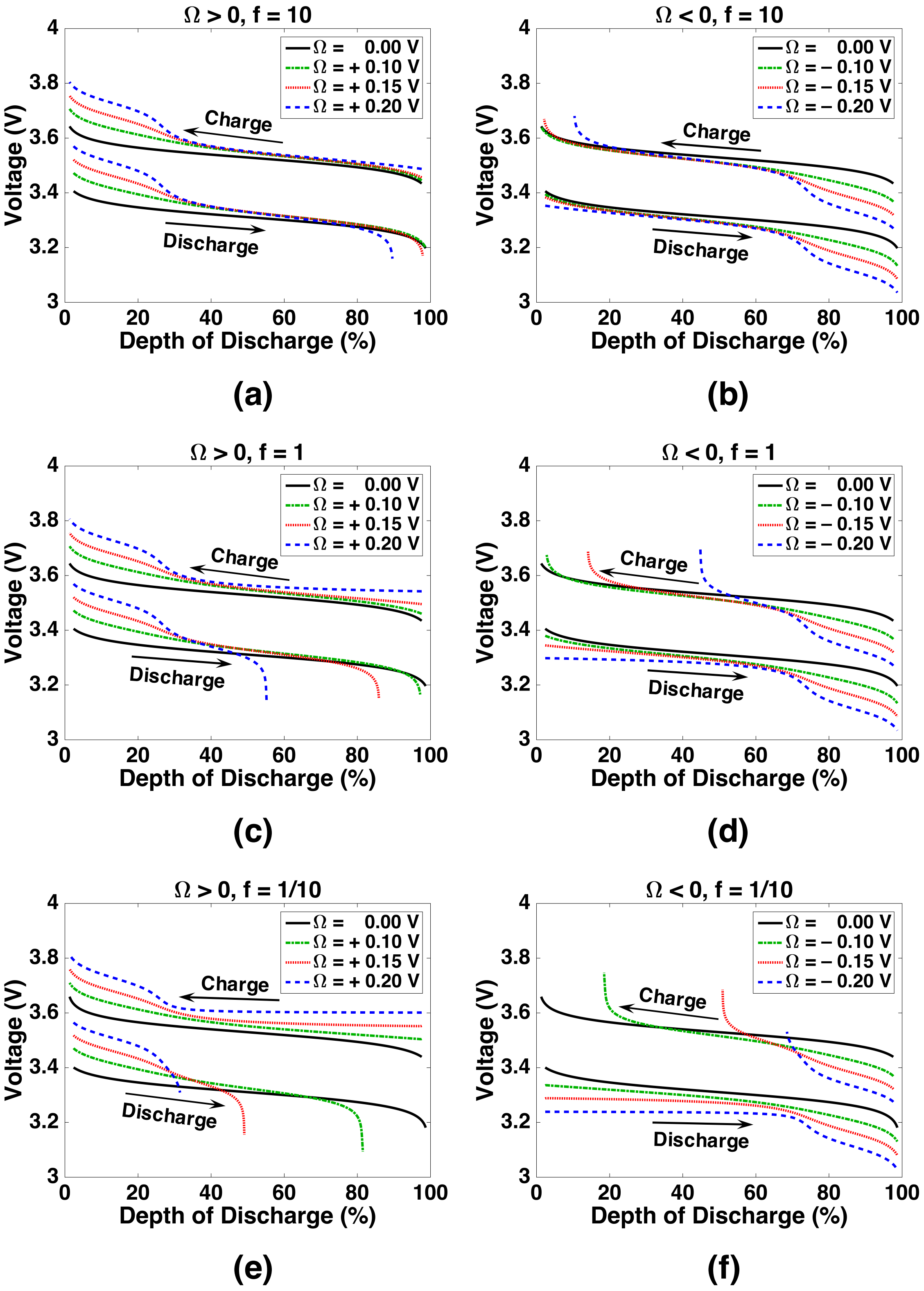

Figure 5.5. Galvanostatic charge and discharge curves at 1C for particles with Ω ranging from –0.2 V to +0.2 V, and a surface-phase diffusivity ranging from $D_b/10$ to $10D_b$. A higher surface phase diffusivity compensates for the capacity loss caused by the OCV difference between the surface and bulk phases.

The effect of surface phase thickness

The effect of surface-phase thickness on the galvanostatic discharge capacity was studied by varying the surface thickness from $\Delta = 5\,nm$ to $45\,nm$, while keeping the radius of the particle constant at $50\,nm$. In all cases, the Li diffusion coefficient in the bulk phase was varied from 1.0×10^{-11} to $5.0 \times 10^{-14}\,cm^2/s$. In the first case, the OCV difference between the surface and bulk phases was set to 0 ($\Omega = 0$), but the Li diffusion coefficient in the surface phase was assumed to be 100 times lower than that of the bulk phase. As shown in Figure 5.6(a), in this case the discharge capacity decreases with increase in the surface thickness. The reason is that the surface phase with a lower Li diffusivity, limits the Li transport into the particle. Therefore, in particles with a thicker surface phase, the Li atoms have to diffuse through a longer path with low Li diffusivity. As a result, the Li concentration at the surface of the particle increases more rapidly, which in turn inhibits further lithiation of the particle and therefore, decreases the accessible discharge capacity of the particle.

In the second case, the OCV difference between the surface and bulk phases was set to 0.2 V ($\Omega = 0.2\,V$), but the Li diffusion coefficient in the surface phase was assumed to be equal to that of the bulk phase. As shown in Figure 5.6(b), in this case the discharge capacity increases with increase in the surface thickness. The reason is that the surface phase with a higher OCV is lithiated before the bulk phase. Once the surface phase is fully lithiated, the remaining capacity in the bulk phase becomes inaccessible. Therefore, in particles with a thicker surface, there is less inaccessible bulk phase, which allows for more Li to diffuse into the particle, resulting in an increased discharge capacity.

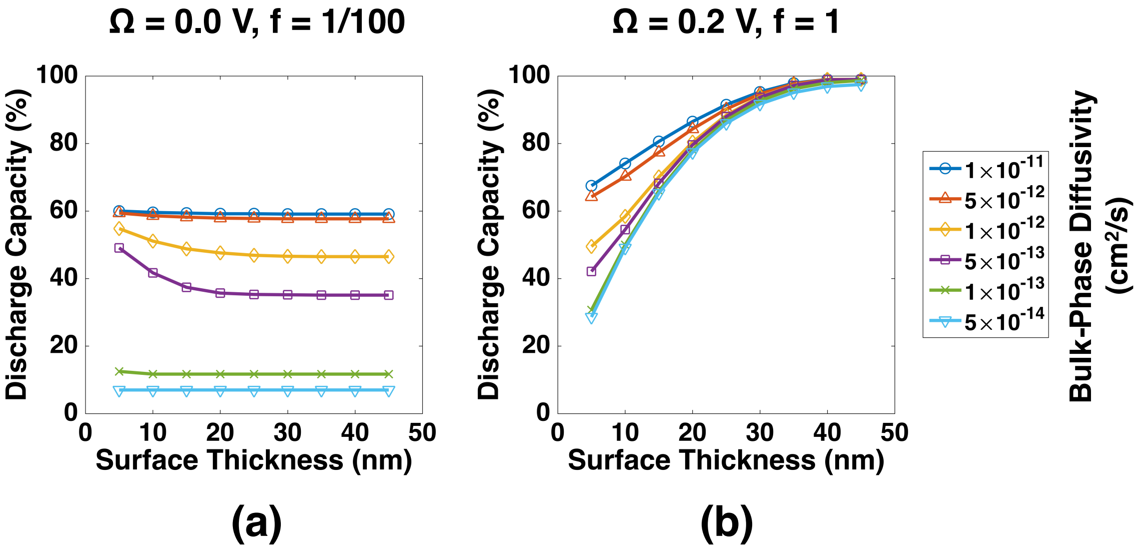

Figure 5.6. Galvanostatic discharge capacity of core-shell cathode particles with a) Ω = 0.0 V and $D_s = D_b/100$, b) Ω = +0.2 V and $D_s = D_b$.

Summary and Conclusions

In this chapter, we utilized our 1D continuum-scale model described in chapter 4 to simulate the galvanostatic charge/discharge of a core-shell cathode particle. The model particle is assumed to be spherical, in which the core material is encapsulated by a thin layer of a second phase with a different OCV and Li diffusivity. The SBM formulation of the diffusion equation was used to describe the Li transport inside the particle, and a reaction rate boundary condition was set at the particle-electrolyte interface to account for the electrochemical insertion of Li described by Butler-Volmer kinetics.

The effect of the surface-phase diffusivity on the Li intercalation kinetics and the galvanostatic charge/discharge behavior of core-shell cathode particles was studied at different C-rates and exchange current densities. Galvanostatic simulations at a constant C-rate show that the galvanostatic charge/discharge capacity of the particle decreases with reduction in the surface-phase diffusivity. By examining the Li concentration evolution inside the particle, we showed that this reduction in capacity is caused by the low Li transport mobility at the surface of the particle due to the high Li concentration in the surface phase during lithiation (discharge) and low Li concentration during delithiation (charge).

In addition, galvanostatic simulations at different C-rates showed that increasing the C-rate results in an increase in the voltage hysteresis during the charge/discharge cycle. Moreover, as the C-rate increases, the charge/discharge capacity decreases, and this reduction in capacity is more significant in particles with a lower surface-phase diffusivity. Additionally, simulations performed at different exchange current densities showed that varying the exchange current density does not affect the shape of the voltage profile; however, the voltage hysteresis is smaller at higher exchange current densities.

The effect of surface phase diffusivity was also studied in particles where the surface and bulk phases have different OCVs. Galvanostatic simulations indicated that the reduction in capacity caused by the surface-bulk OCV difference is smaller when the surface-phase diffusivity is higher than the bulk-phase diffusivity. Therefore, a higher surface-phase diffusivity compensates for the capacity loss caused by the OCV difference between the surface and bulk phases.

The effect of the surface-phase thickness on the galvanostatic discharge capacity of core-shell cathode particles was studied by varying the thickness of the surface phase while keeping the radius of the particle constant. Galvanostatic simulations showed that in particles where the surface and bulk phases have the same OCV but the surface phase has a lower Li diffusivity than the bulk phase, the discharge capacity decreases with increase in surface thickness. However, in particles where the surface phase has a higher OCV than the bulk phase but both phases have the same Li diffusivity, the discharge capacity increases with increase in surface thickness.

Our simulations showed that the galvanostatic charge/discharge capacity of a hybrid cathode particle with a core-shell heterostructure is greatly affected by the OCV of the constituent active materials, Li diffusion coefficient in the surface and bulk phases, and the thickness of the surface phase. By analyzing the voltage profiles and Li concentration evolution inside the particles during the charge/discharge processes, these simulations also shed light on the kinetics of Li intercalation/deintercalation in core-shell hybrid cathode particles. These findings provide valuable guidance in material design and selection when designing high-capacity hybrid cathode materials for rechargeable batteries.

Chapter 6.

Modeling Reaction Heterogeneity in Battery Electrodes using Porous Electrode Theory

Introduction

In this chapter,[*] we present a continuum-scale model based on the porous electrode theory to study the reaction heterogeneity in battery electrodes. While energy storage in lithium ion batteries relies on the ability of a cathode phase to reversibly intercalate Li ions, critical performance metrics such as energy density, rate capability, and cycle life often depend on the heterogeneous composite electrode architecture, which mediates electronic and ionic transport to the cathode particles. Realizing the full performance potential of a given cathode requires that this nanocomposite architecture, which contains the active phase along with conductive carbon additives, binder and electrolyte accessible porous regions, be optimized to effectively transport and deliver the charge carriers (i.e., Li-ions and electrons) to the cathode particles. For a given system, the electrode architecture and cycling parameter, must be optimized to deliver the best balance between capacity, power, and stability. While the cycling parameters (e.g. rate) are controlled for the cell and nanocomposite electrode as a whole, locally, limitations in ionic and electronic conductivity in the composite heterostructure may retard the reaction in parts of the electrode. This heterogeneity in the electrochemical reaction is associated with local deviations

---

[*] Adopted from H. Liu, S. Kazemiabnavi, A. Grenier, G. Vaughan, M. Di Michiel, B.J. Polzin, K. Thornton, K.W. Chapman, and P.J. Chupas, "Quantifying Reaction and Rate Heterogeneity in Battery Electrodes in 3D Through Operando X-Ray Diffraction Computed Tomography," *ACS Appl. Mater. Interfaces*, 11, 20, (**2019**) 18386-18394. This is an unofficial adaptation of an article that appeared in an ACS publication. ACS has not endorsed the content of this adaptation or the context of its use.

from the target cycling parameters and may be detrimental to the battery's performance [141], leading to locally underutilized capacity, non-uniform electrode degradation and accelerated capacity loss. For example, recent studies implicated reaction heterogeneity that arises as a consequence of cracking of secondary particles as the principal origin of long-term capacity fading in $LiNi_{0.8}Co_{0.15}Al_{0.05}O_2$ [142]. Hence, quantifying the degree and length scale of such heterogeneity in the energy storage reaction is important to designing of improved battery electrode architectures.

To interrogate reaction heterogeneity within the composite electrode, the local state-of-charge must be resolved on relevant length and time scales. Because of the dynamic nature of battery cycling, it is imperative that such reaction heterogeneity is quantified in *operando*, during charge and discharge. Spatially-resolved *operando* studies of electrochemical cycling have been demonstrated using a variety of probes sensitive to the reaction chemistry, including nuclear magnetic resonance spectroscopy [143], energy dispersive X-ray diffraction [144, 145], and neutron [146-148] and X-ray imaging [149-154]. Amongst these, computed tomographies (CT) have been widely adopted to resolve the electrode reaction in three dimensions (3D) to reveal how reactions proceed and how heterostructures, such as Li dendrites [149, 155], may develop. Such CT reconstructions are typically a compromise between the field-of-view and spatial resolution, with additional constraints on the time resolution and sample scale dictated by the measurement rate (e.g. flux) and penetration. For example, while X-ray transmission microscopy can follow reactions within particles with very high spatial resolution (e.g. 10s of nm), the field-of-view is restricted (e.g. to small crystallites of active material [151-154] or 10s of micron) and does not extend to the full electrode. Recently, penetrating high energy X-ray-based CT has demonstrated the potential to cover full battery devices to image the distribution of components in a commercial battery [156] and to isolate the scattering signal of an active phase from the cell background during cycling [157].

In this chapter, the simulation results were validated against experimental data obtained from *operando* high energy X-ray diffraction computed tomography (XRD-CT) [158] to resolve and quantify reaction heterogeneity within a whole electrode (Figure 6.1). The high-energy X-rays can penetrate macroscale objects to map a complete composite electrode assembled in a realistic battery stack [156, 157], with the diffraction data directly probing the chemical structure of the active electrode particles. We focus on a thick electrode, relevant to recent strategies to increase the energy density, based on $LiFePO_4$ which has a high rate capability such that any reaction heterogeneity is not specific to the active material but reflects the limitations of the composite architecture. The cycling reaction was mapped with 200 μm in-plane resolution and 100 μm depth resolution (i.e. with distance from the current collector) over the full electrode, to resolve and quantify heterogeneity in the in-plane and depth-dependent dimensions. The in-plane and depth resolution were adjusted to ensure an average change of 0.05 Li per formula unit of $LiFePO_4$ per operando scan step to limit the compositional changes occurred during each scan. This leads to a temporal resolution of ~30 min per scan. While the average state-of-charge across the electrode matches the electrochemistry, locally, there are large variations in state- and rate-of-charge.

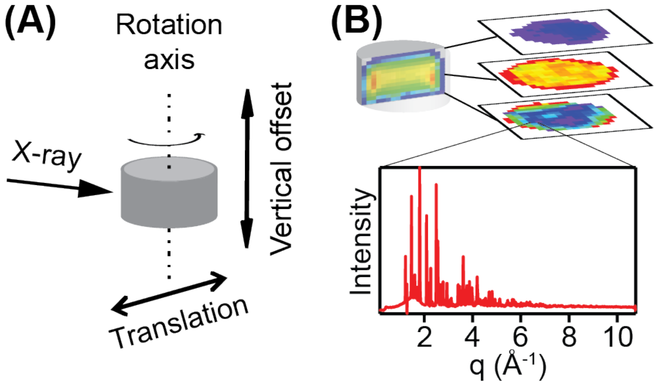

Figure 6.1. Illustration of the X-ray diffraction computed tomography. a) A schematic of the experimental setup for X-ray diffraction computed tomography. b) An example of the reconstructed composite electrode during charge with false color representation of the Li composition of electrode particles. An example of the reconstructed X-ray diffraction pattern from a single voxel is also shown. Reproduced from Ref. [28].

The insights provided by the XRD-CT have implications in the development of batteries with higher energy density, where increasing the electrode thickness is a strategy that reduces the relative proportion of inactive components such as the current collector. However, increasing the electrode thickness extends the transport pathway for charge carriers and impedes high-power applications. Improvements in charge transport in thick electrodes are predicated on the design of better electrode architectures [159, 160]. The combination of XRD-CT and continuum-scale modeling offers a new approach to evaluate novel electrode architectures, therefore, opening new avenues to develop high-energy density composite electrodes.

Mapping the reaction state through XRD-CT

The voltage profile during the *operando* XRD-CT is shown in Figure 6.2(a). The reconstructed X-ray scattering data from a single voxel at the start and end of charge are shown in Figure 6.3. The data were well fit by reported [161] structural models for $LiFePO_4$ (LFP) and $FePO_4$ (FP), refining the lattice parameters and the peak shape. This correspondence confirms the reliability of the reconstructed Bragg peak intensities and the potential for detailed Rietveld structural analysis.

Since the delithiation of LFP proceeds *via* a two-phase reaction, where FP grows at the expense of LFP [162], the state-of-charge and Li composition, can be evaluated based on the relative fraction of each phase. The integrated intensities of the (301) peaks for both phases were used to determine the relative phase fraction of LFP, which is shown in Figure 6.2(a) (square markers) for the whole electrode. Since the relative LFP phase fraction alone is necessary to determine the reaction kinetics, the efficient and robust peak fitting method was chosen to extract the phase fractions. The average LFP phase fraction determined from XRD-CT is in good agreement with the expected linear change of the average Li composition of the electrode under galvanostatic cycling (dashed black line in Figure 6.2(a)). The Li composition map of different horizontal layers across the electrode thickness during cycling is shown in Figure 6.2(b).

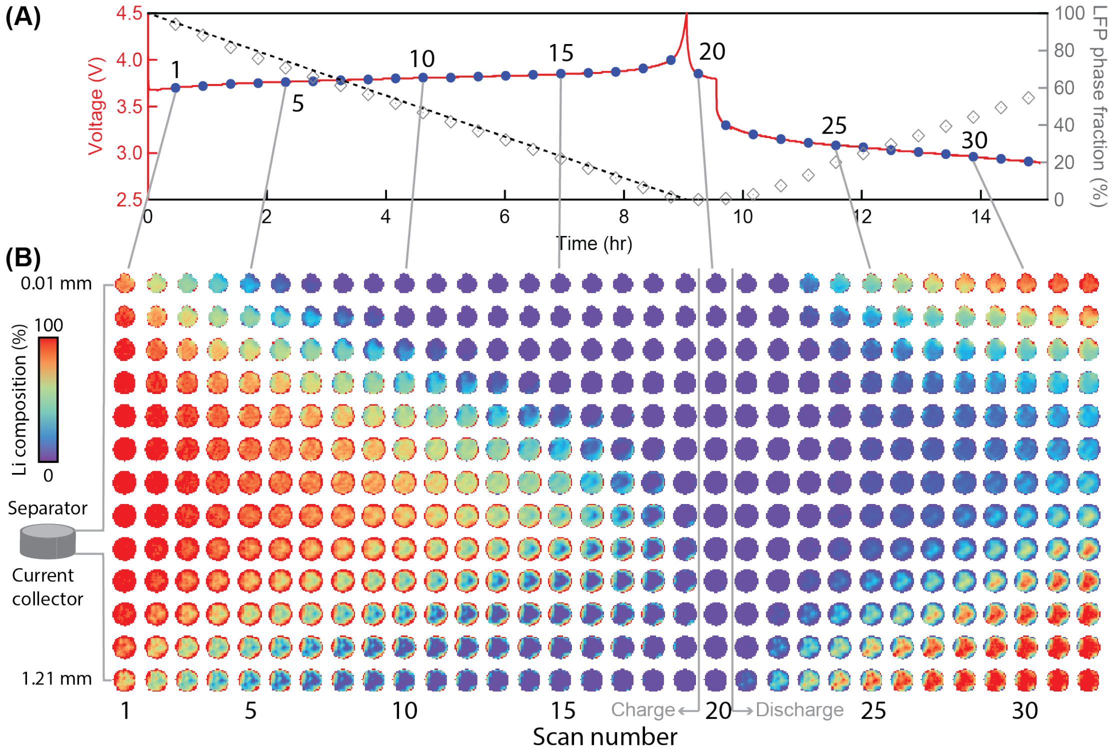

Figure 6.2. a) Voltage profile of the thick electrode cycled at C/10 during operando XRD-CT (red curve). Blue dots indicate the time of each tomography measurement. Grey squares indicate the average LFP phase fraction of the entire electrode. The dashed black line indicates the ideal LFP phase fraction during galvanostatic charge. b) The LFP phase fraction, i.e. the Li composition, map of different horizontal layers across the electrode during cycling. The Li composition (LFP phase fraction) is represented in color. The separation between adjacent layers is 0.1 mm. Reproduced from Ref. [28].

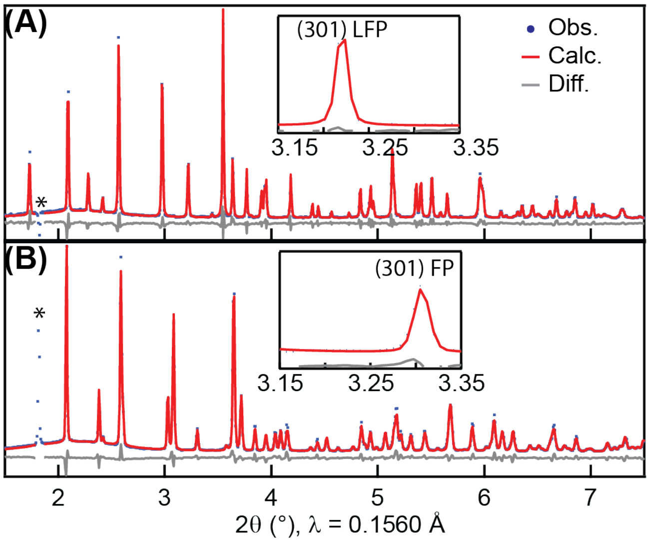

Figure 6.3. Examples of reconstructed X-ray diffraction patterns from voxels of the (a) LFP and (b) FP phase. The asterisk indicates the peak position corresponding to the PTFE tube, which could not be correctly reconstructed due to absorption. Blue dots correspond to the reconstructed pattern, red line the calculated pattern, and grey line the difference between the reconstructed and the calculated. Reproduced from Ref. [28].

Electrochemical Model

The charge (delithiation) of the cell was modeled using the porous electrode theory [163] with representative volumes to account for the particle-size distribution of the many particles that are present throughout the cathode [145, 164, 165]. To predict the charge/discharge behavior of the cell, multiple physical and chemical phenomena have been considered that occur simultaneously in the porous electrode and the liquid electrolyte. Namely, we consider the coupled evolution of (1) concentration and (2) electrostatic potential in the porous electrode, (3) concentration and (4) electrostatic potential in the electrolyte, and (5) the electrochemical reaction in the porous electrode [145]. We assume uniform lithium concentration inside the cathode particles, and therefore, the concentration evolution of the particles is described using a pseudo-capacitor model [145]. The configuration of the simulation domain that represents the experimental cell is shown in Figure 6.4. The cylindrical cathode is 1.2 mm thick with a diameter of 3 mm, and has a porosity of 66%. The remaining 33% is composed of 83.7% LFP, 7.2%

carbon, and 9.1% binder by volume. The separator has a thickness of 160 μm and is 40% porous. The gap between electrode and its casing is approximately 90 μm.

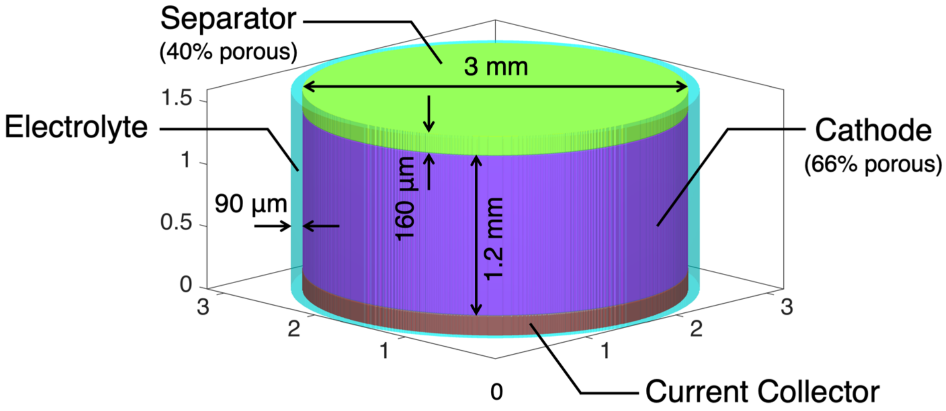

Figure 6.4. The configuration of the LFP electrode with a thickness of 1.2 mm and a porosity of 66% used in the porous electrode simulations. Reproduced from Ref. [28].

In the current formulation of the porous electrode model, representative volumes were used to account for the particle-size distribution of the many particles that are present inside the cathode. Each representative volume in the computational domain is assumed to contain ten spherical particles with different sizes. Simulations performed with 20 and 30 spherical particles in each representative volume resulted in less than 5% difference in the Li composition during charge at C/10. The constituent particles are assumed to follow a log-normal size distribution with an average of 122 nm in particle diameter and a standard deviation of 84 nm.

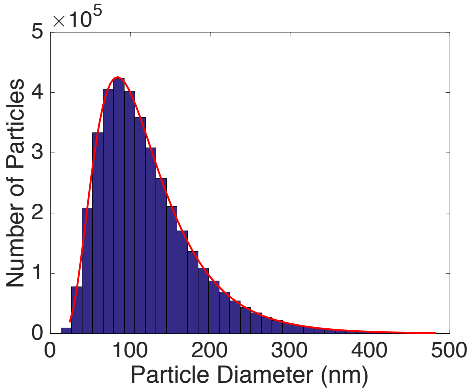

Figure 6.5. The log-normal distribution of particle size used in the simulations. The average and standard deviation of particle diameter are 122 nm and 84 nm, respectively.

The modified governing equations of the porous media were used to account for the presence of multiple particles in each voxel (representative volume) of the computational domain. According to the porous electrode model, the volume fraction of the solid components, ε_s, can be represented as:

$$\varepsilon_s = 1 - \varepsilon_e \tag{6.1}$$

where ε_e is the volume fraction of the electrolyte. The solid phase is assumed to be composed of active materials with a volume fraction of L_p, and inactive materials with a volume fraction of $1 - L_p$.

The salt concentration evolution in the electrolyte is described by the porous-medium diffusion equation with a source term accounting for reaction [134],

$$\varepsilon_e \frac{\partial C_e}{\partial t} = \nabla.(\varepsilon_e D_{amb} \nabla C_e) - (1 - t_+) \sum_i a_{p,i} r_i \tag{6.2}$$

where C_e is the salt concentration, t is time, and r_i is the reaction rate of the particle i. D_{amb} and t_+ are the ambipolar diffusivity and cation transference number, respectively, which are calculated from the ionic diffusivities in the electrolyte using the equations from the textbook by Newman and Thomas-Alyea [8]. The variable $a_{p,i}$ is the surface area per unit volume of the intercalation particles and is defined as $a_{p,i} = \varepsilon_s L_p a_{v,i} (V_i / V_T)$, in which V_T is the sum of the volumes for the ten particles in each representative volume, and $a_{v,i}$ is the particle area per particle volume defined as $a_{v,i} = A_i / V_i$. Here A_i and V_i are the area and volume of particle i, respectively.

The electrostatic potential in the electrolyte, ϕ_e, is obtained by imposing the electroneutrality condition on the continuity equation [134, 163],

$$\nabla.\left[\varepsilon_e \frac{F}{RT} (z_+ D_+ - z_- D_-) C_e \nabla \phi_e\right] = \sum_i a_{p,i} r_i + \nabla.[\varepsilon_e (D_- - D_+) \nabla C_e] \tag{6.3}$$

where F is Faraday's constant, R is the universal gas constant, T is the absolute temperature, z_j and D_j are the charge number and diffusivity of species j, respectively.

We assume uniform concentration inside the cathode particles, and therefore, the concentration evolution of the particles is described using a pseudo-capacitor model [145],

$$\frac{\partial c_{s,i}}{\partial t} = a_{v,i} r_i \tag{6.4}$$

where $C_{s,i}$ is the average concentration in particle i.

The electrostatic potential in the solid phase is determined by employing the current continuity equation in the porous media [145, 163],

$$\nabla . [\varepsilon_s \kappa_s \nabla \phi_s] = -F \sum_i a_{p,i} r_i \tag{6.5}$$

where κ_s and ϕ_s are the effective electrical conductivity and the electrostatic potential of the solid phase, respectively.

The Butler-Volmer equation is assumed to yield the electrochemical reaction rate [145],

$$r_i = \frac{i_0}{F}\left[\exp\left(-\frac{\alpha F}{RT}\eta\right) - \exp\left(\frac{(1-\alpha)F}{RT}\eta\right)\right] \tag{6.6}$$

where i_0 is the exchange current density, α is the transfer coefficient, and η is the overpotential defined as $\phi_s - \phi_e - (V_{OC} - \mu_s/F)$. Here, V_{OC} is the open-circuit voltage plateau and μ_s is the chemical potential defined based on the regular solution model [134, 145],

$$\mu_s = RT\left[\ln\left(\frac{X_s}{1-X_s}\right) + \Omega(1-2X_s)\right] \tag{6.7}$$

where Ω is the regular solution parameter and X_s is the occupied Li site fraction defined as $X_s = C_s/\rho_{Li}$ and ρ_{Li} is the Li-site density. The exchange current density, i_0, in Eq. (6.6) is defined as [163]:

$$i_0 = \frac{F\left(k_c^0 a_e\right)^{1-\alpha}\left(k_a^0 a_s\right)^{\alpha}}{\gamma_{TS}} = \frac{i_0'(a_e)^{1-\alpha}(a_s)^{\alpha}}{\gamma_{TS}} \tag{6.8}$$

where k_a^0 and k_c^0 are the rate constants for the anodic and cathodic reactions, respectively, α is the charge transfer coefficient, and i_0' is the exchange current density coefficient. The term γ_{TS} is the chemical activity coefficient of the transition state, which is approximated as $1/(1-X_s)$ [166]. The activity of the electrolyte, a_e, is defined as C_e/C_e^0, where C_e^0 is the reference concentration at which the exchange current density was measured. The activity of the particle, a_s, is defined as $a_s = \exp(\mu_s/RT)$. The model parameters used in the simulations are listed in Table 6.1. Combining the two rate constants into one parameter (i_0'), is similar to the approach used in Refs. [166-168]. We take i_0' to be $2.97 \times 10^{-6}\ A/cm^2$, which is obtained by scaling an experimental value of $2.97 \times 10^{-4}\ A/cm^2$ measured using electrochemical impedance spectroscopy [169] by 1/100 as suggested by Bai *et al.* [166]. This scaling was done since the macroscopic cross-sectional area was used in the experimental measurements, while in this study the exchange current density should be per the actual particle surface area [134], and assumes that the two areas differ by a factor of 100.

Numerical Scheme

The set of partial differential equations, Eq. (6.2), (6.3), and (6.5), were solved using a central finite difference scheme for the spatial discretization and a backward implicit time-stepping scheme for the temporal discretization in Eq. (6.2). A uniform spatial discretization with a grid spacing of 40 μm was used along all directions. The equation for the salt concentration evolution in the electrolyte, Eq. (6.2), is implicitly solved using the alternating-direction-line-relaxation (ADLR) scheme [114]. The electroneutrality equation in the electrolyte, Eq. (6.3), and the current continuity equation in the solid phase, Eq. (6.5), are also solved using the ADLR scheme. The concentration evolution within the particles, Eq. (6.4), was solved using a forward explicit time-stepping scheme.

Table 6.1. The parameters employed in the simulations and their sources. Reproduced from Ref. [28].

Parameter	Description	Value	Reference
D_+	Diffusivity of cation in the electrolyte	$7.3 \times 10^{-7}\ cm^2/s$	[170]
D_-	Diffusivity of anion in the electrolyte	$4.0 \times 10^{-6}\ cm^2/s$	[170]
κ_s	Electrical conductivity in the solid phase	$0.01\ S/cm$	-
i_0'	Exchange current density coefficient	$2.97 \times 10^{-6}\ A/cm^2$	See text
Ω	Regular solution parameter	4.5	[145]
ρ_{Li}	Li-site density	$0.0228\ mol/cm^3$	[145]
V_{OC}	Open-circuit voltage plateau	$3.42\ V$	[145]
α	Transfer coefficient in Butler-Volmer equation	0.2	[171]
T	Absolute temperature	$300\ K$	-

Results and Discussion

The simulated Li composition for all the horizontal layers across the thickness of the electrode during charge (delithiation) at C/10 is shown in Figure 6.6. The simulation results show that the dominant reaction heterogeneity is observed as a function of depth within the electrode, which is in agreement with the observed reaction heterogeneity between different layers (through plane) in the XRD-CT experiments (Figure 6.2(b)). The reaction occurs faster within electrode layers near the separator and the current collector, compared to the layers at the center of the electrode. For example, delithiation of the layer closest to the separator was completed in ~5 hours, approximately half of the time needed for the entire electrode, with this layer spending the remaining time at rest.

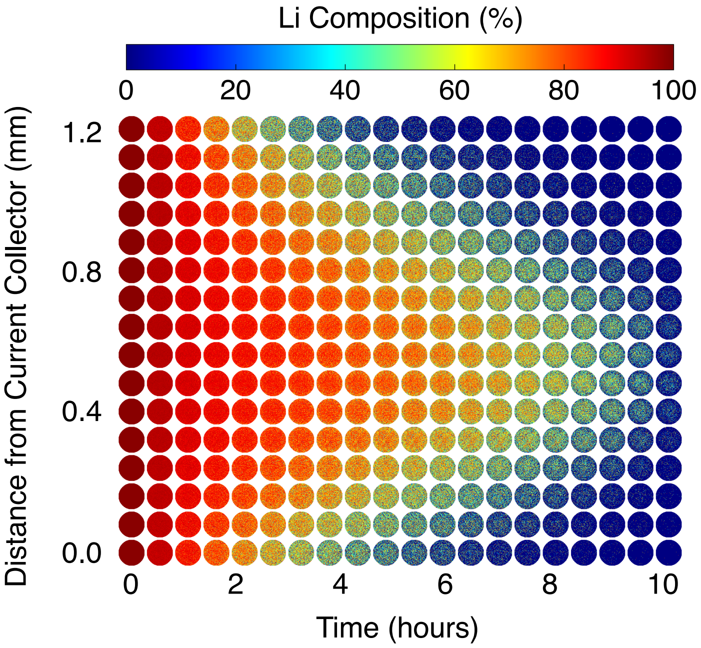

Figure 6.6. The simulated Li composition map of different horizontal layers across the electrode during delithiation (charge) at C/10. The Li composition (LFP phase fraction) is represented in color. The separation between adjacent layers is 0.08 mm.

The high rate capability of LFP [172, 173] means that the observed reaction heterogeneity reflect kinetic limitations of the composite electrode architecture. The reaction heterogeneity arises as the transport of charge carriers, that is, electrons in the solid phase of the composite electrode and ions of the liquid electrolyte within the composite electrode pores, becomes rate-limiting. For conventional composite electrodes, a non-monotonic reaction gradient through the electrode, with a higher rate of reaction for particles close to the current collector and the separator, is expected when both electronic and ionic conductivities/limitations are of similar magnitude and cycled at high current densities [174]. This seems to suggest that electrochemical reaction for the present thick electrode, is also subject to the dual limits of electronic and ionic conductivities.

Simulations were undertaken to verify the rate-limiting mechanisms underlying the observed reaction heterogeneity. A virtual model of the composite electrode shown in Figure 6.4

was used to simulate the charge behavior observed experimentally. To identify the rate-limiting factor that gives rise to the non-monotonic Li concentration through the electrode, simulations with three different electrical conductivities for the composite LFP electrode (κ_s = 0.005, 0.01, and 0.04 S/cm) were performed. While ionic diffusivity in the liquid electrolyte can also impact reaction heterogeneity, for a given electrolyte system, differences in the electrode's tortuosity induce less variability in the effective ionic diffusivity (by a factor of only 2-3 for calendered vs. non-calendered electrodes) [175] than is possible for the electrical conductivity and hence, these simulations focus on the impact of varying electrical conductivity on the reaction distribution in the composite electrode.

The simulated Li concentration evolution within the porous cathode during charge at a rate of C/10 is shown in Figure 6.7. In the case where the electrical conductivity of the composite cathode is high (Figure 6.7(c) with κ_s = 0.04 S/cm), the delithiation near the current collector occurs at a lower rate compared to that near the separator. In the case where the composite cathode has a low electrical conductivity (Figure 6.7(a) with κ_s = 0.005 S/cm, a value reported for carbon-coated LFP [176, 177]), the delithiation near the current collector occurs at a higher rate compared to that near the separator. In the case where the composite cathode has an intermediate electrical conductivity (Figure 6.7(b) with κ_s = 0.01 S/cm), the delithiation of the electrode occurs near both current collector and separator at similar rates and is in good agreement with the experimental observation (Figure 6.7(d)).

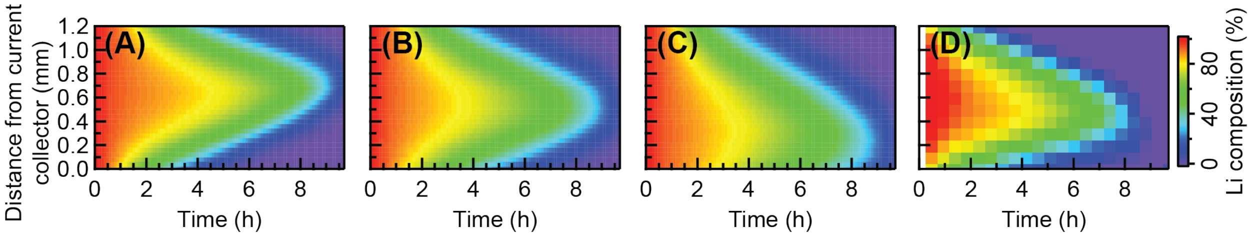

Figure 6.7. The simulated and observed Li concentration evolution inside the porous cathode. The simulated Li concentration evolution with an electrical conductivity of (a) 0.005 S/cm, (b) 0.01 S/cm, and (c) 0.04 S/cm during charge at a rate of C/10 as well as (d) the observed Li concentration evolution. Reproduced from Ref. [28].

Moreover, as shown in Figure 6.8, this result is independent of the potential for ions from the electrolyte to enter the electrode disc from the edges or current collector face, due to gaps between the electrode and cell casing or between the electrode and current collector, as may exist in the present experiment geometry.

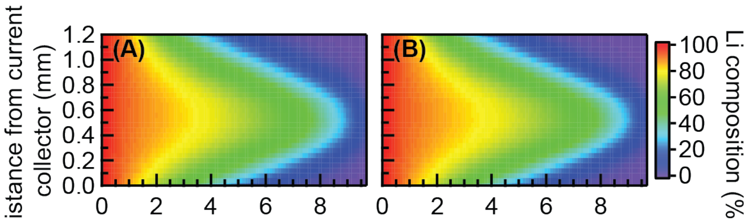

Figure 6.8. The simulated Li concentration evolution inside the porous cathode during charge at a rate of C/10. In (a) there is a gap between the composite electrode and its casing, and the current collector is porous. In (b) there is no gap between the cell and its casing, and the current collector is not porous. The effective electrical conductivity of the composite cathode is 0.01 S/cm for both cases. Reproduced from Ref. [28].

Our simulation demonstrates the mixed control of the reaction kinetics by both the electrical and ionic conductivity. The driving force for reaction is effectively dictated by the overpotential as the electrostatic potential difference between the solid phase, i.e. the composite porous electrode, and the liquid electrolyte. (Eq. 6.6) For a high electrical conductivity, this overpotential is dominated by the electrostatic potential of the electrolyte, which increases with increasing distance from the current collector and favors a more rapid reaction at the separator end. For a low electrical conductivity, this overpotential is dominated by the electrostatic potential of the composite porous electrode, which decreases with increasing distance from the separator and favors a more rapid reaction at the current collector end. For an intermediate electrical conductivity, this overpotential is at a minimum magnitude in between the two ends of the electrode and increases in magnitude with closer proximity to either end of the electrode. Therefore, faster reactions observed for regions close to both ends of the electrode in the present study is evident of larger magnitude of overpotential at both the current collector and the separator ends, which are dictated by the relative electrical and ionic conductivities.

Summary and Conclusions

Limitations in rate capability are recognized for most active electrode materials; cycling an electrode at higher rates leads to reduced effective capacity, increased strain and/or fracture [178], and accelerated capacity fade and failure. Reaction heterogeneity evident within the electrode leads to a distribution in rate, above and below the average applied to the whole cell. It is possible that the extremes in rate experienced by parts of the electrode may play a larger role in governing rate-limiting phenomena (e.g. strain, fracture, capacity fade). The peak rather than the average reaction rate may offer a better quantitative comparison to local studies or models of degradation. Improving the reaction uniformity may mitigate these effects, to allow increased lifetime for the same average rate (i.e. a lower maximal rate) or to allow an increased average rate capability for same maximal local rate. It may be possible to design electrode architectures incorporating microstructural heterogeneity, such as depth-dependent porosity and particle size [179], that mitigate transport limitations that give rise to the depth-dependent heterogeneity evident here, such that the reaction and rate are more uniform.

Chapter 7.

Modeling Highly-Ordered Hierarchical Anodes for Extreme Fast Charging Batteries

Introduction

In this chapter,[*] we present a three-dimensional continuum-scale model based on the porous electrode theory to investigate the electrochemical performance of highly-ordered hierarchical anode architectures during extreme fast charging conditions. As one of the primary energy storage solutions, Li-ion batteries play a major role in a wide range of applications from vehicle electrification to powering consumer electronic devices. The state-of-the-art Li-ion battery utilizes porous electrodes comprised of solid-state active material particles and the pores are filled with a Li-ion conducting electrolyte. The operation of a Li-ion battery is contingent upon Li-ion transport through these electrolyte-filled pores. Therefore, the microscopic structure of the composite electrodes affects the rate at which these ions are transported [180]. Decreasing the porosity of the electrodes by maximizing the volume fraction of active material increases the energy density of a battery. However, decreasing the porosity of the electrode generally increases its tortuosity [181], which in turn slows down the ion transport in the electrode, and therefore, decreases the rate capability of the battery. Thus, developing electrodes with enhanced ionic

---

[*] Derived from the manuscript currently in preparation: S. Kazemiabnavi, S. M. Mortuza, K-H Chen, M. Namkoong, C. Yang, J. Mazumder, J. Sakamoto, N. Dasgupta, and K. Thornton, "Modeling Highly-Ordered Hierarchical Anodes for Extreme Fast Charging Batteries," *in preparation.*

transport is essential for improving the electrochemical performance of Li-ion batteries under extreme fast charging conditions.

In industrial manufacturing of Li-ion battery electrodes, a slurry that consists of active electrode particles, conductive additive, and polymeric binder is cast and dried on a current collector followed by a series of calendaring processes to control the thickness and porosity of the electrode [182]. The microstructure of the battery electrodes depends heavily on the morphology of the active electrode particles used as well as the processing conditions under which the electrodes are made [183-185]. For example, Marks et al. have shown that non-spherical platelet-shaped active material particles demonstrate anisotropic tortuosity due to the alignment of the particles parallel to the current collector during the manufacturing process, which results in an increased tortuosity in the cross-plane direction (i.e., perpendicular to the current collector) [182].

Recently, novel electrode fabrication techniques have been developed to allow for fast charge and discharge with minimal capacity loss by enhancing Li transport kinetics inside the battery electrode. For example, Zhang et al., have reported cycling rates of up to 400C and 1000C for Li-ion and nickel-metal hydride batteries, respectively, by using cathodes made from a three-dimensional bicontinuous nanoarchitecture [186]. Bae et al., introduced battery electrodes with ordered dual-scale porosity that combines aligned channels and a porous matrix to minimize the electrode tortuosity. These electrodes that are fabricated using iterative co-extrusion and sintering, reportedly result in a three-fold improvement in capacity per unit are when compared with optimized conventional Li-ion battery electrodes [187]. However, both abovementioned fabrication techniques are far from commercialization. In this chapter, we show that introducing vertical channels through the thickness of the electrode is effective in suppressing the Li ion transport limitations that occur during fast charging. We use a three-dimensional model based on the porous electrode theory to investigate the geometric parameters that affect the electrochemical performance of highly-ordered hierarchical (HOH) anodes under galvanostatic extreme fast charging conditions.

Electrochemical Model

The configuration of the computational domain used to model the electrochemical behavior of the HOH anode is shown in Figure 7.1. The model Li-ion battery consists of the cathode, the separator, the anode, and the electrolyte, which fills the porous components as well as the channels in the anode.

The lithium concentration evolution in the active electrode particles is described by the Fick's second law of diffusion in spherical coordinates [36],

$$\frac{\partial c_{s,i}}{\partial t} = D_{s,i} \frac{1}{r^2} \frac{\partial}{\partial r} \left(r^2 \frac{\partial c_{s,i}}{\partial r} \right) \tag{7.1}$$

where i denotes the positive ($i = p$) or negative ($i = n$) electrodes. A no-flux boundary condition is applied to the center of the particle such that $-D_{s,i} \frac{\partial c_{s,i}}{\partial r} = 0$ at $r = 0$. Since the electrochemical reaction occurs at the particle-electrolyte interface, the flux on the surface of the particles is equal to the reaction rate such that $-D_{s,i} \frac{\partial c_{s,i}}{\partial r} = J_i$ at $r = R_{s,i}$, where J_i is the electrochemical reaction flux at the surface of the particles [36].

The salt concentration evolution for the binary electrolyte in the liquid phase is described by the porous-medium diffusion equation with an electrochemical reaction source term [36],

$$\varepsilon_i \frac{\partial c_i}{\partial t} = \nabla . \left(D_{eff,i} \nabla \mathrm{c}_i \right) + (1 - t_+^0) a_i J_i \tag{7.2}$$

where $i = p$, s, and n, denoting positive electrode, separator, and negative electrode, respectively. The variable a_i is the surface area per unit volume of the intercalation particles defined as $(3/R_{s,i})(1-\varepsilon_i-\varepsilon_{f,i})$. The reaction flux is zero in the separator since it is not electrochemically active. No-flux boundary conditions are applied to the electrode-current collector interfaces at the two ends of the cell such that $-D_{eff,n}\nabla c_n\big|_{z=0}=0$ and $-D_{eff,p}\nabla c_p\big|_{z=L_n+L_s+L_p}=0$ [36]. At the positive electrode-separator and the negative electrode-separator interfaces, we assume continuous electrolyte salt concentration and continuous flux, resulting in the following additional boundary conditions [36],

$c_n|_{z=L_n^-}=c_s|_{z=L_n^+}$,

$c_s|_{z=(L_n+L_s)^-}=c_p\big|_{z=(L_n+L_s)^+}$,

$-D_{eff,n}\nabla c_n\big|_{z=L_n^-}=-D_{eff,s}\nabla c_s\big|_{z=L_n^+}$, and

$-D_{eff,s}\nabla c_s\big|_{z=(L_n+L_s)^-}=-D_{eff,p}\nabla c_p\big|_{z=(L_n+L_s)^+}$.

The electrostatic potential in the solid phase is determined by employing Ohm's law [36],

$$\nabla.\left[\sigma_{eff,i}\nabla\phi_{s,i}\right]=a_iFJ_i \qquad (7.3)$$

where σ_{eff} is the effective electrical conductivity of the electrode defined as $\sigma_{eff,i}=\sigma_i(1-\varepsilon_i-\varepsilon_{f,i})$ with $i=p$ and n for positive and negative electrode, respectively. A flux boundary condition is applied to the positive electrode-current collector interface such that the charge flux is equal to the applied current density [36],

$-\sigma_{eff,p}\nabla\phi_{s,p}\big|_{z=L_n+L_s+L_p}=I_{app}$.

A no charge flux boundary condition is applied to the electrode-separator interfaces, which results in the following boundary conditions [36],

$-\sigma_{eff,p}\nabla\phi_{s,p}\big|_{z=L_n+L_s}=0$, and

$-\sigma_{eff,n}\nabla\phi_{s,n}\big|_{z=L_n}=0$.

The electrostatic potential at the negative electrode-current collector interface is set to zero, $\phi_{s,n}\big|_{z=0} = 0$, and therefore, the cell voltage will be equal to the electrostatic potential at the positive electrode-separator interface, $E_{cell} = \phi_{s,p}\big|_{z=L_n+L_s+L_p}$ [36].

The electrostatic potential in the liquid phase is governed by the charge balance equation based on Ohm's law [36],

$$-\nabla\left[\kappa_{eff,i}\nabla\phi_{l,i}\right] + \frac{2RT\left(1-t_+^0\right)}{F}\nabla\left[\kappa_{eff,i}\nabla \ln c_i\right] = a_i F J_i \tag{7.4}$$

No charge flux boundary conditions are applied to the liquid phase at the electrode-current collector interfaces such that [36],

$-\kappa_{eff,n}\nabla\phi_{l,n}\big|_{z=0} = 0$, and

$-\kappa_{eff,p}\nabla\phi_{l,p}\big|_{z=L_n+L_s+L_p} = 0$.

The electrochemical reaction flux in Eq. 7.2-7.4 is determined by the Butler-Volmer equation [36],

$$J_i = k_i\left(c_{s,i,max} - c_{s,i,surf}\right)^{0.5} c_{s,i,surf}{}^{0.5} c_i{}^{0.5} \times \left[\exp\left(\frac{0.5F}{RT}\eta_i\right) - \exp\left(\frac{-0.5F}{RT}\eta_i\right)\right] \tag{7.5}$$

where the overpotential for the electrochemical reaction, η_i, is defined as $\phi_{s,i} - \phi_{l,i} - U_i$.

The abovementioned system of coupled partial differential equations was solved in COMSOL Multiphysics 5.4 using finite element method. The model was solved using the multifrontal massively parallel sparse direct solver (MUMPS) [188, 189] and a backward differential formula (BDF) solver for time-stepping with a relative tolerance of 1×10^{-3}. A mesh sensitivity analysis was also performed to ensure the mesh independency of the results.

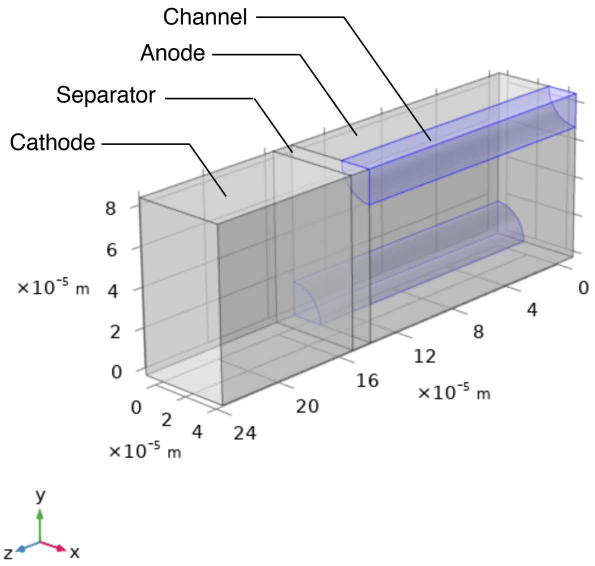

Figure 7.1. The configuration of the simulation domain representing one unit cell of the HOH electrode.

Results and Discussion

Model Validation

The electrodes that were used in this study were hard carbon (HC) anode and Nickel Cobalt Aluminum Oxide ($LiNi_{0.8}Co_{0.15}Al_{0.05}O_2$, NCA) cathode. The electrolyte was 1M $LiPF_6$ in 3:7 EC:EMC. The list of parameter values used in the electrochemical simulations is presented in Table 7.1. In all simulations, the temperature was fixed at 298.15 K. In order to test the validity of the estimated model parameters, the simulated anode and cathode voltage profiles at different rates were compared with the corresponding voltage profiles obtained from three-electrode cell with non-patterned (control) anode. As demonstrated in Figure 7.2, the model can accurately predict the anode and cathode voltage profiles at different rates obtained from three-electrode cell measurements with the control anode and a Li^+/Li reference electrode.

Table 7.1. The parameters used in the simulations and their sources.

Parameters	**Values**	**Units**	**Sources**
Anode			
Thickness	149	um	Experiment
Particle radius	3.50	um	Experiment
Electrolyte volume fraction	0.31	--	Experiment
Reaction rate constant	8.00×10^{-11}	m/s	Fitting
Effective Electrolyte diffusivity	$0.57 \times D_0$	m^2/s	Fitting†
Effective electrolyte conductivity	$0.57 \times S_0$	S/m	Fitting†
Reference concentration	30550	mol/m^3	[190]
Operational state of lithiation range	$0.02 - 0.70$	mol/m^3	Experiment
Li diffusion coefficient in active material	3.90×10^{-13}	m^2/s	Fitting
Electronic conductivity	100	S/m	Fitting
Cathode			
Thickness	84.5	um	Experiment
Particle radius	3.50	um	Experiment
Electrolyte volume fraction	0.22	--	Experiment
Reaction rate constant	3.00×10^{-11}	m/s	Fitting
Effective Electrolyte diffusivity	$0.47 \times D_0$	m^2/s	Fitting†
Effective electrolyte conductivity	$0.47 \times S_0$	S/m	Fitting†
Reference concentration	33956	mol/m^3	[190]
Operational state of lithiation range	$0.04 - 0.98$	mol/m^3	Experiment
Li diffusion coefficient in active material	6.0×10^{-15}	m^2/s	Fitting
Electronic conductivity	1.5	S/m	Fitting
Separator			
Thickness	12	um	Experiment
Electrolyte volume fraction	0.47	--	Experiment
Effective Electrolyte diffusivity	$0.57 \times D_0$	m^2/s	Fitting†
Effective electrolyte conductivity	$0.57 \times S_0$	S/m	Fitting†
Others			
1C charge current density	37.03	A/m^2	Experiment
Temperature	298.15	K	Experiment

†Expressions for D_0 and S_0 are obtained from the concentration dependent Li^+ ion diffusivity and conductivity equations presented in Ref. [191].

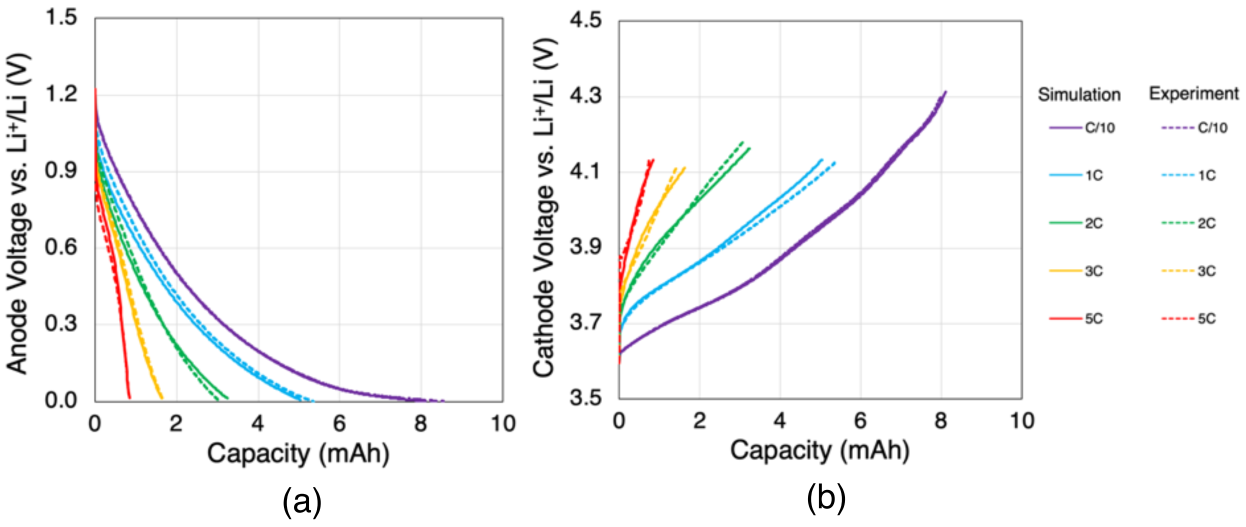

Figure 7.2. Simulated galvanostatic voltage profiles (solid lines) for (a) anode and (b) cathode at different rates compared with the corresponding experimental voltage profiles (dashed lines) obtained from three-electrode cell measurements with control anode.

The Effect of HOH on Rate Capability

In order to investigate the effect of HOH patterning on the rate capability of the electrode and the kinetics of lithium intercalation into the electrode, we employed our 3D model to simulate the isothermal galvanostatic charge cycles from C/10 to 6C for an HOH anode with a hole diameter and hole spacing of 35 μm and 100 μm, respectively. The constant-current (CC) charge capacity of the HOH anode at a cell cut-off voltage of 4.2 V was calculated and compared that with that of the control anode. As shown in Figure 7.3, the CC charge capacity of the HOH anode is higher than that of the control anode at C-rates above 2C. Figure 7.3 also shows that the improvement in CC charge capacity increases with C-rate, reaching to a maximum of ~20% at 6C for this specific HOH geometry.

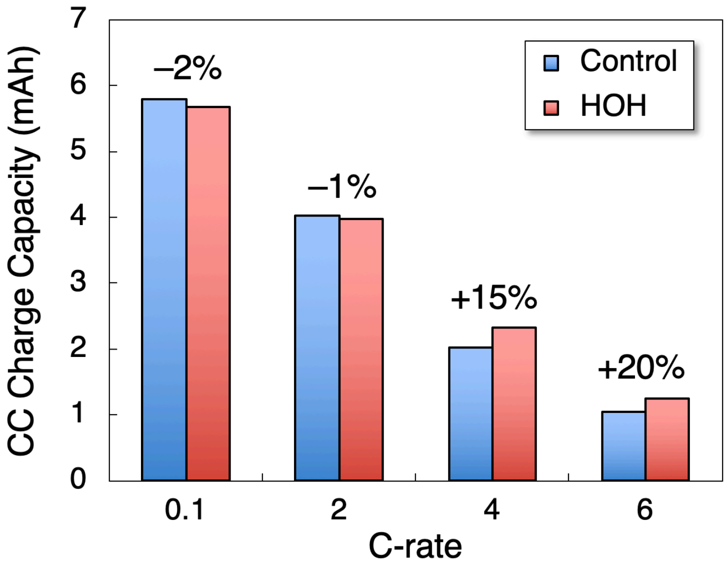

Figure 7.3. Calculated galvanostatic (CC) charge capacity of the control and HOH electrodes at different rates. The relative improvement in the CC charge capacity at each rate for this specific HOH geometry (35 μm diameter, 100 μm spacing) is shown with a percentage number above the corresponding columns.

The distribution of the electrolyte salt concentration in the control and HOH anode electrodes at the end of charge (cell cut-off voltage of 4.2 V) at 6C is shown in Figure 7.4. Moreover, Figure 7.5(a) shows the average electrolyte salt concentration at the end of charge cycle at 6C in the control and HOH anode electrodes across their thickness. Each point is obtained by taking the average of the electrolyte salt concentration in the electrode region that intersects with the corresponding *xy*-plane shown in Figure 7.5(b). The results show that in the HOH anode, the depletion zone of the electrolyte salt concentration is smaller compared to that in the control anode. Therefore, the vertical channels in the HOH electrode effectively reduce the electrolyte transport limitations, especially at high C-rates, resulting in an increased CC charge capacity.

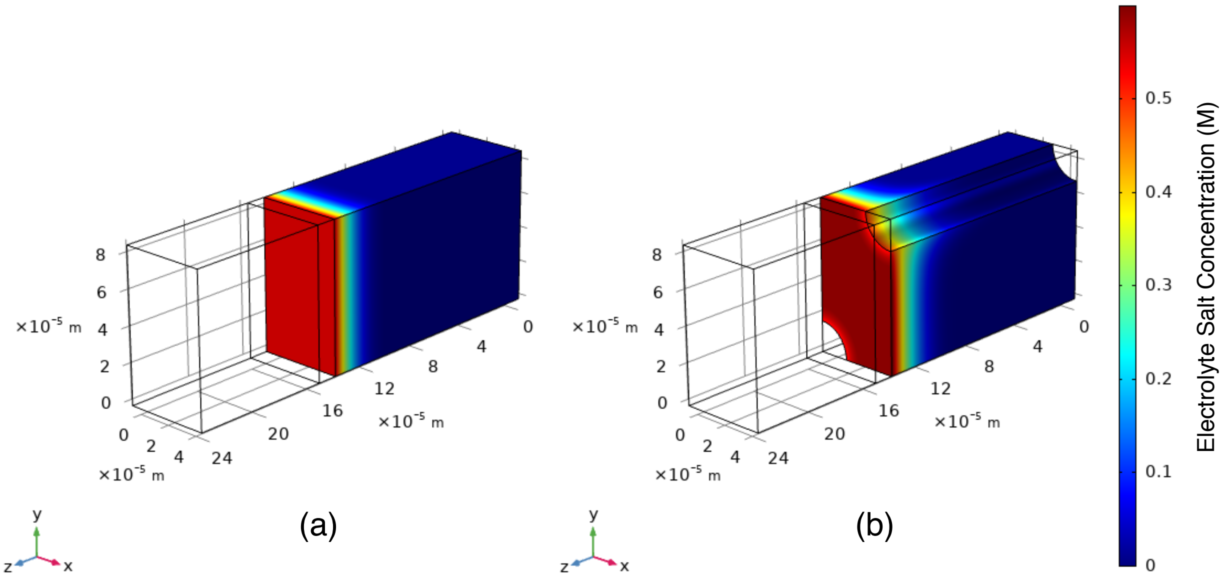

(a) (b)

Figure 7.4. The distribution of electrolyte salt concentration in the (a) control and (b) HOH anode electrodes at the end of charge at 6C.

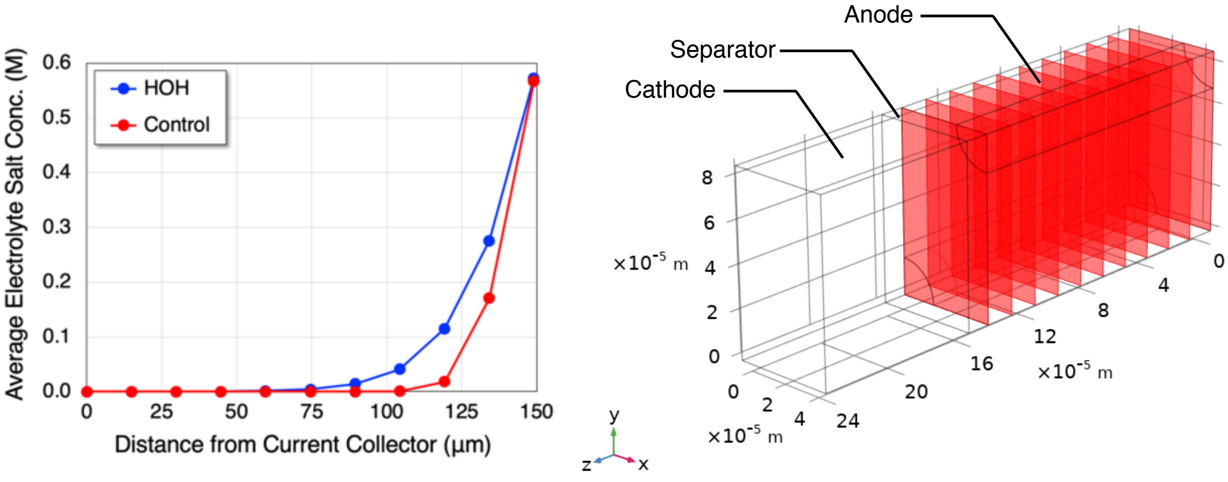

(a) (b)

Figure 7.5. (a) Electrolyte salt concentration averaged over the plane at a given distance from the current collector in the control (red) and HOH anode (blue) with a hole diameter and spacing of 35 μm and 100 μm, respectively, at the end of charge at 6C. Each data point in panel (a) is obtained by taking the average of the electrolyte salt concentration in the electrode region that intersects with the corresponding *xy*-plane shown in panel (b).

Figure 7.6 shows the vector field and streamlines of the electrolyte current density in the anode region during charge at 6C, which demonstrate the direction and path of the Li^+ ion transport in the electrolyte, respectively, with the colors indicating the magnitude of the electrolyte current density. The results presented in this figure show that in the control (non-patterned) electrode, the transport of Li^+ ions mainly occurs cross-plane from the separator to the anode during charge. However, in HOH electrodes, the vertical channels allow for in-plane Li^+ ion transport as well, therefore improving the rate capability of the electrode.

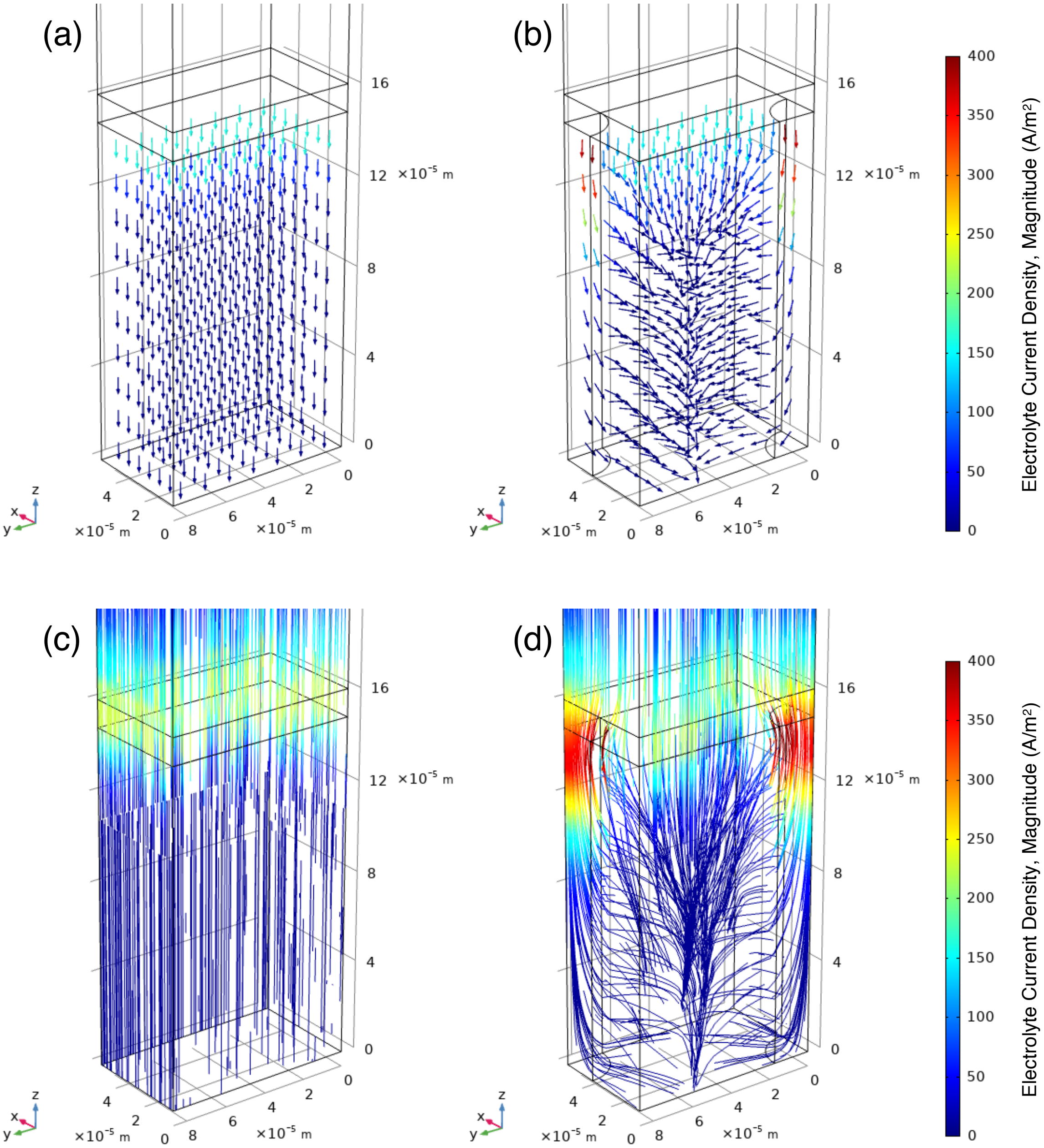

Figure 7.6. Vector field of the electrolyte current density for (a) control and (b) HOH electrodes. Electrolyte current density streamlines indicating the Li^+ ion transport path in the (c) control and (d) HOH electrodes.

Optimizing the HOH Geometry

Here we investigate the effect of hole diameter and hole spacing on the CC charge capacity of the HOH anode and optimize the HOH geometry to achieve maximum galvanostatic charge capacity. The volume retention for each geometry is defined as the ratio of the volume of the HOH electrode to the volume of the control electrode,

$$Volume\ Retention = \frac{h\left(\frac{S\sqrt{3}}{2}\times\frac{S}{2}-\frac{\pi D^2}{8}\right)}{h\left(\frac{S\sqrt{3}}{2}\times\frac{S}{2}\right)} = 1-\frac{D^2\left(\frac{\pi}{8}\right)}{S^2\left(\frac{\sqrt{3}}{4}\right)} = 1-\frac{\pi}{2\sqrt{3}}\left(\frac{D}{S}\right)^2 \tag{7.6}$$

where h is the electrode thickness, D is the hole diameter, and S is the hole spacing. Eq. (7.6) shows that the volume retention only depends on the ratio of the hole diameter to hole spacing. As shown in Figure 7.7(a), we exclude the geometries that result in a volume retention of less than 85%, since they lead to an N:P ratio of less than 1.0 if the N:P ratio of the cell with control anode is less than 1.2.

Figure 7.7(b) shows the CC charge capacity of the HOH anodes with varying geometries at 6C with a cell cut-off voltage of 4.2 V. The results show that the optimized hole diameter and spacing among the combinations examined are 15 μm and 40 μm, respectively, immediately followed by the geometry with a hole diameter and spacing of 40 μm and 100 μm, respectively. Both geometries result in more than 30% increase in the CC charge capacity when compared with the control anode.

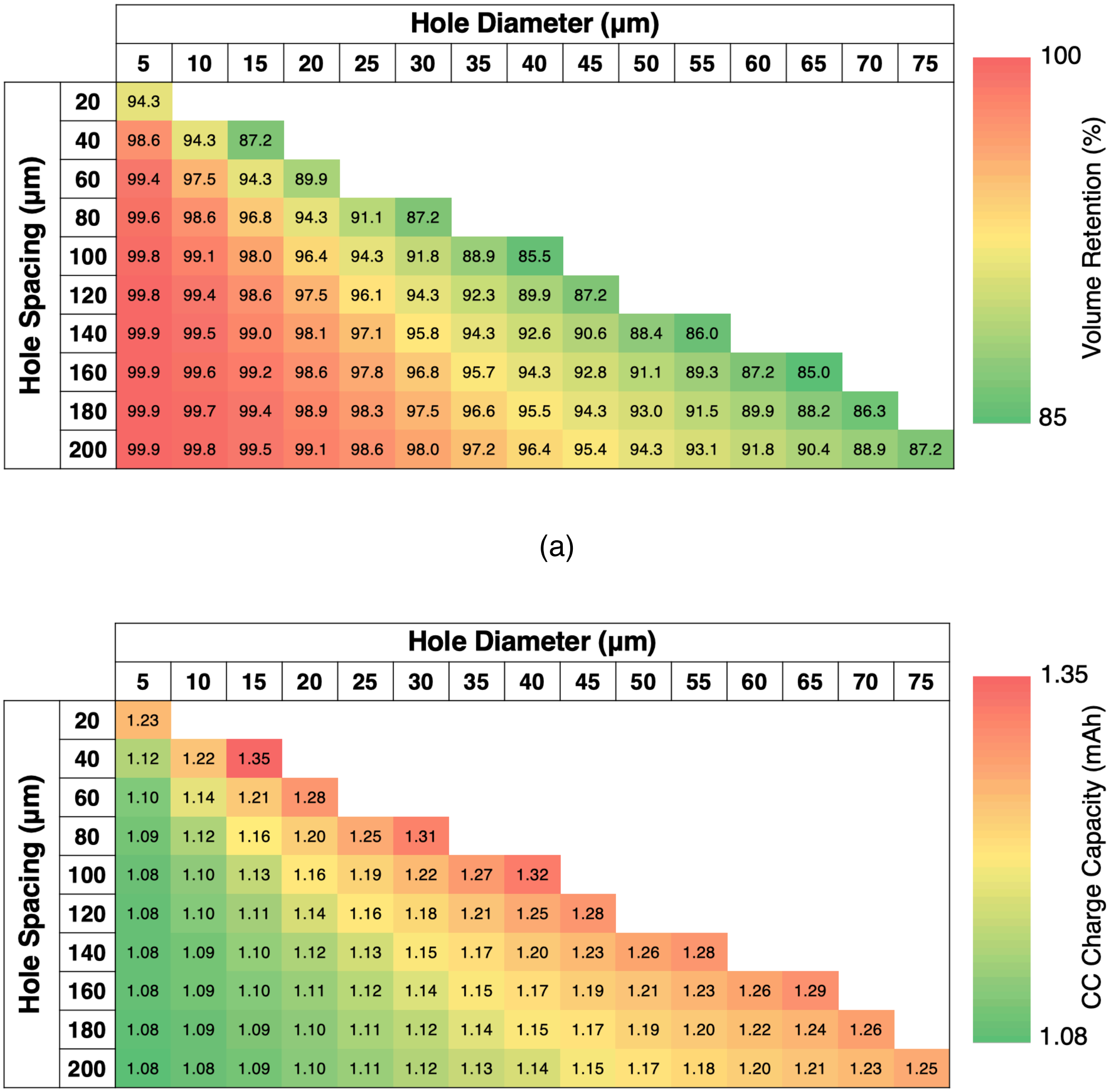

	Hole Diameter (µm)														
Hole Spacing (µm)	5	10	15	20	25	30	35	40	45	50	55	60	65	70	75
20	94.3														
40	98.6	94.3	87.2												
60	99.4	97.5	94.3	89.9											
80	99.6	98.6	96.8	94.3	91.1	87.2									
100	99.8	99.1	98.0	96.4	94.3	91.8	88.9	85.5							
120	99.8	99.4	98.6	97.5	96.1	94.3	92.3	89.9	87.2						
140	99.9	99.5	99.0	98.1	97.1	95.8	94.3	92.6	90.6	88.4	86.0				
160	99.9	99.6	99.2	98.6	97.8	96.8	95.7	94.3	92.8	91.1	89.3	87.2	85.0		
180	99.9	99.7	99.4	98.9	98.3	97.5	96.6	95.5	94.3	93.0	91.5	89.9	88.2	86.3	
200	99.9	99.8	99.5	99.1	98.6	98.0	97.2	96.4	95.4	94.3	93.1	91.8	90.4	88.9	87.2

(a)

	Hole Diameter (µm)														
Hole Spacing (µm)	5	10	15	20	25	30	35	40	45	50	55	60	65	70	75
20	1.23														
40	1.12	1.22	1.35												
60	1.10	1.14	1.21	1.28											
80	1.09	1.12	1.16	1.20	1.25	1.31									
100	1.08	1.10	1.13	1.16	1.19	1.22	1.27	1.32							
120	1.08	1.10	1.11	1.14	1.16	1.18	1.21	1.25	1.28						
140	1.08	1.09	1.10	1.12	1.13	1.15	1.17	1.20	1.23	1.26	1.28				
160	1.08	1.09	1.10	1.11	1.12	1.14	1.15	1.17	1.19	1.21	1.23	1.26	1.29		
180	1.08	1.09	1.09	1.10	1.11	1.12	1.14	1.15	1.17	1.19	1.20	1.22	1.24	1.26	
200	1.08	1.08	1.09	1.10	1.11	1.12	1.13	1.14	1.15	1.17	1.18	1.20	1.21	1.23	1.25

(b)

Figure 7.7. (a) The volume retention for HOH electrodes with different hole diameter and spacing. (b) The CC charge capacity of the HOH anode electrodes at 6C with a cell cut-off voltage of 4.2 V.

As shown in Figure 7.8, for geometries with a volume retention of greater than 85%, the CC charge capacity of the HOH electrodes increases with decrease in volume retention. The expression based on a linear regression on the data points can be used to estimate the CC charge capacity at 6C for a given volume retention between 85%-100%. Furthermore, as shown in

Figure 7.9, for a given hole diameter to spacing ratio, D/S, the CC charge capacity of the HOH electrode increases with decrease in hole diameter. In other words, for a specific volume retention, the CC charge capacity of the HOH electrode is higher for geometries in which the holes are smaller and closer together.

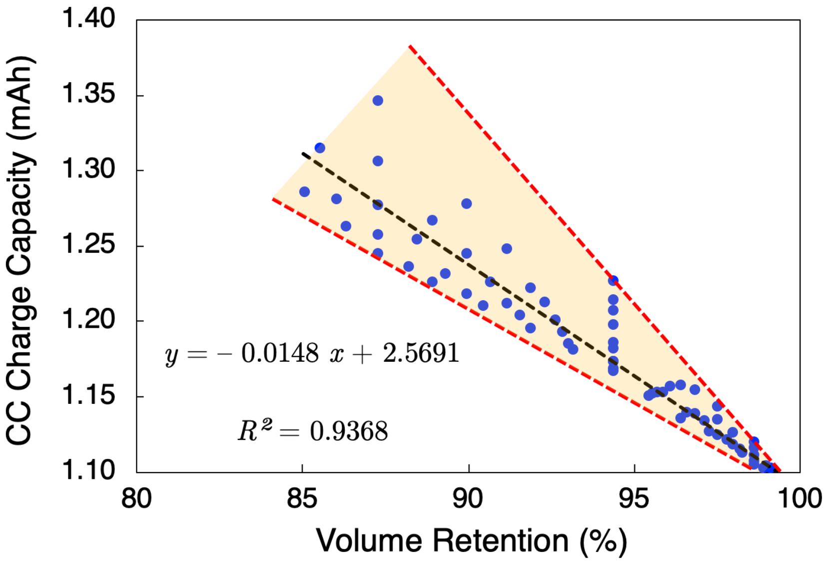

Figure 7.8. The variation of the CC charge capacity at 6C as a function of volume retention of the HOH electrode. The linear expression shown on the plot is the best first-order fit to all data points indicated by black dashed line. The red dashed lines indicate the expected upper/lower bounds of calculated capacities for each volume retention.

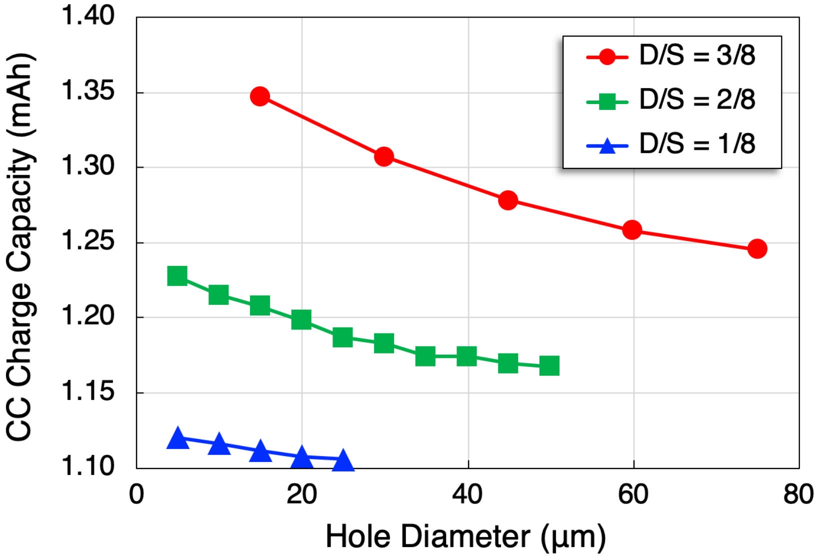

Figure 7.9. The variation of CC charge capacity at 6C as a function of hole diameter for HOH electrodes with three different diameter/spacing (D/S) ratios.

Figure 7.10 shows the effect of hole depth on the CC charge capacity of the HOH anodes at 6C with three different geometries that have the same volume retention. The depth of the hole was varied from ¼ to ⁴⁄₄ of the thickness of the electrode. The results indicate that while the accessible galvanostatic capacity of the HOH anode increases with increase in the hole depth, the rate of improvement decreases when the hole is deeper than ¼ of the thickness of the electrode.

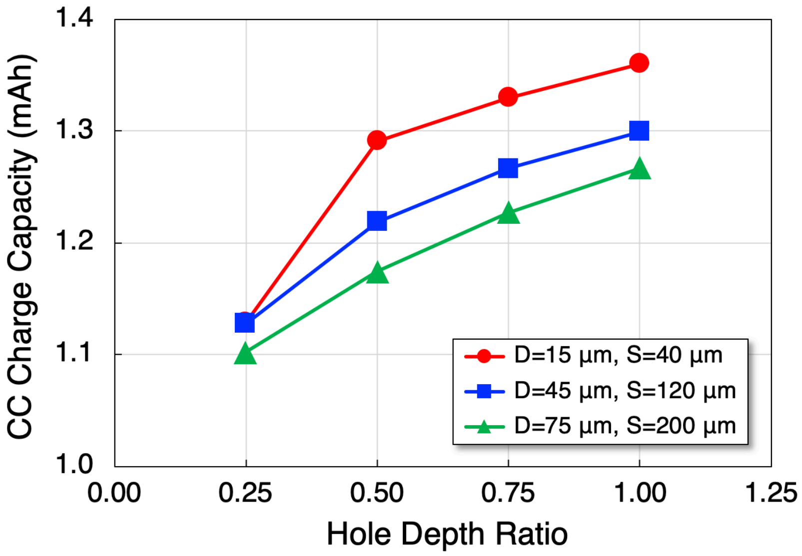

Figure 7.10. The CC charge capacity at 6C as a function of hole depth for geometries with the same diameter/spacing (D/S) ratio of 3/8.

Summary and Conclusions

In this chapter, we showed that introducing vertical channels through the thickness of the electrode is an effective method to suppress the Li ion transport limitations that occur during fast charging. We utilized our three-dimensional model based on the porous electrode theory to investigate the geometric parameters that affect the electrochemical performance of highly-ordered hierarchical (HOH) anodes under galvanostatic extreme fast charging conditions. Our simulations showed that the CC charge capacity of the HOH anode is higher than that of the control anode and this improvement in capacity increases with C-rate.

Furthermore, we investigated the effect of hole diameter and hole spacing on the CC charge capacity of the HOH anode and optimized the HOH geometry to achieve maximum CC charge capacity. We varied the hole diameter from 5 μm to 75 μm and the hole spacing from 20 μm to 200 μm, and calculated the maximum CC charge capacity of the cell with HOH anode at 6C with a cell cut-off voltage of 4.2 V. Our simulations showed that the optimized hole diameter and spacing among the combinations examined are 15 μm and 40 μm, respectively, immediately followed by the geometry with a hole diameter and spacing of 40 μm and 100 μm, respectively. Both geometries result in more than 30% increase in the CC charge capacity when compared with the control anode. Further analysis also indicated that for a given hole diameter to spacing ratio, the CC charge capacity of the HOH electrode increases with decrease in hole diameter. Therefore, for a specific volume retention, the CC charge capacity of the HOH electrode is higher for geometries in which the holes are smaller and closer together.

Lastly, we investigated the effect of hole depth on the galvanostatic charge capacity of the HOH electrodes. The results indicated that while the accessible galvanostatic capacity of the HOH anode increases with increase in the hole depth, the rate of improvement decreases when the hole is deeper than ¼ of the thickness of the electrode.

Chapter 8.

Summary and Future Work

Dissertation Summary

In this dissertation, we investigated the coupled effects thermodynamic and kinetic properties of battery electrodes on their time-dependent electrochemical behavior under various operating conditions. Three examples of electrochemical processes were considered that occur during the operation of metal anode and lithium-ion batteries: thermodynamics and kinetics of nucleation during electrodeposition in metal anode batteries, kinetics of lithium intercalation in electrode particles, and the electrochemical behavior of lithium-ion battery electrodes under various operating conditions. In order to study these systems, three different computational models were presented.

In chapter 1, an overview of the structure of lithium-ion batteries was presented along with the advantages and disadvantages of the most commonly used electrode materials. Chapter 2 provided a general overview of different battery modeling approaches, and in particular, the underlying physics, assumptions, and governing equations of the pseudo two-dimensional (P2D) model developed by Newman et al. [29, 30], which is extensively used in literature as a comprehensive physics-based approach for modeling batteries.

In chapter 3, a model based on the classical theory of nucleation was utilized to study the nucleation behavior of several metals during electrodeposition on metal anodes. The model uses the formation energies of critical nuclei obtained from density functional theory (DFT) calculations to estimate the time-dependent and steady-state nucleation rate and density on various metal anodes with potential applications in single- and multi-valent metal anode batteries. Nucleation rates were predicted to be several orders of magnitude larger on alkali metal surfaces than on the other metals. This multiscale model highlighted the sensitivity of the nucleation behavior on the structure and composition of the electrode surface.

In chapter 4 and 5, a continuum-scale model was introduced to study the kinetics of lithium ion transport in intercalating electrode particles. The model uses smoothed-boundary method to reformulate the governing partial differential equations, which allows for explicitly distinguishing different phases that are present in the model system. The simulations indicated that an open-circuit potential difference between the surface and bulk phases in a core-shell cathode particle leads to a charge/discharge asymmetry in the galvanostatic voltage profiles, causing a decrease in the accessible capacity of the particle. Moreover, further simulations showed that this reduction in the accessible capacity is smaller when the surface-phase diffusivity is higher than the bulk-phase diffusivity. These findings provided valuable guidance in developing a material design and selection criteria that ensures optimal electrochemical performance in core-shell heterostructure hybrid cathode particles.

In chapter 6, a continuum-scale model based on the porous electrode theory was developed to study the reaction heterogeneity in the composite porous electrode of a lithium-ion battery. These simulations allowed us to investigate the effect of various electrode and electrolyte properties on the reaction heterogeneity across the electrode thickness. The simulation results were also validated against the experimental data obtained from X-ray diffraction computed tomography (XRD-CT) measurements. Our simulations showed that accelerated reactions at the electrode faces in contact with either the separator or the current collector demonstrate that both ionic and electronic transport limit the reaction progress. The data quantify how nonuniformity of the electrode reaction leads to variability in the charge/discharge rate, both as a function of time and position within the electrode architecture. This rate heterogeneity may accelerate rate-dependent degradation pathways in regions of the composite electrode experiencing faster-than-average reaction and has important implications for understanding and optimizing rate-dependent battery performance.

In chapter 7, a three-dimensional continuum-scale model based on the porous electrode theory was developed to investigate the effect of introducing vertical channels through the thickness of the electrode on the Li ion transport during fast charging. These simulations allowed us to investigate the geometric parameters that affect the electrochemical performance of highly-ordered hierarchical (HOH) anodes under galvanostatic extreme fast charging conditions. Our analysis shows that the HOH anode architecture with optimized geometric parameters (i.e., hole diameter and spacing) can improve the galvanostatic charge capacity of the electrode at high rates by minimizing the transport limitations that occur during extreme fast charging conditions. Further analysis also indicated that for a given hole diameter to spacing ratio, the galvanostatic charge capacity of the HOH electrode increases with decrease in hole diameter. Therefore, for a specific volume retention, the galvanostatic charge capacity of the HOH electrode is higher for geometries in which the holes are smaller and closer together.

Future Work

The models presented in this dissertation could be extended to include other physical and chemical processes that are involved in electrochemical systems.

Extensions of the 1D model presented in chapter 4 and 5 can be developed to investigate the mechanical stress induced in electrode particles due to their volume change during charge/discharge. The mechanical stress in hybrid cathode particles with two or more different materials results in a non-homogenous strain due to the difference in the volume change of these materials during lithiation/delithiation process. As a result, depending on the distribution of stress, particle cracking may accelerate under such circumstances.

The 3D implementation of the porous electrode theory with representative volume described in chapter 6, assumes uniform lithium concentration throughout the particle. Such assumption may not hold true under high-rate charge/discharge or in electrodes with larger particles. Therefore, the addition of solid-state transport equation will be necessary to make the model applicable to a wider range of electrodes and operating conditions. For instance, transport limitations that occur under fast charge/discharge conditions can be captured more accurately by solving the diffusion equation with a reaction rate source term at the particle-electrolyte interface. This allows for the evaluation of spatial distribution and temporal evolution of lithium concentration in the electrode particles.

Beyond examining different geometries of HOH electrode, the model presented in chapter 7 can be utilized to optimize fast charging strategies with a combination of constant current (CC) and constant voltage (CV) steps. Additionally, the presented model can be coupled with heat transfer physics to account for the variation of cell temperature during fast charging, especially in large format cells. One of the major issues that can result in irreversible capacity loss during fast charging is lithium plating, which can occur more severely in low temperatures. Therefore, increasing the cell temperature before fast charging starts can improve the cycle life of the battery by decreasing the possibility of lithium plating. On the other hand, higher temperatures can accelerate the side reactions responsible for electrolyte and particle degradation in the battery. Therefore, an optimum temperature range exists for fast charging, which depends on the electrode materials, electrolyte composition and additives, and cell design. The addition of heat transfer physics and introducing side reactions to the model described in chapter 7 allows for a detailed study on the effect of fast charging on cell degradation mechanisms.

Bibliography

[1] V. Etacheri, R. Marom, R. Elazari, G. Salitra, and D. Aurbach, "Challenges in the development of advanced Li-ion batteries: a review," *Energy & Environmental Science,* vol. 4, no. 9, pp. 3243-3262, Sep 2011, doi: 10.1039/c1ee01598b.

[2] J. W. Fergus, "Recent developments in cathode materials for lithium ion batteries," *Journal of Power Sources,* vol. 195, no. 4, pp. 939-954, Feb 15 2010, doi: 10.1016/j.jpowsour.2009.08.089.

[3] G. Girishkumar, B. McCloskey, A. C. Luntz, S. Swanson, and W. Wilcke, "Lithium - Air Battery: Promise and Challenges," *J. Phys. Chem. Lett.,* vol. 1, no. 14, pp. 2193-2203, Jul 15 2010, doi: 10.1021/jz1005384.

[4] B. Nykvist and M. Nilsson, "Rapidly falling costs of battery packs for electric vehicles," *Nature Climate Change,* vol. 5, no. 4, pp. 329-332, Apr 2015, doi: 10.1038/nclimate2564.

[5] B. Dunn, H. Kamath, and J. M. Tarascon, "Electrical Energy Storage for the Grid: A Battery of Choices," *Science,* vol. 334, no. 6058, pp. 928-935, Nov 2011, doi: 10.1126/science.1212741.

[6] M. T. Lawder *et al.*, "Battery Energy Storage System (BESS) and Battery Management System (BMS) for Grid-Scale Applications," *Proceedings of the Ieee,* vol. 102, no. 6, pp. 1014-1030, Jun 2014, doi: 10.1109/jproc.2014.2317451.

[7] A. Bizeray, "State and Parameter Estimation of Physics-Based Lithium-Ion Battery Models," Doctor of Philosophy, Department of Engineering Science, University of Oxford, United Kingdom, 2016.

[8] J. Newman and K. E. Thomas-Alyea, *Electrochemical Systems*, Third ed. Hoboken, New Jersy: John Wiley & Sons Inc., 2004, p. 672.

[9] J. Lu, Z. Chen, F. Pan, Y. Cui, and K. Amine, "High-Performance Anode Materials for Rechargeable Lithium-Ion Batteries," *Electrochemical Energy Reviews,* vol. 1, pp. 35-53, 2018.

[10] A. F. Chadwick, "Models of Electrode and Electrolyte Behavior at the Continuum Scale," Doctor of Philosophy, Department of Materials Science and Engineering, University of Michigan, United States, 2018.

[11] Y. Mekonnen, A. Sundararajan, A. I. Sarwat, and Ieee, "A Review of Cathode and Anode Materials for Lithium-Ion Batteries," in *SoutheastCon*, Norfolk, VA, Mar 30-Apr

03 2016, in IEEE SoutheastCon-Proceedings, 2016. [Online]. Available: <Go to ISI>://WOS:000387067900092

[12] S. T. Myung *et al.*, "Nickel-Rich Layered Cathode Materials for Automotive Lithium-Ion Batteries: Achievements and Perspectives," *Acs Energy Letters,* vol. 2, no. 1, pp. 196-223, Jan 2017, doi: 10.1021/acsenergylett.6b00594.

[13] J. Deng, C. Bae, J. Marcicki, A. Masias, and T. Miller, "Safety modelling and testing of lithium-ion batteries in electrified vehicles," *Nature Energy,* vol. 3, no. 4, pp. 261-266, Apr 2018, doi: 10.1038/s41560-018-0122-3.

[14] G. D. Fan, K. Pan, G. L. Storti, M. Canova, J. Marcicki, and X. G. Yang, "A Reduced-Order Multi-Scale, Multi-Dimensional Model for Performance Prediction of Large-Format Li-Ion Cells," *Journal of the Electrochemical Society,* vol. 164, no. 2, pp. A252-A264, 2017, doi: 10.1149/2.0791702jes.

[15] J. Marcicki, X. G. Yang, and P. Rairigh, "Fault Current Measurements during Crush Testing of Electrically Parallel Lithium-Ion Battery Modules," *Ecs Electrochemistry Letters,* vol. 4, no. 9, pp. A97-A99, 2015, doi: 10.1149/2.0011509eel.

[16] J. Marcicki *et al.*, "A Simulation Framework for Battery Cell Impact Safety Modeling Using LS-DYNA," *Journal of the Electrochemical Society,* vol. 164, no. 1, pp. A6440-A6448, 2017, doi: 10.1149/2.0661701jes.

[17] S. Kazemiabnavi, P. Dutta, and S. Banerjee, "Density Functional Theory Based Study of the Electron Transfer Reaction at the Lithium Metal Anode in a Lithium–Air Battery with Ionic Liquid Electrolytes," *The Journal of Physical Chemistry C,* vol. 118, no. 47, pp. 27183–27192, 2014, doi: 10.1021/jp506563j.

[18] F. Zhou, M. Cococcioni, K. Kang, and G. Ceder, "The Li intercalation potential of LiMPO4 and LiMSiO4 olivines with M = Fe, Mn, Co, Ni," *Electrochemistry Communications,* vol. 6, no. 11, pp. 1144-1148, Nov 2004, doi: 10.1016/j.elecom.2004.09.007.

[19] S. Kazemiabnavi, P. Dutta, and S. Banerjee, "A Density Functional Theory Based Study of the Electron Transfer Reaction at the Cathode–Electrolyte Interface in Lithium–Air Batteries," *Physical Chemistry Chemical Physics,* vol. 17, pp. 11740-11751, 2015, doi: 10.1039/C4CP06121G.

[20] M. D. Radin, F. Tian, and D. J. Siegel, "Electronic structure of Li2O2 {0001} surfaces," *Journal of Materials Science,* vol. 47, no. 21, pp. 7564-7570, Nov 2012, doi: 10.1007/s10853-012-6552-6.

[21] S. Kazemiabnavi, Z. C. Zhang, K. Thornton, and S. Banerjee, "Electrochemical Stability Window of Imidazolium-Based Ionic Liquids as Electrolytes for Lithium Batteries," *Journal of Physical Chemistry B,* vol. 120, no. 25, pp. 5691-5702, Jun 2016, doi: 10.1021/acs.jpcb.6b03433.

[22] S. Kazemiabnavi, P. Dutta, and S. Banerjee, "Ab Initio Modeling of the Electron Transfer Reaction Rate at the Electrode-Electrolyte Interface in Lithium-Air Batteries," in *ASME 2014 International Mechanical Engineering Congress and Exposition*, Montreal, Canada, 2014, vol. 6A: Energy: American Society of Mechanical Engineers, doi: 10.1115/IMECE2014-40239.

[23] K. S. Nagy, S. Kazemiabnavi, K. Thornton, and D. J. Siegel, "Thermodynamic Overpotentials and Nucleation Rates for Electrodeposition on Metal Anodes," *Acs Applied Materials & Interfaces,* vol. 11, no. 8, pp. 7954-7964, Feb 2019, doi: 10.1021/acsami.8b19787.

[24] K. Yoo, A. M. Dive, S. Kazemiabnavi, S. Banerjee, and P. Dutta, "Effects of Operating Temperature on the Electrical Performance of a Li-air Battery operated with Ionic Liquid Electrolyte," *Electrochimica Acta,* vol. 194, pp. 317–329, 2016, doi: 10.1016/j.electacta.2016.02.099.

[25] S. P. Ong, O. Andreussi, Y. Wu, N. Marzari, and G. Ceder, "Electrochemical Windows of Room-Temperature Ionic Liquids from Molecular Dynamics and Density Functional Theory Calculations," *Chem. Mater.,* vol. 23, no. 11, pp. 2979-2986, Jun 14 2011, doi: 10.1021/cm200679y.

[26] H. Liu *et al.*, "Effects of Antisite Defects on Li Diffusion in LifePO(4) Revealed, by Li Isotope Exchange," *Journal of Physical Chemistry C,* vol. 121, no. 22, pp. 12025-12036, Jun 2017, doi: 10.1021/acs.jpcc.7b02819.

[27] S. Kazemiabnavi, R. Malik, B. Orvananos, A. Abdellahi, G. Ceder, and K. Thornton, "The effect of surface-bulk potential difference on the kinetics of intercalation in core-shell active cathode particles," *Journal of Power Sources,* vol. 382, pp. 30-37, Apr 2018, doi: 10.1016/j.jpowsour.2018.02.023.

[28] H. Liu *et al.*, "Quantifying Reaction and Rate Heterogeneity in Battery Electrodes in 3D through Operando X-ray Diffraction Computed Tomography," *Acs Applied Materials & Interfaces,* vol. 11, no. 20, pp. 18386-18394, May 2019, doi: 10.1021/acsami.9b02173.

[29] M. Doyle, T. F. Fuller, and J. Newman, "Modeling of Galvanostatic Charge and Discharge of the Lithium/Polymer/Insertion Cell," *Journal of the Electrochemical Society,* vol. 140, no. 6, pp. 1526-1533, Jun 1993, doi: 10.1149/1.2221597.

[30] T. F. Fuller, M. Doyle, and J. Newman, "Simulation and Optimization of the Dual Lithium Ion Insertion Cell," *Journal of the Electrochemical Society,* vol. 141, no. 1, pp. 1-10, Jan 1994, doi: 10.1149/1.2054684.

[31] G. L. Plett, "Extended Kalman filtering for battery management systems of LiPB-based HEV battery packs - Part 3. State and parameter estimation," *Journal of Power Sources,* vol. 134, no. 2, pp. 277-292, Aug 2004, doi: 10.1016/j.jpowsour.2004.02.033.

[32] X. S. Hu, S. B. Li, and H. Peng, "A comparative study of equivalent circuit models for Li-ion batteries," *Journal of Power Sources,* vol. 198, pp. 359-367, Jan 2012, doi: 10.1016/j.jpowsour.2011.10.013.

[33] D. Andre, M. Meiler, K. Steiner, H. Walz, T. Soczka-Guth, and D. U. Sauer, "Characterization of high-power lithium-ion batteries by electrochemical impedance spectroscopy. II: Modelling," *Journal of Power Sources,* vol. 196, no. 12, pp. 5349-5356, Jun 2011, doi: 10.1016/j.jpowsour.2010.07.071.

[34] S. M. M. Alavi, C. R. Birkl, and D. A. Howey, "Time-domain fitting of battery electrochemical impedance models," *Journal of Power Sources,* vol. 288, pp. 345-352, Aug 2015, doi: 10.1016/j.jpowsour.2015.04.099.

[35] J. Newman and W. Tiedemann, "Porous-electrode theory with battery applications," *Aiche Journal,* vol. 21, no. 1, pp. 25-41, 1975, doi: 10.1002/aic.690210103.

[36] L. Cai and R. E. White, "Mathematical modeling of a lithium ion battery with thermal effects in COMSOL Inc. Multiphysics (MP) software," *Journal of Power Sources,* vol. 196, no. 14, pp. 5985-5989, Jul 2011, doi: 10.1016/j.jpowsour.2011.03.017.

[37] H. Kim, G. Jeong, Y. U. Kim, J. H. Kim, C. M. Park, and H. J. Sohn, "Metallic anodes for next generation secondary batteries," *Chemical Society Reviews,* vol. 42, no. 23, pp. 9011-9034, 2013, doi: 10.1039/c3cs60177c.

[38] H. D. Yoo, I. Shterenberg, Y. Gofer, G. Gershinsky, N. Pour, and D. Aurbach, "Mg rechargeable batteries: an on-going challenge," *Energy & Environmental Science,* vol. 6, no. 8, pp. 2265-2279, Aug 2013, doi: 10.1039/c3ee40871j.

[39] B. L. Ellis and L. F. Nazar, "Sodium and sodium-ion energy storage batteries," *Current Opinion in Solid State & Materials Science,* vol. 16, no. 4, pp. 168-177, Aug 2012, doi: 10.1016/j.cossms.2012.04.002.

[40] G. Crabtree, "The Joint Center for Energy Storage Research: A New Paradigm for Battery Research and Development," in *3rd Physics of Sustainable Energy (PSE) Conference*, Berkeley, CA, Mar 08-09 2014, vol. 1652, in AIP Conference Proceedings, 2015, pp. 112-128, doi: 10.1063/1.4916174. [Online]. Available: <Go to ISI>://WOS:000354881700011

[41] K. Brandt, "Historical Development of Secondary Lithium Batteries," *Solid State Ionics,* vol. 69, no. 3-4, pp. 173-183, Aug 1994, doi: 10.1016/0167-2738(94)90408-1.

[42] A. H. Tullo, "Batteries that breathe air," *Chemical & Engineering News,* vol. 95, no. 9, pp. 21-22, Feb 2017.

[43] D. Aurbach *et al.*, "Prototype systems for rechargeable magnesium batteries," *Nature,* vol. 407, no. 6805, pp. 724-727, Oct 12 2000, doi: 10.1038/35037553.

[44] J. Muldoon, C. B. Bucur, and T. Gregory, "Quest for Nonaqueous Multivalent Secondary Batteries: Magnesium and Beyond," *Chemical Reviews,* vol. 114, no. 23, pp. 11683-11720, Dec 2014, doi: 10.1021/cr500049y.

[45] T. R. Zhang, Z. L. Tao, and J. Chen, "Magnesium-air batteries: from principle to application," *Materials Horizons,* vol. 1, no. 2, pp. 196-206, Mar 2014, doi: 10.1039/c3mh00059a.

[46] "Phinergy Product Page." http://www.phinergy.com/product/ (accessed December 6, 2019).

[47] S. Licht, G. Levitin, C. Yarnitzky, and R. Tel-Vered, "The organic phase for aluminum batteries," *Electrochemical and Solid State Letters,* vol. 2, no. 6, pp. 262-264, Jun 1999, doi: 10.1149/1.1390805.

[48] Y. Nakayama *et al.*, "Sulfone-based electrolytes for aluminium rechargeable batteries," *Physical Chemistry Chemical Physics,* vol. 17, no. 8, pp. 5758-5766, 2015, doi: 10.1039/c4cp02183e.

[49] F. Endres, "Ionic liquids: Solvents for the electrodeposition of metals and semiconductors," *Chemphyschem,* vol. 3, no. 2, pp. 144-154, Feb 2002, doi: 10.1002/1439-7641(20020215)3:2<144::aid-cphc144>3.0.co;2-%23.

[50] T. Jiang, M. J. C. Brym, G. Dube, A. Lasia, and G. M. Brisard, "Electrodeposition of aluminium from ionic liquids: Part I - electrodeposition and surface morphology of aluminium from aluminium chloride (AlCl3)-l-ethyl-3-methylimidazolium chloride (EMIm Cl) ionic liquids," *Surface & Coatings Technology,* vol. 201, no. 1-2, pp. 1-9, Sep 2006, doi: 10.1016/j.surfcoat.2005.10.046.

[51] T. Jiang, M. J. C. Brym, G. Dube, A. Lasia, and G. M. Brisard, "Electrodeposition of aluminium from ionic liquids: Part II - studies on the electrodeposition of aluminum from aluminum chloride (AICl(3)) - trimethylphenylammonium chloride (TMPAC) ionic liquids," *Surface & Coatings Technology,* vol. 201, no. 1-2, pp. 10-18, Sep 2006, doi: 10.1016/j.surfcoat.2005.12.024.

[52] J. Q. Deng, W. B. Luo, S. L. Chou, H. K. Liu, and S. X. Dou, "Sodium-Ion Batteries: From Academic Research to Practical Commercialization," *Advanced Energy Materials,* vol. 8, no. 4, Feb 2018, Art no. 1701428, doi: 10.1002/aenm.201701428.

[53] P. Adelhelm, P. Hartmann, C. L. Bender, M. Busche, C. Eufinger, and J. Janek, "From lithium to sodium: cell chemistry of room temperature sodium-air and sodium-sulfur batteries," *Beilstein Journal of Nanotechnology,* vol. 6, pp. 1016-1055, Apr 2015, doi: 10.3762/bjnano.6.105.

[54] X. D. Ren and Y. Y. Wu, "A Low-Overpotential Potassium-Oxygen Battery Based on Potassium Superoxide," *Journal of the American Chemical Society,* vol. 135, no. 8, pp. 2923-2926, Feb 2013, doi: 10.1021/ja312059q.

[55] Q. Zhao, Y. X. Hu, K. Zhang, and J. Chen, "Potassium-Sulfur Batteries: A New Member of Room-Temperature Rechargeable Metal-Sulfur Batteries," *Inorganic Chemistry,* vol. 53, no. 17, pp. 9000-9005, Sep 2014, doi: 10.1021/ic500919e.

[56] D. Aurbach, R. Skaletsky, and Y. Gofer, "THE ELECTROCHEMICAL-BEHAVIOR OF CALCIUM ELECTRODES IN A FEW ORGANIC ELECTROLYTES," *Journal of the Electrochemical Society,* vol. 138, no. 12, pp. 3536-3545, Dec 1991, doi: 10.1149/1.2085455.

[57] A. Ponrouch, D. Monti, A. Boschin, B. Steen, P. Johansson, and M. R. Palacin, "Non-aqueous electrolytes for sodium-ion batteries," *Journal of Materials Chemistry A,* vol. 3, no. 1, pp. 22-42, 2015, doi: 10.1039/c4ta04428b.

[58] D. Wang, X. W. Gao, Y. H. Chen, L. Y. Jin, C. Kuss, and P. G. Bruce, "Plating and stripping calcium in an organic electrolyte," *Nature Materials,* vol. 17, no. 1, pp. 16-20, Jan 2018, doi: 10.1038/nmat5036.

[59] Z. Liu *et al.*, "Dendrite-Free Nanocrystalline Zinc Electrodeposition from an Ionic Liquid Containing Nickel Triflate for Rechargeable Zn-Based Batteries," *Angewandte Chemie-International Edition,* vol. 55, no. 8, pp. 2889-2893, Feb 2016, doi: 10.1002/anie.201509364.

[60] H. Chang and C. Lim, "Zinc deposition during charging nickel/zinc batteries," *Journal of Power Sources,* vol. 66, no. 1-2, pp. 115-119, May-Jun 1997, doi: 10.1016/s0378-7753(96)02536-0.

[61] M. Paunovic and M. Schlesinger, *Fundamentals of Electrochemical Deposition*, Second ed. John Wiley & Sons, Inc., 2006.

[62] J. S. Hummelshoj, A. C. Luntz, and J. K. Norskov, "Theoretical evidence for low kinetic overpotentials in Li-O-2 electrochemistry," *Journal of Chemical Physics,* vol. 138, no. 3, Jan 2013, Art no. 034703, doi: 10.1063/1.4773242.

[63] A. Sahari, A. Azizi, G. Schmerber, and A. Dinia, "Nucleation, Growth, and Morphological Properties of Electrodeposited Nickel Films from Different Baths," *Surface Review and Letters,* vol. 15, no. 6, pp. 717-725, Dec 2008.

[64] M. Willis and R. Alkire, "Additive-Assisted Nucleation and Growth by Electrodeposition I. Experimental Studies with Copper Seed Arrays on Gold Films," *Journal of the Electrochemical Society,* vol. 156, no. 10, pp. D377-D384, 2009, doi: 10.1149/1.3183502.

[65] R. M. Stephens, M. Willis, and R. C. Alkire, "Additive-Assisted Nucleation and Growth by Electrodeposition II. Mathematical Model and Comparison with Experimental Data," *Journal of the Electrochemical Society,* vol. 156, no. 10, pp. D385-D394, 2009, doi: 10.1149/1.3183505.

[66] W. A. Saidi, "Density Functional Theory Study of Nucleation and Growth of Pt Nanoparticles on MoS2(001) Surface," *Crystal Growth & Design,* vol. 15, no. 2, pp. 642-652, Feb 2015, doi: 10.1021/cg5013395.

[67] F. Ferrante, A. Prestianni, R. Cortese, R. Schimmenti, and D. Duca, "Density Functional Theory Investigation on the Nucleation of Homo and Heteronuclear Metal Clusters on Defective Graphene," *Journal of Physical Chemistry C,* vol. 120, no. 22, pp. 12022-12031, Jun 2016, doi: 10.1021/acs.jpcc.6b02833.

[68] A. Prestianni, F. Ferrante, E. M. Sulman, and D. Duca, "Density Functional Theory Investigation on the Nucleation and Growth of Small Palladium Clusters on a Hyper-Cross-Linked Polystyrene Matrix," *Journal of Physical Chemistry C,* vol. 118, no. 36, pp. 21006-21013, Sep 2014, doi: 10.1021/jp506320z.

[69] W. R. Tyson and W. A. Miller, "SURFACE FREE-ENERGIES OF SOLID METALS - ESTIMATION FROM LIQUID SURFACE-TENSION MEASUREMENTS," *Surface Science,* vol. 62, no. 1, pp. 267-276, 1977, doi: 10.1016/0039-6028(77)90442-3.

[70] F. R. de Boer, R. Boom, W. C. M. Mattens, A. R. Miedema, and A. K. Niessen, *Cohesion in Metals: Transition Metal Alloys*. North-Holland: Amsterdam, 1988.

[71] A. R. Miedema, "SURFACE ENERGIES OF SOLID METALS," *Zeitschrift Fur Metallkunde,* vol. 69, no. 5, pp. 287-292, 1978.

[72] A. R. Miedema and R. Boom, "SURFACE-TENSION AND ELECTRON-DENSITY OF PURE LIQUID-METALS," *Zeitschrift Fur Metallkunde,* vol. 69, no. 3, pp. 183-190, 1978.

[73] S. Hayun *et al.*, "Experimental Methodologies for Assessing the Surface Energy of Highly Hygroscopic Materials: The Case of Nanocrystalline Magnesia," *Journal of Physical Chemistry C,* vol. 115, no. 48, pp. 23929-23935, Dec 2011, doi: 10.1021/jp2087434.

[74] J. G. Smith, J. Naruse, H. Hiramatsu, and D. J. Siegel, "Theoretical Limiting Potentials in Mg/O-2 Batteries," *Chemistry of Materials,* vol. 28, no. 5, pp. 1390-1401, Mar 2016, doi: 10.1021/acs.chemmater.5b04501.

[75] W. R. Tyson, "SURFACE ENERGIES OF SOLID METALS," *Canadian Metallurgical Quarterly,* vol. 14, no. 4, pp. 307-314, 1975.

[76] J. K. Norskov *et al.*, "Origin of the overpotential for oxygen reduction at a fuel-cell cathode," *Journal of Physical Chemistry B,* vol. 108, no. 46, pp. 17886-17892, Nov 2004, doi: 10.1021/jp047349j.

[77] J. Rossmeisl, Z. W. Qu, H. Zhu, G. J. Kroes, and J. K. Norskov, "Electrolysis of water on oxide surfaces," *Journal of Electroanalytical Chemistry,* vol. 607, no. 1-2, pp. 83-89, Sep 2007, doi: 10.1016/j.jelechem.2006.11.008.

[78] I. C. Man *et al.*, "Universality in Oxygen Evolution Electrocatalysis on Oxide Surfaces," *Chemcatchem,* vol. 3, no. 7, pp. 1159-1165, Jul 2011, doi: 10.1002/cctc.201000397.

[79] S. Siahrostami *et al.*, "First principles investigation of zinc-anode dissolution in zinc-air batteries," *Physical Chemistry Chemical Physics,* vol. 15, no. 17, pp. 6416-6421, 2013, doi: 10.1039/c3cp50349f.

[80] V. Viswanathan, J. K. Norskov, A. Speidel, R. Scheffler, S. Gowda, and A. C. Luntz, "Li-O-2 Kinetic Overpotentials: Tafel Plots from Experiment and First-Principles Theory," *Journal of Physical Chemistry Letters,* vol. 4, no. 4, pp. 556-560, Feb 2013, doi: 10.1021/jz400019y.

[81] L. D. Chen, J. K. Norskov, and A. C. Luntz, "Al-Air Batteries: Fundamental Thermodynamic Limitations from First-Principles Theory," *Journal of Physical Chemistry Letters,* vol. 6, no. 1, pp. 175-179, Jan 2015, doi: 10.1021/jz502422v.

[82] M. Jackle and A. Gross, "Microscopic properties of lithium, sodium, and magnesium battery anode materials related to possible dendrite growth," *Journal of Chemical Physics,* vol. 141, no. 17, Nov 2014, Art no. 174710, doi: 10.1063/1.4901055.

[83] S. Toschev and I. Markov, "Transient Nucleation in Electrodeposition of Mercury," *Journal of Crystal Growth,* vol. 3-4, pp. 436–440, 1968.

[84] R. W. Balluffi, S. M. Allen, and W. C. Carter, R. A. Kemper, Ed. *Kinetics of Materials*. Hoboken, NJ, USA: John Wiley & Sons, Inc., 2005, p. 672.

[85] Y. D. Gamburg and G. Zangari, "Theory and Practice of Metal Electrodeposition," *Theory and Practice of Metal Electrodeposition,* pp. 1-378, 2011 2011, doi: 10.1007/978-1-4419-9669-5.

[86] R. A. Enrique, S. DeWitt, and K. Thornton, "Morphological stability during electrodeposition," *Mrs Communications,* vol. 7, no. 3, pp. 658-663, Sep 2017, doi: 10.1557/mrc.2017.38.

[87] G. Garcia, E. Ventosa, and W. Schuhmann, "Complete Prevention of Dendrite Formation in Zn Metal Anodes by Means of Pulsed Charging Protocols," *Acs Applied Materials & Interfaces,* vol. 9, no. 22, pp. 18691-18698, Jun 2017, doi: 10.1021/acsami.7b01705.

[88] D. Rehnlund, C. Ihrfors, J. Maibach, and L. Nyholm, "Dendrite-free lithium electrode cycling via controlled nucleation in low LiPF6 concentration electrolytes," *Materials Today,* vol. 21, no. 10, pp. 1010-1018, Dec 2018, doi: 10.1016/j.mattod.2018.08.003.

[89] W. M. Kang *et al.*, "A review of recent developments in rechargeable lithium-sulfur batteries," *Nanoscale,* vol. 8, no. 37, pp. 16541-16588, 2016, doi: 10.1039/c6nr04923k.

[90] Y. Wang *et al.*, "Design principles for solid-state lithium superionic conductors," *Nature Materials,* vol. 14, no. 10, pp. 1026-+, Oct 2015, doi: 10.1038/nmat4369.

[91] J. Christensen *et al.*, "A Critical Review of Li/Air Batteries," *J. Electrochem. Soc.,* vol. 159, no. 2, pp. R1-R30, 2012 2012, doi: 10.1149/2.086202jes.

[92] Y. F. Mo, S. P. Ong, and G. Ceder, "First-principles study of the oxygen evolution reaction of lithium peroxide in the lithium-air battery," *Physical Review B,* vol. 84, no. 20, Nov 2011, Art no. 205446, doi: 10.1103/PhysRevB.84.205446.

[93] C. M. Julien, A. Mauger, K. Zaghib, and D. Liu, "High Voltage Cathode Materials," *Rechargeable Batteries: Materials, Technologies and New Trends,* pp. 477-509, 2015, doi: 10.1007/978-3-319-15458-9_17.

[94] C. Li *et al.*, "Cathode materials modified by surface coating for lithium ion batteries," *Electrochimica Acta,* vol. 51, no. 19, pp. 3872-3883, May 20 2006, doi: 10.1016/j.electacta.2005.11.015.

[95] Z. Chen, Y. Qin, K. Amine, and Y. K. Sun, "Role of surface coating on cathode materials for lithium-ion batteries," *Journal of Materials Chemistry,* vol. 20, no. 36, pp. 7606-7612, 2010 2010, doi: 10.1039/c0jm00154f.

[96] Z. H. Chen and J. R. Dahn, "Methods to obtain excellent capacity retention in LiCoO2 cycled to 4.5 V," *Electrochimica Acta,* vol. 49, no. 7, pp. 1079-1090, Mar 15 2004, doi: 10.1016/j.electacta.2003.10.019.

[97] A. Mauger and C. Julien, "Surface modifications of electrode materials for lithium-ion batteries: status and trends," *Ionics,* vol. 20, no. 6, pp. 751-787, Jun 2014, doi: 10.1007/s11581-014-1131-2.

[98] L. Su, Y. Jing, and Z. Zhou, "Li ion battery materials with core-shell nanostructures," *Nanoscale,* vol. 3, no. 10, pp. 3967-3983, 2011 2011, doi: 10.1039/c1nr10550g.

[99] X. Wang and G. Yushin, "Chemical vapor deposition and atomic layer deposition for advanced lithium ion batteries and supercapacitors," *Energy & Environmental Science,* vol. 8, no. 7, pp. 1889-1904, 2015 2015, doi: 10.1039/c5ee01254f.

[100] N. Ravet, Y. Chouinard, J. F. Magnan, S. Besner, M. Gauthier, and M. Armand, "Electroactivity of natural and synthetic triphylite," *Journal of Power Sources,* vol. 97-8, pp. 503-507, Jul 2001, doi: 10.1016/s0378-7753(01)00727-3.

[101] H. Li and H. Zhou, "Enhancing the performances of Li-ion batteries by carbon-coating: present and future," *Chemical Communications,* vol. 48, no. 9, pp. 1201-1217, 2012 2012, doi: 10.1039/c1cc14764a.

[102] M. Jeong, M.-J. Lee, J. Cho, and S. Lee, "Surface Mn Oxidation State Controlled Spinel LiMn2O4 as a Cathode Material for High-Energy Li-Ion Batteries," *Advanced Energy Materials,* vol. 5, no. 13, Jul 8 2015, Art no. 1500440, doi: 10.1002/aenm.201500440.

[103] J.-H. Shim *et al.*, "Characterization of Spinel LixCo2O4-Coated LiCoO2 Prepared with Post-Thermal Treatment as a Cathode Material for Lithium Ion Batteries," *Chemistry of Materials,* vol. 27, no. 9, pp. 3273-3279, May 12 2015, doi: 10.1021/acs.chemmater.5b00159.

[104] J. Li, J. Camardese, R. Shunmugasundaram, S. Glazier, Z. Lu, and J. R. Dahn, "Synthesis and Characterization of the Lithium-Rich Core-Shell Cathodes with Low Irreversible Capacity and Mitigated Voltage Fade," *Chemistry of Materials,* vol. 27, no. 9, pp. 3366-3377, May 12 2015, doi: 10.1021/acs.chemmater.5b00617.

[105] K. Zaghib *et al.*, "New advanced cathode material: LiMnPO4 encapsulated with LiFePO4," *Journal of Power Sources,* vol. 204, pp. 177-181, Apr 15 2012, doi: 10.1016/j.jpowsour.2011.11.085.

[106] J. Cho, "Correlation between AlPO4 nanoparticle coating thickness on LiCoO2 cathode and thermal stability," *Electrochimica Acta,* vol. 48, no. 19, pp. 2807-2811, Aug 15 2003, doi: 10.1016/s0013-4686(03)00415-8.

[107] G. T. K. Fey, P. Muralidharan, C. Z. Lu, and Y. D. Cho, "Enhanced electrochemical performance and thermal stability of La2O3-coated LiCoO2," *Electrochimica Acta,* vol. 51, no. 23, pp. 4850-4858, Jun 15 2006, doi: 10.1016/j.electacta.2006.01.024.

[108] J. Kikkawa, S. Terada, A. Gunji, T. Nagai, K. Kurashima, and K. Kimoto, "Chemical States of Overcharged LiCoO2 Particle Surfaces and Interiors Observed Using Electron Energy-Loss Spectroscopy," *Journal of Physical Chemistry C,* vol. 119, no. 28, pp. 15823-15830, Jul 16 2015, doi: 10.1021/acs.jpcc.5b02303.

[109] J. Lee, D. H. Seo, M. Balasubramanian, N. Twu, X. Li, and G. Ceder, "A new class of high capacity cation-disordered oxides for rechargeable lithium batteries: Li-Ni-Ti-Mo oxides," *Energy & Environmental Science,* vol. 8, no. 11, pp. 3255-3265, 2015, doi: 10.1039/c5ee02329g.

[110] X. F. Bian *et al.*, "Multi-Functional Surface Engineering for Li-Excess Layered Cathode Material Targeting Excellent Electrochemical and Thermal Safety Properties," *Acs Applied Materials & Interfaces,* vol. 8, no. 5, pp. 3308-3318, Feb 2016, doi: 10.1021/acsami.5b11199.

[111] J. R. Croy *et al.*, "Examining Hysteresis in Composite xLi2MnO3·(1–x)LiMO2 Cathode Structures," *Journal of Physical Chemistry C,* vol. 117, no. 13, pp. 6525-6536, Apr 4 2013, doi: 10.1021/jp312658q.

[112] C. L. Wei, W. He, X. D. Zhang, J. X. Shen, and J. Y. Ma, "Recent progress in hybrid cathode materials for lithium ion batteries," *New Journal of Chemistry,* vol. 40, no. 4, pp. 2984-2999, 2016, doi: 10.1039/c5nj02212f.

[113] A. Van der Ven, J. Bhattacharya, and A. A. Belak, "Understanding Li Diffusion in Li-Intercalation Compounds," *Accounts of Chemical Research,* vol. 46, no. 5, pp. 1216-1225, May 21 2013, doi: 10.1021/ar200329r.

[114] H.-C. Yu, H.-Y. Chen, and K. Thornton, "Extended smoothed boundary method for solving partial differential equations with general boundary conditions on complex boundaries," *Modelling and Simulation in Materials Science and Engineering,* vol. 20, no. 7, Oct 2012, Art no. 075008, doi: 10.1088/0965-0393/20/7/075008.

[115] B. Orvananos *et al.*, "Architecture Dependence on the Dynamics of Nano-LiFePO4 Electrodes," *Electrochimica Acta,* vol. 137, pp. 245-257, Aug 10 2014, doi: 10.1016/j.electacta.2014.06.029.

[116] B. Orvananos *et al.*, "Effect of a Size-Dependent Equilibrium Potential on Nano-LiFePO4 Particle Interactions," *Journal of the Electrochemical Society,* vol. 162, no. 9, pp. A1718-A1724, 2015 2015, doi: 10.1149/2.0161509jes.

[117] B. Orvananos *et al.*, "Kinetics of Nanoparticle Interactions in Battery Electrodes," *Journal of the Electrochemical Society,* vol. 162, no. 6, pp. A965-A973, 2015 2015, doi: 10.1149/2.0481506jes.

[118] B. Orvananos, "Modeling and Simulation of Nanoparticulate Lithium Iron Phosphate Battery Electrodes," Ph.D., Materials Science and Engineering, University of Michigan, Ann Arbor, MI, 2014.

[119] P. J. Bouwman, "Lithium Intercalation in Preferentially Oriented Submicron $LiCoO_2$ Films," Ph.D., University of Twente, The Netherlands, 2002.

[120] Q. C. Zhuang *et al.*, "LiCoO2 electrode/electrolyte interface of Li-ion batteries investigated by electrochemical impedance spectroscopy," *Science in China Series B-Chemistry,* vol. 50, no. 6, pp. 776-783, Dec 2007, doi: 10.1007/s11426-007-0088-7.

[121] M. Park, X. C. Zhang, M. D. Chung, G. B. Less, and A. M. Sastry, "A review of conduction phenomena in Li-ion batteries," *Journal of Power Sources,* vol. 195, no. 24, pp. 7904-7929, Dec 2010, doi: 10.1016/j.jpowsour.2010.06.060.

[122] B. Wu, Y. Ren, and N. Li, "$LiFePO_4$ Cathode Material," in *Electric Vehicles - The Benefits and Barriers*, S. Soylu Ed.: InTech, 2011, ch. 6, pp. 199-216.

[123] M. Okubo, E. Hosono, T. Kudo, H. S. Zhou, and I. Honma, "Size effect on electrochemical property of nanocrystalline LiCoO(2) synthesized from rapid thermal annealing method," *Solid State Ionics,* vol. 180, no. 6-8, pp. 612-615, May 2009, doi: 10.1016/j.ssi.2008.06.010.

[124] A. Sidhu, A. Izadian, and S. Anwar, "Adaptive Nonlinear Model-Based Fault Diagnosis of Li-Ion Batteries," *Ieee Transactions on Industrial Electronics,* vol. 62, no. 2, pp. 1002-1011, Feb 2015, doi: 10.1109/tie.2014.2336599.

[125] Y. Hua, M. Xu, M. Li, C. B. Ma, and C. Zhao, "Estimation of State of Charge for Two Types of Lithium-Ion Batteries by Nonlinear Predictive Filter for Electric Vehicles," *Energies,* vol. 8, no. 5, pp. 3556-3577, May 2015, doi: 10.3390/en8053556.

[126] T. Nakajima and H. Groult, *Advanced Fluoride-Based Materials for Energy Conversion*. Waltham, MA, USA: Elsevier, 2015, p. 458.

[127] C. M. Julien, A. Mauger, K. Zaghib, and H. Groult, "Comparative Issues of Cathode Materials for Li-Ion Batteries," *Inorganics,* vol. 2, pp. 132-154, 2014.

[128] H. Xia, L. Lu, and G. Ceder, "Li diffusion in LiCoO2 thin films prepared by pulsed laser deposition," *Journal of Power Sources,* vol. 159, no. 2, pp. 1422-1427, Sep 2006, doi: 10.1016/j.jpowsour.2005.12.012.

[129] H. Xia, L. Lu, Y. S. Meng, and G. Ceder, "Phase transitions and high-voltage electrochemical behavior of LiCoO2 thin films grown by pulsed laser deposition," *Journal of the Electrochemical Society,* vol. 154, no. 4, pp. A337-A342, 2007, doi: 10.1149/1.2509021.

[130] K. N. Grew and W. K. S. Chiu, "A review of modeling and simulation techniques across the length scales for the solid oxide fuel cell," *Journal of Power Sources,* vol. 199, pp. 1-13, Feb 2012, doi: 10.1016/j.jpowsour.2011.10.010.

[131] M. J. Buehler, "Atomistic and continuum modeling of mechanical properties of collagen: Elasticity, fracture, and self-assembly," *Journal of Materials Research,* vol. 21, no. 8, pp. 1947-1961, Aug 2006, doi: 10.1557/jmr.2006.0236.

[132] P. Babakhani, J. Bridge, R. A. Doong, and T. Phenrat, "Continuum-based models and concepts for the transport of nanoparticles in saturated porous media: A state-of-the-science review," *Advances in Colloid and Interface Science,* vol. 246, pp. 75-104, Aug 2017, doi: 10.1016/j.cis.2017.06.002.

[133] S. DeWitt, N. Hahn, K. Zavadil, and K. Thornton, "Computational Examination of Orientation-Dependent Morphological Evolution during the Electrodeposition and Electrodissolution of Magnesium," *Journal of the Electrochemical Society,* vol. 163, no. 3, pp. A513-A521, 2016 2016, doi: 10.1149/2.0781603jes.

[134] B. Orvananos, T. R. Ferguson, H. C. Yu, M. Z. Bazant, and K. Thornton, "Particle-Level Modeling of the Charge-Discharge Behavior of Nanoparticulate Phase-Separating Li-Ion Battery Electrodes," *Journal of the Electrochemical Society,* vol. 161, no. 4, pp. A535-A546, 2014, doi: 10.1149/2.024404jes.

[135] I. A. Guz, A. A. Rodger, A. N. Guz, and J. J. Rushchitsky, "Developing the mechanical models for nanomaterials," *Composites Part a-Applied Science and Manufacturing,* vol. 38, no. 4, pp. 1234-1250, 2007, doi: 10.1016/j.compositesa.2006.04.012.

[136] J. T. Hertz *et al.*, "Magnetism and structure of LixCoO2 and comparison to NaxCoO2," *Physical Review B,* vol. 77, no. 7, Feb 2008, Art no. 075119, doi: 10.1103/PhysRevB.77.075119.

[137] H. Wang, W. D. Zhang, L. Y. Zhu, and M. C. Chen, "Effect of LiFePO4 coating on electrochemical performance of LiCoO2 at high temperature," *Solid State Ionics,* vol. 178, no. 1-2, pp. 131-136, Jan 2007, doi: 10.1016/j.ssi.2006.10.028.

[138] C. Shen, B. Zhang, J. C. Zheng, Y. D. Han, and J. F. Zhang, "Effect of sintering time on the synthesize of the multi-layered core-shell LiVOPO4-Li3V2(PO4)(3) composite for Li-ion batteries," *Journal of Alloys and Compounds,* vol. 622, pp. 771-776, Feb 2015, doi: 10.1016/j.jallcom.2014.10.198.

[139] S. C. Park, Y. M. Kim, Y. M. Kang, K. T. Kim, P. S. Lee, and J. Y. Lee, "Improvement of the rate capability of LiMn2O4 by surface coating with LiCoO2," *Journal of Power Sources,* vol. 103, no. 1, pp. 86-92, Dec 2001, doi: 10.1016/s0378-7753(01)00832-1.

[140] B. Sadeghi, R. Sarraf-Mamoory, and H. R. Shahverdi, "Surface Modification of LiMn2O4 for Lithium Batteries by Nanostructured LiFePO4 Phosphate," *Journal of Nanomaterials,* 2012, Art no. 743236, doi: 10.1155/2012/743236.

[141] S. J. Harris and P. Lu, "Effects of Inhomogeneities-Nanoscale to Mesoscale-on the Durability of Li-Ion Batteries," *Journal of Physical Chemistry C,* vol. 117, no. 13, pp. 6481-6492, Apr 2013, doi: 10.1021/jp311431z.

[142] H. Liu *et al.*, "Intergranular Cracking as a Major Cause of Long-Term Capacity Fading of Layered Cathodes," *Nano Letters,* vol. 17, no. 6, pp. 3452-3457, Jun 2017, doi: 10.1021/acs.nanolett.7b00379.

[143] M. X. Tang *et al.*, "Following lithiation fronts in paramagnetic electrodes with in situ magnetic resonance spectroscopic imaging," *Nature Communications,* vol. 7, Nov 2016, Art no. 13284, doi: 10.1038/ncomms13284.

[144] K. Kirshenbaum *et al.*, "In situ visualization of Li/Ag2VP2O8 batteries revealing rate-dependent discharge mechanism," *Science,* vol. 347, no. 6218, pp. 149-154, Jan 2015, doi: 10.1126/science.1257289.

[145] F. C. Strobridge *et al.*, "Mapping the Inhomogeneous Electrochemical Reaction Through Porous LiFePO4-Electrodes in a Standard Coin Cell Battery," *Chemistry of Materials,* vol. 27, no. 7, pp. 2374-2386, Apr 2015, doi: 10.1021/cm504317a.

[146] J. Nanda *et al.*, "Anomalous Discharge Product Distribution in Lithium-Air Cathodes," *Journal of Physical Chemistry C,* vol. 116, no. 15, pp. 8401-8408, Apr 2012, doi: 10.1021/jp3016003.

[147] J. P. Owejan, J. J. Gagliardo, S. J. Harris, H. Wang, D. S. Hussey, and D. L. Jacobson, "Direct measurement of lithium transport in graphite electrodes using neutrons," *Electrochimica Acta,* vol. 66, pp. 94-99, Apr 2012, doi: 10.1016/j.electacta.2012.01.047.

[148] Y. X. Zhang, K. S. R. Chandran, and H. Z. Bilheux, "Imaging of the Li spatial distribution within V2O5 cathode in a coin cell by neutron computed tomography," *Journal of Power Sources,* vol. 376, pp. 125-130, Feb 2018, doi: 10.1016/j.jpowsour.2017.11.080.

[149] K. J. Harry, K. Higa, V. Srinivasan, and N. P. Balsara, "Influence of Electrolyte Modulus on the Local Current Density at a Dendrite Tip on a Lithium Metal Electrode," *Journal of the Electrochemical Society,* vol. 163, no. 10, pp. A2216-A2224, 2016, doi: 10.1149/2.0191610jes.

[150] L. Nowack, D. Grolimund, V. Samson, F. Marone, and V. Wood, "Rapid Mapping of Lithiation Dynamics in Transition Metal Oxide Particles with Operando X-ray Absorption Spectroscopy," *Scientific Reports,* vol. 6, Feb 2016, Art no. 21479, doi: 10.1038/srep21479.

[151] M. Ebner, F. Marone, M. Stampanoni, and V. Wood, "Visualization and Quantification of Electrochemical and Mechanical Degradation in Li Ion Batteries," *Science,* vol. 342, no. 6159, pp. 716-720, Nov 2013, doi: 10.1126/science.1241882.

[152] P. Pietsch *et al.*, "Quantifying microstructural dynamics and electrochemical activity of graphite and silicon-graphite lithium ion battery anodes," *Nature Communications,* vol. 7, Sep 2016, Art no. 12909, doi: 10.1038/ncomms12909.

[153] J. J. Wang, Y. C. K. Chen-Wiegart, and J. Wang, "In operando tracking phase transformation evolution of lithium iron phosphate with hard X-ray microscopy," *Nature Communications,* vol. 5, Aug 2014, Art no. 4570, doi: 10.1038/ncomms5570.

[154] J. J. Wang, Y. C. K. Chen-Wiegart, and J. Wang, "In Situ Three-Dimensional Synchrotron X-Ray Nanotomography of the (De) lithiation Processes in Tin Anodes**," *Angewandte Chemie-International Edition,* vol. 53, no. 17, pp. 4460-4464, Apr 2014, doi: 10.1002/anie.201310402.

[155] K. J. Harry, X. X. Liao, D. Y. Parkinson, A. M. Minor, and N. P. Balsara, "Electrochemical Deposition and Stripping Behavior of Lithium Metal across a Rigid Block Copolymer Electrolyte Membrane," *Journal of the Electrochemical Society,* vol. 162, no. 14, pp. A2699-A2706, 2015, doi: 10.1149/2.0321514jes.

[156] K. M. O. Jensen *et al.*, "X-Ray Diffraction Computed Tomography for Structural Analysis of Electrode Materials in Batteries," *Journal of the Electrochemical Society,* vol. 162, no. 7, pp. A1310-A1314, 2015, doi: 10.1149/2.0771507jes.

[157] J. Sottmann *et al.*, "Chemical Structures of Specific Sodium Ion Battery Components Determined by Operando Pair Distribution Function and X-ray Diffraction Computed Tomography," *Angewandte Chemie-International Edition,* vol. 56, no. 38, pp. 11385-11389, Sep 2017, doi: 10.1002/anie.201704271.

[158] P. Bleuet, E. Welcomme, E. Dooryhee, J. Susini, J. L. Hodeau, and P. Walter, "Probing the structure of heterogeneous diluted materials by diffraction tomography," *Nature Materials,* vol. 7, no. 6, pp. 468-472, Jun 2008, doi: 10.1038/nmat2168.

[159] W. Lai *et al.*, "Ultrahigh-Energy-Density Microbatteries Enabled by New Electrode Architecture and Micropackaging Design," *Advanced Materials,* vol. 22, no. 20, pp. E139-+, May 2010, doi: 10.1002/adma.200903650.

[160] J. I. Hur, L. C. Smith, and B. Dunn, "High Areal Energy Density 3D Lithium-Ion Microbatteries," *Joule,* vol. 2, no. 6, pp. 1187-1201, Jun 2018, doi: 10.1016/j.joule.2018.04.002.

[161] A. Yamada *et al.*, "Room-temperature miscibility gap in Li(x)FePO(4)," *Nature Materials,* vol. 5, no. 5, pp. 357-360, May 2006, doi: 10.1038/nmat1634.

[162] A. K. Padhi, K. S. Nanjundaswamy, and J. B. Goodenough, "Phospho-olivines as positive-electrode materials for rechargeable lithium batteries," *Journal of the Electrochemical Society,* vol. 144, no. 4, pp. 1188-1194, Apr 1997, doi: 10.1149/1.1837571.

[163] T. R. Ferguson and M. Z. Bazant, "Nonequilibrium Thermodynamics of Porous Electrodes," *Journal of the Electrochemical Society,* vol. 159, no. 12, pp. A1967-A1985, 2012, doi: 10.1149/2.048212jes.

[164] Y. Y. Li *et al.*, "Current-induced transition from particle-by-particle to concurrent intercalation in phase-separating battery electrodes," *Nature Materials,* vol. 13, no. 12, pp. 1149-1156, Dec 2014, doi: 10.1038/nmat4084.

[165] R. Darling and J. Newman, "Modeling a porous intercalation electrode with two characteristic particle sizes," *Journal of the Electrochemical Society,* vol. 144, no. 12, pp. 4201-4208, Dec 1997, doi: 10.1149/1.1838166.

[166] P. Bai, D. A. Cogswell, and M. Z. Bazant, "Suppression of Phase Separation in LiFePO4 Nanoparticles During Battery Discharge," *Nano Letters,* vol. 11, no. 11, pp. 4890-4896, Nov 2011, doi: 10.1021/nl202764f.

[167] S. Dargaville and T. W. Farrell, "A comparison of mathematical models for phase-change in high-rate LiFePO4 cathodes," *Electrochimica Acta,* vol. 111, pp. 474-490, Nov 2013, doi: 10.1016/j.electacta.2013.08.014.

[168] S. Dargaville and T. W. Farrell, "The persistence of phase-separation in LiFePO4 with two-dimensional Li+ transport: The Cahn-Hilliard-reaction equation and the role of defects," *Electrochimica Acta,* vol. 94, pp. 143-158, Apr 2013, doi: 10.1016/j.electacta.2013.01.082.

[169] M. Pasquali, A. Dell'Era, and P. P. Prosini, "Fitting of the voltage-Li+ insertion curve of LiFePO4," *Journal of Solid State Electrochemistry,* vol. 13, no. 12, pp. 1859-1865, Dec 2009, doi: 10.1007/s10008-008-0737-6.

[170] E. S. Takeuchi, A. C. Marschilok, K. J. Takeuchi, A. Ignatov, Z. Zhong, and M. Croft, "Energy dispersive X-ray diffraction of lithium-silver vanadium phosphorous oxide cells: in situ cathode depth profiling of an electrochemical reduction-displacement reaction," *Energy & Environmental Science,* vol. 6, no. 5, pp. 1465-1470, May 2013, doi: 10.1039/c3ee40152a.

[171] T. R. Ferguson, "Lithium-ion battery modeling using non-equilibrium thermodynamics," Ph.D., Department of Chemical Engineering, Massachusetts Institute of Technology, Cambridge, MA, United States, 2014.

[172] G. K. P. Dathar, D. Sheppard, K. J. Stevenson, and G. Henkelman, "Calculations of Li-Ion Diffusion in Olivine Phosphates," *Chemistry of Materials,* vol. 23, no. 17, pp. 4032-4037, Sep 2011, doi: 10.1021/cm201604g.

[173] B. Kang and G. Ceder, "Battery materials for ultrafast charging and discharging," *Nature,* vol. 458, no. 7235, pp. 190-193, Mar 2009, doi: 10.1038/nature07853.

[174] J. S. Newman and C. W. Tobias, "Theoretical Analysis of Current Distribution in Porous Electrodes," *Journal of the Electrochemical Society,* vol. 109, no. 12, pp. 1183-1191, 1962, doi: 10.1149/1.2425269.

[175] I. V. Thorat, D. E. Stephenson, N. A. Zacharias, K. Zaghib, J. N. Harb, and D. R. Wheeler, "Quantifying tortuosity in porous Li-ion battery materials," *Journal of Power Sources,* vol. 188, no. 2, pp. 592-600, Mar 2009, doi: 10.1016/j.jpowsour.2008.12.032.

[176] K. Zaghib, A. Mauger, J. B. Goodenough, F. Gendron, and C. M. Julien, "Electronic, optical, and magnetic properties of LiFePO4: Small magnetic polaron effects," *Chemistry of Materials,* vol. 19, no. 15, pp. 3740-3747, Jul 2007, doi: 10.1021/cm0710296.

[177] H. C. Shin, W. I. Cho, and H. Jang, "Electrochemical properties of carbon-coated LiFePO4 cathode using graphite, carbon black, and acetylene black," *Electrochimica Acta,* vol. 52, no. 4, pp. 1472-1476, Dec 2006, doi: 10.1016/j.electacta.2006.01.078.

[178] K. J. Zhao, M. Pharr, J. J. Vlassak, and Z. G. Suo, "Fracture of electrodes in lithium-ion batteries caused by fast charging," *Journal of Applied Physics,* vol. 108, no. 7, Oct 2010, Art no. 073517, doi: 10.1063/1.3492617.

[179] X. Y. Zhang, T. W. Verhallen, F. Labohm, and M. Wagemaker, "Direct Observation of Li-Ion Transport in Electrodes under Nonequilibrium Conditions Using Neutron Depth Profiling," *Advanced Energy Materials,* vol. 5, no. 15, Aug 2015, Art no. 1500498, doi: 10.1002/aenm.201500498.

[180] V. P. Nemani, S. J. Harris, and K. C. Smith, "Design of Bi-Tortuous, Anisotropic Graphite Anodes for Fast Ion-Transport in Li-Ion Batteries," *Journal of the Electrochemical Society,* vol. 162, no. 8, pp. A1415-A1423, 2015, doi: 10.1149/2.0151508jes.

[181] N. A. Zacharias, D. R. Nevers, C. Skelton, K. Knackstedt, D. E. Stephenson, and D. R. Wheeler, "Direct Measurements of Effective Ionic Transport in Porous Li-Ion Electrodes," *Journal of the Electrochemical Society,* vol. 160, no. 2, pp. A306-A311, 2013, doi: 10.1149/2.062302jes.

[182] T. Marks, S. Trussler, A. J. Smith, D. J. Xiong, and J. R. Dahn, "A Guide to Li-Ion Coin-Cell Electrode Making for Academic Researchers," *Journal of the Electrochemical Society,* vol. 158, no. 1, pp. A51-A57, 2011, doi: 10.1149/1.3515072.

[183] K. C. Smith, P. P. Mukherjee, and T. S. Fisher, "Columnar order in jammed LiFePO4 cathodes: ion transport catastrophe and its mitigation," *Physical Chemistry Chemical Physics,* vol. 14, no. 19, pp. 7040-7050, 2012, doi: 10.1039/c2cp40135e.

[184] M. Ebner, D. W. Chung, R. E. Garcia, and V. Wood, "Tortuosity Anisotropy in Lithium-Ion Battery Electrodes," *Advanced Energy Materials,* vol. 4, no. 5, Apr 2014, Art no. 1301278, doi: 10.1002/aenm.201301278.

[185] D. Kehrwald, P. R. Shearing, N. P. Brandon, P. K. Sinha, and S. J. Harris, "Local Tortuosity Inhomogeneities in a Lithium Battery Composite Electrode," *Journal of the Electrochemical Society,* vol. 158, no. 12, pp. A1393-A1399, 2011, doi: 10.1149/2.079112jes.

[186] H. G. Zhang, X. D. Yu, and P. V. Braun, "Three-dimensional bicontinuous ultrafast-charge and -discharge bulk battery electrodes," *Nature Nanotechnology,* vol. 6, no. 5, pp. 277-281, May 2011, doi: 10.1038/nnano.2011.38.

[187] C. J. Bae, C. K. Erdonmez, J. W. Halloran, and Y. M. Chiang, "Design of Battery Electrodes with Dual-Scale Porosity to Minimize Tortuosity and Maximize Performance," *Advanced Materials,* vol. 25, no. 9, pp. 1254-1258, Mar 2013, doi: 10.1002/adma.201204055.

[188] P. R. Amestoy and I. S. Duff, "Vectorization of a multiprocessor multifrontal code," *International Journal of Supercomputer Applications and High Performance Computing,* vol. 3, no. 3, pp. 41-59, Fal 1989, doi: 10.1177/109434208900300303.

[189] P. R. Amestoy, I. S. Duff, J. Y. L'Excellent, and J. Koster, "A fully asynchronous multifrontal solver using distributed dynamic scheduling," *Siam Journal on Matrix Analysis and Applications,* vol. 23, no. 1, pp. 15-41, Apr 2001, doi: 10.1137/s0895479899358194.

[190] D. K. Karthikeyan, G. Sikha, and R. E. White, "Thermodynamic model development for lithium intercalation electrodes," *Journal of Power Sources,* vol. 185, no. 2, pp. 1398-1407, Dec 2008, doi: 10.1016/j.jpowsour.2008.07.077.

[191] A. Nyman, M. Behm, and G. Lindbergh, "Electrochemical characterisation and modelling of the mass transport phenomena in LiPF6-EC-EMC electrolyte," *Electrochimica Acta,* vol. 53, no. 22, pp. 6356-6365, Sep 2008, doi: 10.1016/j.electacta.2008.04.023.